



# Neue numerische Studien von Bit Patterned Magnetic Recording

DISSERTATION

zur Erlangung des akademischen Grades

**Doktor der Technischen Wissenschaften**

eingereicht von

**Alexander Kovacs BSc MSc**

Matrikelnummer 1328387

an der Fakultät für Physik  
der Technischen Universität Wien

Betreuung: Univ.- Doz. Dipl.-Ing. Dr. Thomas Schrefl

Diese Dissertation haben begutachtet:

---

Nicola Morley

---

Franz Keplinger

Wien, 1. Oktober 2020

---

Alexander Kovacs



Die approbierte gedruckte Originalversion dieser Dissertation ist an der TU Wien Bibliothek verfügbar.  
The approved original version of this doctoral thesis is available in print at TU Wien Bibliothek.



# Novel numerical studies of bit patterned magnetic recording

DISSERTATION

submitted in partial fulfillment of the requirements for the degree of

**Doktor der Technischen Wissenschaften**

by

**Alexander Kovacs BSc MSc**

Registration Number 1328387

to the Faculty of Physics  
at the Vienna University of Technology

Advisor: Univ.- Doz. Dipl.-Ing. Dr. Thomas Schrefl

The dissertation has been reviewed by:

---

Nicola Morley

---

Franz Keplinger

Vienna, 1<sup>st</sup> October, 2020

---

Alexander Kovacs



Die approbierte gedruckte Originalversion dieser Dissertation ist an der TU Wien Bibliothek verfügbar.  
The approved original version of this doctoral thesis is available in print at TU Wien Bibliothek.

**Morty:** All right, all right. So, what's so special about these seeds, anyways?

**Rick:** You ask a lot of questions, Morty. Not very charismatic. It makes you kind of an (burps) under- (burps) underfoot figure.

**Morty:** You have a whole planet sitting around making your power for you? That's slavery.

**Rick:** It's society. They work for each other, Morty. They pay each other. They buy houses. They get married and make children that replace them when they get too old to make power.

**Morty:** That just sounds like slavery with extra steps.

**Rick:** Ooh-la-la, someone's gonna get laid in college.



Die approbierte gedruckte Originalversion dieser Dissertation ist an der TU Wien Bibliothek verfügbar.  
The approved original version of this doctoral thesis is available in print at TU Wien Bibliothek.

# Erklärung zur Verfassung der Arbeit

Alexander Kovacs BSc MSc  
Albertsgasse 4 / 19, A-1210 Wien

Hiermit erkläre ich, dass ich diese Arbeit selbständig verfasst habe, dass ich die verwendeten Quellen und Hilfsmittel vollständig angegeben habe und dass ich die Stellen der Arbeit – einschließlich Tabellen, Karten und Abbildungen –, die anderen Werken oder dem Internet im Wortlaut oder dem Sinn nach entnommen sind, auf jeden Fall unter Angabe der Quelle als Entlehnung kenntlich gemacht habe.

Wien, 1. Oktober 2020

---

Alexander Kovacs



Die approbierte gedruckte Originalversion dieser Dissertation ist an der TU Wien Bibliothek verfügbar.  
The approved original version of this doctoral thesis is available in print at TU Wien Bibliothek.



# Danksagung

Zu aller erst muss ich mich bei meinem Doktorvater, Chef, Vorbild, Mentor und Freund bedanken. Danke Thomas. Ohne Deiner positiven Zusprüche, Deiner exzellenten Führungsfähigkeit, Inspiration und Motivation wäre dieses Dokument und mein Interesse für so viele neue Dinge nie zu Stande gekommen. Man kann sich keinen besseren Chef als Dich wünschen. Ich möchte mich auch bei all meinen Kollegen und Freunden bedanken. Bei manchen dafür, dass sie mich bei jeder Gelegenheit nach dem Status meiner Dissertation fragten, bei manchen dafür, dass sie es unterlassen haben. Ich bin eigentlich der Meinung, dass ich hier jeden Menschen, dem ich jemals begnete, danken sollte, da er mich auf eine gewisse Weise inspiriert hat. Ganz gleich ob er nur ein paar wenige Schritte oder bereits eine Dekade neben mir durchs Leben ging. Das kann ich aber leider nicht aus Platzgründen und Wissenslücken und deswegen nenne ich hier nur eine bergenzte Auswahl an Gesichtern die mich auf diesem langen steinigen Weg begleitet, unterstützt, inspiriert oder sekkiert haben. Danke Dir, ganz besonders Dir Harald Özelt, Johann Fischbacher, Markus Gusenbauer, Franz Reichel, Lukas Exl, Simon Bance, David Hahn, Hossein Sepherin-Amin, Gino Hrkac, Alex Goncharov, Manfred Schabes, Thomas Glatzl, Aleksey Bratukhin, Roman Beigelbeck, Wilfried Hortschitz, Herbert Weitensfelder, Matthias Kahr, Astrit Shoshi, Harald Steiner, Hubert Brückl, Marco Lubarda, Boris Livshitz, Vitaly Lomakin, Muhammad Asif Bashir, Swaraj Basu, Mark Gubbins, Robert Lamberton, Dieter Suess, Claas Abert, Pietro Palmesi, Anton Bachleitner-Hofmann, Roman Windl, Christian Huber, Christoph Vogler, Florian Bruckner, Bernhard Bergmair, Sabri Koraltan, Markus Fuger, Erol Girt, Florian Dorfbauer, Otto Reichel, Georg Gutenbrunner, Edward R. Tufte, Ulrike Lachner und Elisabeth Schiefer. Meinen Freunden, Freundinnen, privaten Wegbegleitern und Wegbegleiterinnen, Roman Köhler, Sebastian Forthuber, Markus Müllner-Rieder, Tina Eberhardt, Anna Gorczynski, Simon Klausner, Alexander Kriz, Sabrina Löffle, Tobias, Lukas und Christina Rescheneder. Und natürlich danke ich auch meiner Familie. Danke Dir Maria und Herbert Kovacs. Danke Andrea Waldner, mich geboren und durchgefüttert zu haben sowie mich bis heute zu dulden. Danke Dir Ludwig Pichler mir wie ein Vater bei Seite zu stehen. Danke auch Dir Sebastian Kovacs und Arthur Pichler. Und danke auch an Dich solltest Du Deinen Namen bis jetzt nicht gelesen haben.



Die approbierte gedruckte Originalversion dieser Dissertation ist an der TU Wien Bibliothek verfügbar.  
The approved original version of this doctoral thesis is available in print at TU Wien Bibliothek.

# Acknowledgements

First and foremost, I have to thank my supervisor, boss, role model, mentor and friend. Thanks Thomas. Without your positive encouragement, your excellent teaching skills, inspiration and motivation, this document and my interest in so many new things would never have come about. There is no better boss than you. I would also like to thank all my colleagues and friends. Some of them for asking me about the status of my thesis at every opportunity, some of them for not doing so. I actually feel that I should thank every person I ever met here, because they have inspired me in some way. No matter if he or she walked just a few steps or already a decade next to me through life. Unfortunately, I cannot do this for reasons of space and knowledge, so here is just a selection of the faces that have accompanied, supported, inspired or pestered me on this long and rocky road. Thank you, especially you Harald Özelt, Johann Fischbacher, Markus Gusenbauer, Franz Reichel, Luke Exl, Simon Bance, David Hahn, Hossein Sepherin-Amin, Gino Hrkac, Alex Goncharov, Manfred Schabes, Thomas Glatzl, Aleksey Bratukhin, Roman Beigelbeck, Wilfried Hortschitz, Herbert Weitensfelder, Matthias Kahr, Astrit Shoshi, Harald Steiner, Hubert Brückl, Marco Lubarda, Boris Livshitz, Vitaly Lomakin, Muhammad Asif Bashir, Swaraj Basu, Mark Gubbins, Robert Lamberton, Dieter Suess, Claas Abert, Pietro Palmesi, Anton Bachleitner-Hofmann, Roman Windl, Christian Huber, Christoph Vogler, Florian Bruckner, Bernhard Bergmair, Sabri Koraltan, Markus Fuger, Erol Girt, Florian Dorfbauer, Otto Reichel, Georg Gutenbrunner, Edward R. Tufte, Ulrike Lachner and Elisabeth Schiefer. My friends and private companions, Roman Köhler, Sebastian Forthuber, Markus Müllner-Rieder, Tina Eberhardt, Anna Gorczynski, Simon Klausner, Alexander Kriz, Sabrina Löffle, Tobias, Lukas and Christina Reschender. And of course I also thank my family. Thank you Maria and Herbert Kovacs. Thank you Andrea Waldner for having given birth to me, for raising and tolerating me until today. Thank you Ludwig Pichler for standing by me like a father. Thanks also to Sebastian Kovacs and Arthur Pichler. And thanks also to you, if you haven't read your name by now.



Die approbierte gedruckte Originalversion dieser Dissertation ist an der TU Wien Bibliothek verfügbar.  
The approved original version of this doctoral thesis is available in print at TU Wien Bibliothek.

# Kurzfassung

Es wird erwartet, dass die Gesamtmenge der jedes Jahr erstellten Daten von derzeit 50 ZB im Jahr 2020 auf 175 ZB im Jahr 2025 anwachsen wird. Dabei werden mehr als 60 % dieser Datenmenge von Endpunkten wie Internet-of-Things Geräten, Fahrzeugen, Smartphones und ihren Benutzern erzeugt werden, während die anderen 40 % in großen Datenzentren und Gateways, Mobilfunk-Zelltürmen und Zweigstellen erzeugt werden. Während sich die Datenspeicherung von Festplattenlaufwerken auf Solid-State-Laufwerke in mobilen Computergeräten verlagert hat, werden Festplattenlaufwerke hauptsächlich in Datenspeicherzentren eingesetzt. Um den stetig steigenden Speicherbedarf zu decken, müssen etwa 60 % der jährlich produzierten Daten auf Festplattenlaufwerken in traditionellen oder Cloud-basierten Rechenzentren gespeichert werden. In dieser Arbeit wird ein System entwickelt, das in der Lage ist, die Form eines konventionellen magnetischen Schreibkopfes und das darunter liegende Medium eines Festplattenlaufwerks zu optimieren. Ein Konstruktionskript für eine parametrisierte Schreibkopfgeometrie wird in ein Optimierungs-Framework eingebettet. Mit mikromagnetischen Simulationen wird das emittierte Schreibfeld eines einpoligen Schreibkopfes in der Medienebene berechnet. Dynamische Schreibprozesse werden simuliert, um drei spezifische Fehlerraten zu berechnen: (i) kein Schreiben des gewünschten Bits, (ii) falsches Schreiben eines zuvor geschriebenen Bits und (iii) thermisch induziertes Überschreiben von Bits in einer benachbarten Spur. Durch Abstimmung der Materialeigenschaften des Mediums kann die Gesamtfehlerrate angepasst werden. Die magnetokristalline Anisotropiekonstante wird für ein einphasiges bit-strukturiertes Mediendesign mit einer Speicherdichte von  $2.12 \text{ Tb/in}^2$  und die Kopplungsstärke und Anisotropiekonstante für ein austauschgekoppeltes Verbundmedium mit einer Speicherdichte von  $4 \text{ Tb/in}^2$  optimiert. Um das Potenzial von zentrierter, gestaffelter und geschichteter Aufzeichnung zu untersuchen, werden beide Medientwürfe für jedes Schreibschema getrennt optimiert. Ein kommerzieller Multiobjektiv-Optimierer und ein Open-Source-Optimierungs-Framework werden eingesetzt. Der Optimierer findet zwei lokale Minima, bei denen unterschiedliche Medientypen auftreten, während die Form des Schreibkopfes ähnlich bleibt. Ein optimierter Medientyp weist eine starke Kopplung zwischen der harten und der weichen Schicht auf, während der andere eine schwache Kopplung aufweist. Die Gesamtschreibfehlerraten können mit Hilfe dieses Frameworks unter die Obergrenze von  $10^{-2}$  gesenkt werden. Die Schichtaufzeichnung erweist sich als das vielversprechendste Schema in Hinblick auf die Maximierung der Speicherdichte und die Reduzierung der Schreibfehlerraten.



Die approbierte gedruckte Originalversion dieser Dissertation ist an der TU Wien Bibliothek verfügbar.  
The approved original version of this doctoral thesis is available in print at TU Wien Bibliothek.

# Abstract

The total amount of data created each year is expected to grow from currently 50 ZB in 2020 to 175 ZB in 2025. Where more than 60 % of this amount of data will be produced by endpoints such as Internet-of-Things devices, vehicles, smartphones and their users, whereas the other 40 % is produced at large data centers and gateways, cell towers and branch offices. While data storage has shifted from hard disc drives to solid state drives in mobile computing devices, hard disc drives are mostly used in data storage centers. To meet the steadily increasing storage demand, around 60 % of the annual produced data will have to be stored on hard disc drives at traditional or cloud based datacenters. In this thesis a framework capable of optimizing the shape of a conventional magnetic recording head and the underlying media of a hard disc drive is developed. A parametrized script for the construction of recording head geometries is embedded into an optimization framework. With micromagnetic simulations the emitted write field of a single pole recording head is computed at the media plane. Dynamic recording processes are simulated to compute three specific error rates: (i) not writing the target, (ii) falsely writing a previously written bit, and (iii) thermally induced overwriting of bits in an adjacent track. The total error rate can be adjusted by tuning the material properties of the medium. The magnetocrystalline anisotropy constant is optimized for a single phase bit patterned media design with a storage density of 2.12 Tb/in<sup>2</sup> and the coupling strength and anisotropy constant for an exchange coupled composite media with a storage density of 4 Tb/in<sup>2</sup>. To investigate the potential of centered, staggered and shingled recording, both media designs are optimized for each writing scheme, separately. A commercial multiobjective optimizer and an open source optimization framework are applied. The optimizer finds two local minima where different media types show up while the recording head's shape stays similar. One optimized media type has strong coupling between the hard and soft layer whereas the other has a weak coupling. The total write error rates can be decreased below the upper limit of 10<sup>-2</sup> with the help of this framework. Shingled recording turns out to be the most promising scheme in terms of areal density maximization and reduction of write error rates.



Die approbierte gedruckte Originalversion dieser Dissertation ist an der TU Wien Bibliothek verfügbar.  
The approved original version of this doctoral thesis is available in print at TU Wien Bibliothek.



# Contents

<b>Kurzfassung</b>	<b>xiii</b>
<b>Abstract</b>	<b>xv</b>
<b>1 Motivation</b>	<b>1</b>
<b>2 Basics of Magnetic Recording</b>	<b>5</b>
2.1 How does Magnetic Recording work? . . . . .	5
2.1.1 Sufficient Recording Head Field . . . . .	8
2.1.2 Writeable but Stable Media . . . . .	8
2.1.3 Read-Back Conditions . . . . .	10
2.2 Superparamagnetic Limit . . . . .	10
2.3 Extended Overview . . . . .	13
2.3.1 Media and Media Reversal Modes . . . . .	14
2.3.2 Recorder and Recording Schemes . . . . .	17
2.3.3 Read Head . . . . .	19
2.3.4 Writer Shields . . . . .	21
2.3.5 Skewing and Pole Tip Taper Angle . . . . .	21
2.3.6 Recording Errors and their Occurrences . . . . .	22
<b>3 Global Optimization Method</b>	<b>23</b>
3.1 Search Strategies . . . . .	24
3.2 Conclusion . . . . .	31
<b>4 Micromagnetic Background</b>	<b>33</b>
4.1 Introduction . . . . .	33
4.2 Total Gibb's Free Energy . . . . .	35
4.2.1 Zeeman Energy . . . . .	35
4.2.2 Exchange Energy . . . . .	35
4.2.3 Anisotropy Energy . . . . .	36
4.2.4 Demagnetizing Energy . . . . .	37
4.3 Exchange lengths . . . . .	38
4.4 Magnetization Dynamics . . . . .	39
4.5 Energy barrier estimation . . . . .	40

<b>5</b>	<b>Initial Investigations</b>	<b>43</b>
5.1	Write field computation . . . . .	43
5.2	Manual Optimization . . . . .	46
5.3	Results and Discussion . . . . .	47
5.3.1	Centered Recording . . . . .	47
5.3.2	Staggered Recording . . . . .	48
5.3.3	Shingled Recording . . . . .	50
<b>6</b>	<b>Multi-objective optimization of static recording simulation</b>	<b>53</b>
6.1	Strategy . . . . .	54
6.1.1	Design Evaluation . . . . .	54
6.1.2	Optimization Process . . . . .	54
6.1.3	Error Rate Approximation . . . . .	56
6.2	Geometrical Setup . . . . .	60
6.2.1	Predefined Media Design . . . . .	60
6.2.2	Parametrized Recording Head Design . . . . .	60
6.3	Results . . . . .	62
6.4	Remarks . . . . .	64
<b>7</b>	<b>Single objective optimization of dynamic recording simulation</b>	<b>69</b>
7.1	Strategy . . . . .	70
7.1.1	Design Evaluation . . . . .	70
7.1.2	Optimization Process . . . . .	71
7.1.3	Comprehensive Objective Function . . . . .	72
7.1.4	Improved Error Rate Approximation . . . . .	72
7.2	Geometrical Setup . . . . .	75
7.2.1	Exchange Coupled Composite Media Design and Layout . . . . .	75
7.2.2	Parametrized Recording Head Design . . . . .	76
7.3	Results . . . . .	78
7.4	Remarks . . . . .	80
<b>8</b>	<b>Conclusion and Outlook</b>	<b>83</b>
8.1	Conclusion . . . . .	83
8.1.1	Possible Model Improvements . . . . .	84
8.2	Outlook . . . . .	84
	<b>Bibliography</b>	<b>87</b>

# List of Figures

1.1	Tree Chart of Magnetic Recording Companies over Time . . . . .	3
2.1	Magnetic Recording is Rocket Science . . . . .	6
2.2	Finite Element Model of Perpendicular Write Head, Pole Tip and Media . . . . .	7
2.3	Unshielded Magnetoresistive Read Head Principle . . . . .	11
2.4	Media Grainsize Transition-Width Correlations . . . . .	11
2.5	Granular Media Structure vs. Bit Patterned Media . . . . .	14
2.6	Stoner-Wohlfarth Particle . . . . .	16
2.7	Nucleation Field vs. Magnet Size and Categorization of Reversal Modes . . . . .	17
2.8	Media Types: Single Phase, Exchange Coupled Composite and Graded . . . . .	17
2.9	Recording Orientations Sketch . . . . .	18
2.10	Three Different Recording Schemes . . . . .	20
2.11	Finite Element Model of a Perpendicular Read Head . . . . .	21
2.12	Skewing and Pole Tip Taper Angle . . . . .	22
3.1	Random Sampling vs. Optimized Latin-Hypercube Sampling . . . . .	26
3.2	Parameter Activeness and Error Correlation . . . . .	28
3.3	Describing an Optimization Problem with a Gaussian Process . . . . .	29
3.4	Uncertainty along the Prediction . . . . .	29
3.5	Probability of Improvement . . . . .	30
3.6	Expected Improvement Function along Prediction . . . . .	30
4.1	Kronmüller, Fähnle’s application areas of Micromagnetism . . . . .	34
4.2	Uniaxial and easy-plane Magnetocrystalline Anisotropy . . . . .	37
4.3	Damped Precessional Motion of Magnetic Moment towards Effective Field . . . . .	40
5.1	Micromagnetic Simulation Setup with Recording Head and Underlying Evaluation Regions . . . . .	45
5.2	Stoner-Wohlfarth Model’s Effective Field Scaling Factor . . . . .	46
5.3	Field bubble to media layout matching . . . . .	47
5.4	Different Coil Currents and Magnetic Spacing for Centered Writing . . . . .	48
5.5	Different Coil Currents and Side Shield Gaps for Centered Writing . . . . .	49
5.6	Different Coil Currents and Side Shield Gaps for Staggered Writing . . . . .	49
5.7	Different Track Centers for Different Coil Currents for Shingled Recording Head . . . . .	50
5.8	Effective Field Profile for Shingled Writing . . . . .	50
6.1	Target and Adjacent Track Field Profile Analysis . . . . .	57
6.2	Field Profile Expectations of Multi-Objective Approach . . . . .	57
6.3	Field Profile Working Point and Objective Function Definitions for Error Rate Estimation . . . . .	59

6.4	Single Phase Media Layout Definition . . . . .	61
6.5	Dimensions and Materials of Finite Element Recording Head Geometry for Field Determination . . . . .	63
6.6	Multi Objective Approach's Design Parameters for Pole Tip and Shield for Optimization Software . . . . .	63
6.7	Optimized Field Profiles and Gradients for Centered, Staggered and Shingled Scheme . . . . .	65
6.8	Remarks on Recording Model's Plot Over Line Definition . . . . .	67
7.1	Design Error Rate Evaluation Flow Chart . . . . .	71
7.2	Target and Previous Bit Error Rate Simulation Setup and Possible Outcomes	74
7.3	Statistical Approach of Write Error Estimation . . . . .	75
7.4	Exchange Coupled Composite Media Layout Definition . . . . .	77
7.5	Single Objective Approach's Design Parameters of Pole Tip and Shield for Optimization Software . . . . .	78
7.6	Charge Sheet Approach . . . . .	79
7.7	Final Field Profile Analysis of Single Objective Approach . . . . .	82

## List of Tables

6.1	Applied Intrinsic Material Properties of Recording Head Model . . . . .	61
6.2	Design Parameter Space Restriction . . . . .	62
6.3	Multi Objective Approach Results . . . . .	64
7.1	Design Space Restrictions for joint Optimization of Head and Media . . . . .	80
7.2	Final Results of Single Objective Approach . . . . .	81

# CHAPTER 1

## Motivation

There being nowadays throughout the scientific world great activity of thought regarding listening and talking machines, the readers of *THE ELECTRICAL WORLD* may be interested in a description of two or three possible methods of making a phonograph which the writer contrived some years ago, but which were laid aside and never brought to completion on account of a press of other work.

"Some Possible Forms of Phonograph" by Oberlin Smith, September 8, 1888

The American engineer Oberlin Smith proposed these ideas for data storage after visiting Thomas Edison's laboratory in New Jersey. It is said that Oberlin Smith has seen Edison's phonograph where a needle was used to etch sound waves through vibration onto a rotating cylinder. Inspired by this concept of recording and replaying sound he wanted to improve Edison's recording device by replacing the mechanical approach with an electromagnetic one. Instead of a stylus a magnetic coil should record the sound waves onto a magnetizable wire. He unfortunately failed to build a prototype, but wrote an accurate description about his ideas which are dated back to the year 1878. Ten years later in the year 1888 he published an article in The Electrical World magazine [1] making his previous thoughts accessible for everyone who is "interested" in and willing to spend approximately 4% of his own daily wage at that time for the magazine<sup>1</sup>. It took ten more years until Valdemar Poulsen officially proved Smith's concepts feasibility by developing a functional prototype: the "Telegraphone". This device was intended to store and replay missed telephone calls and Poulsen filed patents for his invention in Denmark and the United States [3]. At the International Exhibition in Paris in the year 1900 he demonstrated his machinery to Franz Joseph, the Austrian emperor at this time, whose excitement has been recorded and is still preserved in the Danish Museum of Science

---

<sup>1</sup>percentage in the US and 8% in Belgium/around Europe, according to the average daily wages in the United States and Europe, 1870-1898 [2]

and Technology. After Poulsen's patents [3–8] expired the technology has been further improved. Fritz Pfeumer filed a patent about a magnetizable powder embedded into a thin elastic film being in direct contact with a reading and recording device [9], which can be considered as the beginning of the "tape".

When the first non-commercial computing machines were introduced at that time data and programs were stored on punched paper cards. Soon the computational power and amount of produced data increased and so did the demand of data storage. Reading and writing data on magnetic tapes has been the latest technique back at that time. But one major drawback of this system was, that the tape had to be rolled up on a tube, which required sequential reading and writing processes by winding the tape forwards and backwards. A more flexible technology which would allow reading and writing at any time and location onto the media was needed.

After several years of research IBM introduced its first commercially available hard disc drive in the year 1956. The hard disc was shipped in a room-sized computer and consisted of 50 rotating magnetic discs, each 24 inches ( $\approx 0.6$  m) in diameter. The read/write head was floating above the discs with pressurized air. This technique prevented the discs from mechanical damage in contrast to the previous tape read/write heads, which always had to be in contact with the tape. With a, at that time achievable areal density of  $2 \text{ kbit in}^{-2}$  (around  $3 \text{ bit mm}^{-2}$ ) a total capacity of 4.5 MB was reached.

Between 1957 and today the competitive magnetic recording industry demonstrated great advancements. 1988 for example, a new magneto-resistive effect was discovered by Fert [10] and Grünberg [11] independently. Later this discovery has been recognized with the Nobel Price in 2007. The exploitation of the giant magneto-resistive effect (GMR) led to more sensible reading heads, which consequently allowed increased areal density. Its first usage in hard drives has been demonstrated by IBM. In 1997 IBM released a storage system with a total storage capacity of about 17 GB [12]. In 1988 the new form factor of 2.5 inches for hard disc drives was introduced, which is still used today in mobile devices. From 1991 to 1998 the areal density doubled every two years. Perpendicular recording was introduced into the market by Seagate, Hitachi and Fujitsu in 2006 [13]. Many other improvements of recording- and read-heads in lithography for fabrication and for overall performance appeared. Inventions in terms of how to record the information like in a two-dimensional manner or shingled magnetic recording further improved the areal density. The usage of composite materials for magnetic recording reduced the required write fields [14, 15].

As shown in Fig. 1.1 many individual companies emerged and were bought by other recording companies later. Please note that this list is not complete and focuses on the past of today's three leading recording companies. The success of the different companies was mainly determined by the ability to file new patents describing small improvements in magnetic recording.

Why is this important? Magnetic hard discs are predominantly used today in data centers storing 60 % of the overall produced data [18]. The demand of storage capacity increases with cloud computing and the number of mobile devices. The monthly data usage of one mobile device lies around 7 GB in 2019 and is expected to increase [19]. The

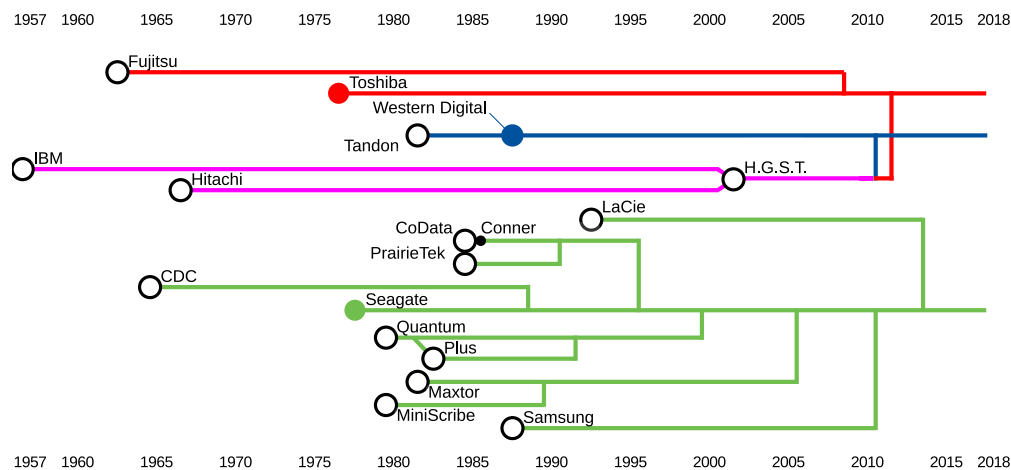


Figure 1.1: A tree chart including the three big hard drive companies Toshiba, Western Digital and Seagate. Company names are colored and grouped by their present owner. The chart visualizes the data compiled from [16] and the plot is generated with help of gnuclad [17]. In [16] it is pointed out that the founding year and the year of first shipment has been taken for startups and other entrants, respectively.

increase in storage capacity per surface area reduces the number of spinning discs in data centers and consequently the energy costs. Every possible method capable of improving the current hard drive system at hand had and still should be considered.

One common method to improve the storage density is the systematical variation of adjustable parameters using design of experiment analysis. This methodology is commonly used in the automotive industry. The combination of finite element analysis with optimization [20] has a long tradition in the automotive industry [21] and electrical engineering [22]. Applied in magnetic recording numerical optimization can improve the system design [23–25]. Key adjustable parameters for hard disc storage include the geometrical features of the write head and the intrinsic properties of the recording media.

The main goal for optimization magnetic recording is to increase areal density, the amount of bits stored per limited amount of space measured in bits per square inch ( $\text{bit in}^{-2}$ ). A bit cell describes the minimum required surface area in which one single bit resides.

Recent granular bit cell sizes are around 10 nm to 15 nm times 8 nm [26, pp. 161] which translates into areal densities above 1 Tbit  $\text{in}^{-2}$ . Currently, one bit of information is stored in 6–10 magnetic grains on the disc. The microstructure of a recording media will be discussed in Sections 2.1.2 and 2.1.3 and is shown in Fig. 2.4. One bit cell, as shown in Fig. 2.5, has an average length of one grain diameter and a width of multiple grain diameters.

Increasing the areal density is not a simple task, which will be discussed in more detail in Section 2.2. With about 7 grains per bit of information, current hard disc drives store

a bit on an area of around 7.5 nm times 8 nm. There are many design objectives which have to be optimized simultaneously. These include thermal stability, address-ability, write-ability and read-ability. With decreasing bit size one has to make a risky trade-off between conflicting objectives. Clever ways for multi-objective optimization need to be introduced.

The main topic of this work is to use numerical optimization to reduce the write error rate, which is an important figure of merit in magnetic recording. It has to be mentioned though, that "Magnetic Recording" itself governs a large variety of different terms and effects and that it is not scope of this work to revisit all of them in a detailed manner. The main goal is to demonstrate increased efficiencies in recording systems with the help of numerical optimization methods.

Magnetic recording systems can be improved by optimizing the geometry of magnetic write heads [23, 27, 28], changing the layout and material compositions [14, 15] of the data layer or improving the channel and error correction codes [29]. In this thesis I focus on the simultaneous optimization of recording heads and data layer properties for bit patterned magnetic recording. The joint optimization of these design variables can lead to a significant reduction of the write error rate as discussed in Section 7.3.

Industries, where prototyping is time consuming and expensive – for example in the automotive or semiconductor industry – can greatly benefit from the use of computation models and simulations. Even simplified models can still predict valuable system parameters, rule out designs or give a comparison of the importance of different parameters. These computational results can then improve the whole system and reduce the costs of prototyping (see Section 6.4). As pointed out in [26, p. 55] the fabrication of a typical recording head takes around 5 months involving more than 1000 processing steps.

This work might be of interest to researchers working in the field of magnetic recording, simulations with finite element micromagnetic solvers and maybe partially in the field of global optimization methods and shape optimizations.

Readers unfamiliar with the functionality of hard drives or magnetic recording will find an introduction in Chapter 2, which is followed by a description of optimization strategies or methods used within this work in Chapter 3 and micromagnetism in Chapter 4.

Chapter 5 introduces the basic concepts for the computational exploration of write fields and associated recording strategies for high density recording for areal densities greater than 2 Td/in<sup>2</sup>.

A constrained multi-objective optimization of raw output data treated statically is presented in Chapter 6. A single objective optimization incorporating a more elaborate definition of recording performance is presented in Chapter 7.

Combining micromagnetic simulation tools with an optimization toolkit which automatically explores a recording systems parameter space with a well formulated definition of improvement is presented in Section 7.1.2.

Chapter 8 summarizes the main findings.



# Basics of Magnetic Recording

## Contents

2.1	How does Magnetic Recording work? . . . . .	<b>5</b>
2.1.1	Sufficient Recording Head Field . . . . .	8
2.1.2	Writeable but Stable Media . . . . .	8
2.1.3	Read-Back Conditions . . . . .	10
2.2	Superparamagnetic Limit . . . . .	<b>10</b>
2.3	Extended Overview . . . . .	<b>13</b>
2.3.1	Media and Media Reversal Modes . . . . .	14
2.3.2	Recorder and Recording Schemes . . . . .	17
2.3.3	Read Head . . . . .	19
2.3.4	Writer Shields . . . . .	21
2.3.5	Skewing and Pole Tip Taper Angle . . . . .	21
2.3.6	Recording Errors and their Occurrences . . . . .	22

This chapter gives a brief introduction to magnetic recording. Section 2.1 introduces the three major parts inside a hard drive and how their interplay forms a system in which it is possible to write bits onto the disc and how these written bits can be read out again. Then I discuss the current problems associated with increasing the storage density which result from the conflicting objectives of thermal stability, signal to noise ratio, writeability. Then current concepts to overcome this trilemma are introduced. Section 2.3 explains in more detail each part of the device and the different terms used in the field of magnetic recording and within this work.

## 2.1 How does Magnetic Recording work?

A hard disc drive can be split up into three major magnetic parts: the recording head, the media and the read head. Fig. 2.1 introduces such a perpendicular magnetic recording system from different views and at different length scales.

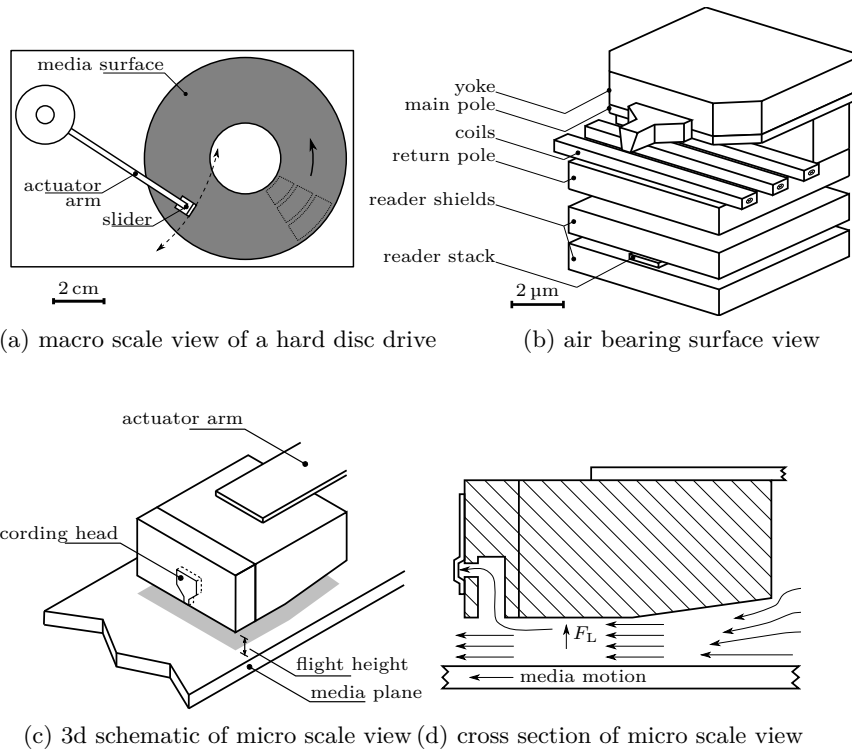


Figure 2.1: Three different length scales of magnetic recording (a) "most familiar view" of a hard disc drive taken and adapted from [30]. Highlighted is the rotating disc and the actuator arm which has the slider mounted on its tip. (b) Media-surface perspective's view. Highlighted is the mainpole, its coils and the reader element (taken and adapted from [31]). (c) On the sliders trailing edge the main pole is highlighted. The media plane illustrated here includes the soft under layer. The schematic is taken and adapted from [32]. (d) Cross-section of the slider, in which the main pole is highlighted. Note that the control of the flight height has to consider aerodynamics in such length scales.

In Fig. 2.1a one can see the most familiar perspective of a hard disc drive (HDD). On the right hand side the disc represents the media. On the left hand side the actuator arm, which is positioning the read/write head above a track. Mounted onto this actuator is the slider, which is illustrated in more detail in Fig. 2.1c. Above the media the slider with the tiny recording head is mounted on the actuator arm.

The actuator arm controls the position of the head above a specific media track. Below, the rotating magnetizable discs are mounted onto a spindle motor. Just a 10 nm to 20 nm thin crystal structure layer represents the layer in which information is stored [33, pp. 138]. Below the media a soft under layer helps to close the magnetic flux from the main pole to the return pole. The single pole head consisting of main pole, soft under

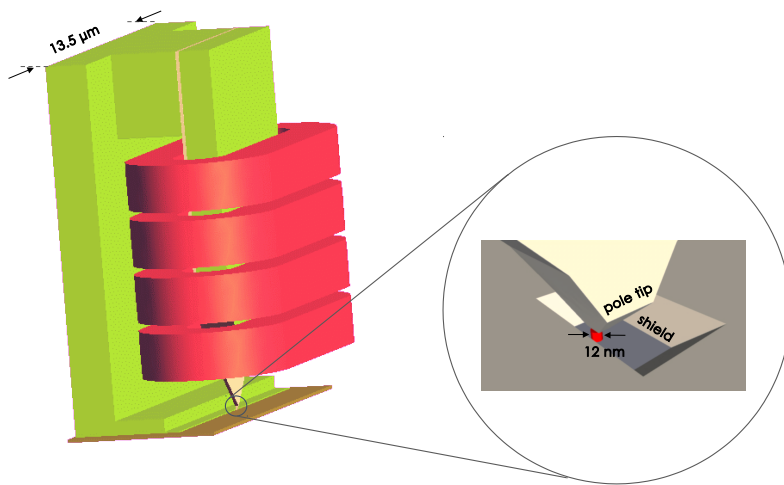


Figure 2.2: A finite element model of a perpendicular write head is shown. The main pole and yoke is surrounded a coil with 4 turns. In the enlarged section the shielded pole tip and one underlying bit patterned media island is shown.

layer and return pole was considered to be one of the main advantages of perpendicular magnetic recording, which places the data layer in the air gap of the write head instead of only using the fringing field of a ring head as in longitudinal magnetic recording. This enables higher write fields in perpendicular recording as compared to longitudinal recording.

To see the difference in scale between slider and main pole, the Fig. 2.1d shows a cross section of the floating slider from Fig. 2.1c. Within this cross section it becomes more clear that the thin film recording head and reader stack are just very small as compared to the slider. Fig. 2.1b is the media's view onto the air bearing surface. From top to bottom one can see the yoke, main pole, coil wires, return pole and after a gap the read head, residing between two large shields. In Fig. 2.1b the tip of the main pole is shown, which will be further referred to as pole tip. Small vents control the airflow in order to keep the distance to belows media surface constant.

The difference in scales is best illustrated in Fig. 2.2 where we chose a finite element model of the writer. The enlarged section shows the pole tip and one island of a bit patterned media.

By applying a current to the coil contacts, dependent on the current's direction the recording head will reverse to the desired polarization and switches the media's magnetization, in perpendicular recording, up or down.

The reader element on the other side, picks up the changes in stray field coming from the media. It detects the transitions between regions polarized up and down. The

detection of a transition or no transition is then translated into a binary 1 or 0 respectively. More details for the layout of a read head are given in Section 2.3.3.

### 2.1.1 Sufficient Recording Head Field

The emitted field of the recording head has to fulfill certain requirements. First, the field seen from the media layer has to be larger than the media switching field which, for simplicity, is proportional to the anisotropy field  $H_{\text{ani}}$ .  $H_{\text{ani}} = 2K_{\text{u}}/J_{\text{s}}$  depends on intrinsic magnetic material properties, the uniaxial anisotropy constant  $K_{\text{u}}$  and the spontaneous magnetic polarization  $J_{\text{s}}$ .

These strong fields have to be narrowed down to a small region of a few nanometers in order to write only on a single track. In other words adjacent tracks and previously written information have to be protected from accidental reversal inflicted by the magnetic field of the head writing bits on an adjacent track. Soft magnetic shields are capable of protecting neighboring tracks in cross-track direction and previously written bits in down-track direction. High cross- and down-track field gradients are required. The distance of the shield and the main pole in both down- and cross-track direction is influencing the recording head's field strength inside the media. If the shield is placed too far apart, adjacent tracks will be overwritten. If the shield is placed too close to the pole tip, the write field will be reduced, as the shields attract the flux. A too tight placement might also introduce a reversed magnetic domain into the shield. This is unwanted as the strayfield from the associated domain wall could reverse sections of the media which should be actually protected from reversal.

Additionally the main pole has to flip the magnetization of its tip as fast as bit cells on the spinning media disc pass by. The higher the areal density the faster the bit cell is moving.

As the conventional user is not permanently storing information onto the hard disc, the magnetic recording head has to be able to go into a neutral non-writing magnetization state. Such a neutral state can be achieved by using a tip made of anti-ferromagnetic coupled layers, as shown in [34].

Summary of head requirements which all have to be coordinated with the underlying media structure:

- sufficient write field
- sufficiently sharp field transition
- fast reversing pole tip magnetization ensuring a rapidly changing write field
- narrow spatial distribution of the write field

### 2.1.2 Writeable but Stable Media

In conventional recording systems (= perpendicular recording), the media plane consists of a granular structured thin film. The media has to fulfill two requirements, writeability and thermal stability.

1. it's magnetization has to be able to get reversed where the effective write field reaches its maximum
2. it has to withstand thermal fluctuations and the field of a head passing multiple times adjacent tracks.

The media's switching field  $H_{sw}$  is determined by the intrinsic material properties saturation polarization  $J_s$  and magnetocrystalline anisotropy  $K_u$  ( $H_{sw} \propto K_u/J_s$ ). By fine tuning composition or even substituting media material during many complex processing steps – via substrate temperature or gas pressure – recording media composed of layer of different magnetic materials can be fabricated. In this composite media the switching field can be adjusted to the specific write fields [35]. Due to thin-film fabrication steps inhomogeneities occur in the data layer and the intrinsic material properties vary location dependent. This local variation of intrinsic properties results in a distribution of the switching field [36]. This will be relevant for error rate estimations in Sections 6.1.3 and 7.1.4.

The media has to retain its magnetization configuration for at least the lifetime of the mechanical parts of the hard drive. The average lifetime  $\tau$  of a single bit is related to its magnetizations thermal stability. The thermal stability depends on energy barrier  $E_B$  for magnetization reversal which in turn changes with the reversal type. For uniform rotation the energy barrier is  $K_u V$  where  $V$  is the grain volume. If the grain reverses by the nucleation an expansion of a reversed domain the energy barrier is proportional to  $4A\sqrt{A_{ex}K_u}$ , where  $A_{ex}$  is the exchange constant and  $A$  is the cross sectional area of the grain. The non-uniform reversal process is especially important for high aspect ratio grains [37] and composite recording media. The average lifetime of the magnetization of a single grain is

$$\tau = \frac{1}{f_0} \exp\left(\frac{E_B}{k_B T}\right), \quad (2.1)$$

where  $k_B$  is the Boltzmann constant and  $T$  the temperature. The dependency of the thermal stability of the grain size introduces new issues when increasing the areal storage density later on (see Section 2.2). The energy barrier is often given in units of  $k_B T$  and is normally chosen to be around 47–50  $k_B T$  which corresponds to an average media lifetime of 8–164 years, for an attempt frequency  $f_0 = 10^{12}$  Hz.

How a single bit reverses its magnetization configuration in the vicinity of a recording head field strongly affects the minimum required field in order to switch such a bit. The media's reversal process can be categorized into either coherent or incoherent switching and will be discussed in more detail in Section 2.3.1.

Summary of media requirements:

- sufficient lifetime  $\tau$
- sufficiently low media switching field  $H_{sw}$  to enable writing
- narrow spatial  $H_{sw}$  distribution

### 2.1.3 Read-Back Conditions

Recovering information from the media plane is achieved with the reader-stack shown in Fig. 2.1b. To ensure that the read head is only picking up the stray fields from below, it has to be placed between soft magnetic shields, which "suck" away unwanted stray fields from neighboring bits in cross- and down-track direction.

A simplistic view of the reader's functionality is given in Fig. 2.3. Note that here the bit cell polarizations are longitudinally aligned, as this is a schematic of a longitudinal read head using a magneto-resistive element for transition detections. Earlier magnetic recording media had its magnetization in-plane in relation to the media plane, whereas today's recording media has its magnetization perpendicular to its plane. As this work focuses on head media interplay, a longitudinal read head is detailed enough to outline the concept of recovering information from the media. As the read head flies above the media the emitted stray field changes the reader elements polarization, which can be picked up as a proportional change in the sensing current measured at lead contacts.

The number of grains forming a bit cell plays a significant role for the detectivity of transitions in granular media. As emphasized in [26, p. 66, Fig. 2.10] reducing the size of the bit cell deteriorates the signal to noise ratio unless the number of grains in the bit can be kept constant. In addition to the number of grains per bit the signal to noise ratio depends on the transition width. The signal to noise ratio scales as  $1/a^2$ , where  $a$  is the transition width [38].

In Fig. 2.4 the effect of reducing the grain size on the read-ability is demonstrated. From left to right the grain size decreases while consequently the number of grains increases for a constant track width. The average transition width is proportional to the average grain size and the sharper the transition the better its detectivity. Or in other words, with wider transition width noise in the read-back signal gets significant. Further details can be found in [26].

By using bit patterned media, the granular thin film is replaced by ordered single islands separated by a non-magnetic phase as outlined in Fig. 2.5. The signal-to-noise ratio is no longer a grain size dependent factor but scales with lithographic fabrication tolerances.

A list of reader element requirements:

- high sensitivity/high detectivity
- tailored to media's areal density and track width

## 2.2 Superparamagnetic Limit

The areal density increases each year with a highest growth rate around the year 2000. [41] For many years the superparamagnetic limit was considered to be the fundamental limit for magnetic recording. In this limit the grain size is so small that thermal activation reverses a bit before the desired storage life time.

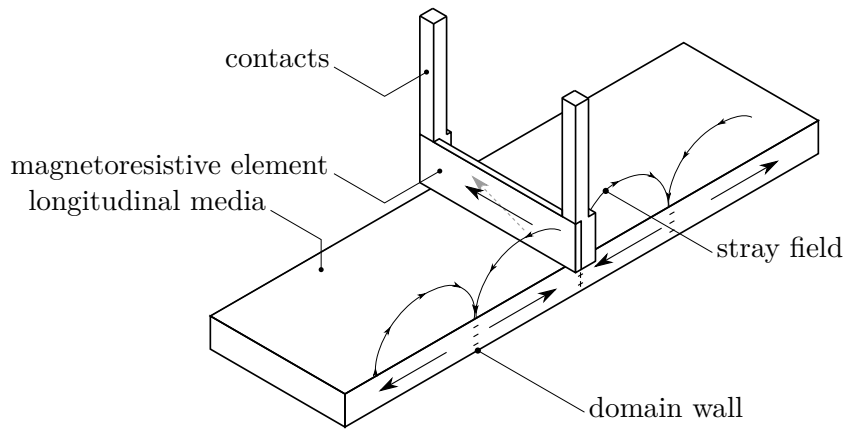


Figure 2.3: A schematic of a read head for longitudinal recording media. The sensing current is proportional to the angle between a free layer's magnetization direction and a pinned layer. The magnetization of the free layer is influenced by the emitted stray field coming from the underlying media. By measuring the sense current, transitions between two oppositely magnetized domains can be detected. Figure compiled from [39, 40]. The layout of a GMR read head is shown in Fig. 2.11.

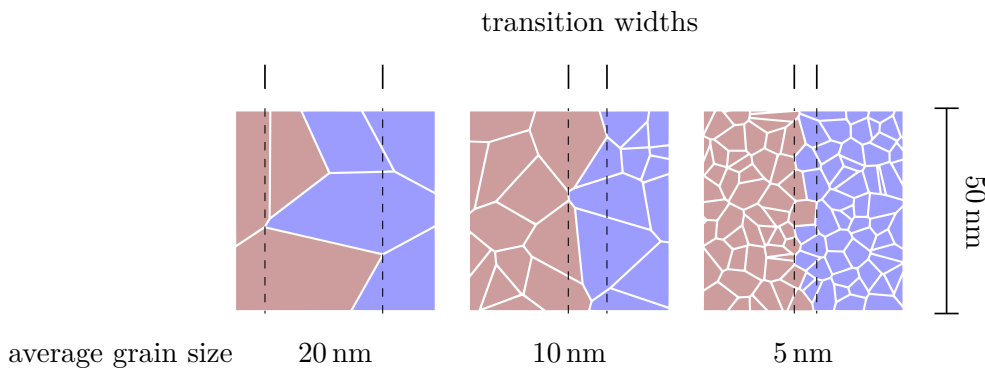


Figure 2.4: Conventional perpendicular magnetic recording media with different average grain diameters. The smaller the average grain diameter  $\langle d \rangle$  the smaller will be the transition width (distance between dashed lines). Consequently by using smaller grains the reader with 50 nm width can pick up the transitions more accurately.

In Sections 2.1.1– 2.1.3 it has shown that each part of the recording device has to fulfill certain requirements in order to achieve sufficient recording performances. Not all of those requirements can be met fully as some of them are concurring. This becomes more clear by looking at the average lifetime of a single bit as shown in Eq. (2.1). The energy barrier  $E_B$  increases with increasing anisotropy and increasing grain size.

An increase of areal density inevitably requires a reduction of grain size. This translates into a decrease of the energy barrier. And consequently an exponential decrease of thermal stability and life time  $\tau$ . To compensate this loss the use of magnetically harder material – larger  $K_u$  – for the media is necessary.

The switching field of a recording media is proportional to the anisotropy constant of its hardest layer. In case of single phase media we can approximate the media switching field with its anisotropy field, which is defined by

$$H_{\text{ani}} = \frac{2K_u}{J_s} \approx H_{\text{sw}}. \quad (2.2)$$

An increase of the anisotropy constant ensures thermal stability, but also results in an increase of the switching field and consequently the required write field  $H_{\text{eff}}$ . This approximation neglects the presence of stray field emitted by surrounding neighboring bits which might change the required switching field [42].

Unfortunately the maximum feasible induced head field to switch the magnetization of the bits is fundamentally limited to 1 T [43, 44]. Therefore, to ensure writable bits the anisotropy constant is restricted according to Eq. (2.2) as well. Other ways of reducing the media's switching field have to be considered.

Two major methods are able to overcome this issue and can provide more storage density, while maintaining thermal stability and writeability.

**Heat Assisted Magnetic Recording (HAMR):** HAMR uses a magnetically hard medium to ensure thermal stability, but uses an additional heat source, usually a laser, to elevate the temperature of a small region on the media where a bit should be written. By adding thermal energy the energy barrier can be overcome with smaller write fields.

The increased temperature reduces the local switching field below the feasible writing field of the head. When the heat source is removed, the magnetic state is thermally stable again due to the high anisotropy. Prominent candidates for hard magnetic media are composites of FePt which show anisotropy constants of around  $7 \text{ MJ/m}^3$  [26, p.220] which gives room temperature switching fields larger than 5 T and needs to be heated to 750 K to be writeable with a write field of around 1 T. A good overview can be found from D. Weller and co-workers [45].

A major challenge of this technology is to focus the heat spot onto a very small surface area where the bit should be written and the adjacent bits left unaltered. The focused laser beam is currently achieved by a near field transducer close to the media. The neighboring grains of the written area can be thermally protected by separating grains by a heat sink material. Further reading can be found in C. Vogler's thesis [46, 47].



Evans et al. [48] pointed out that under current (2012) conditions regarding heat-assisted magnetic recording the limit in terms of areal density will be 15 Tb/in<sup>2</sup> to 20 Tb/in<sup>2</sup> unless technology can move beyond the currently available write field magnitudes. Sufficient head fields are required to mitigate the thermally written in error. Since 2012 the feasible write field didn't change substantially, so that this density limit can still be regarded as valid.

**Microwave Assisted Magnetic Recording (MAMR):** Similar to HAMR the additional energy for overcoming the energy barrier is provided by an oscillating magnetic field. If the system is in resonance through the oscillations in the GHz regime energy is absorbed by the media's magnetization. This again helps to overcome the energy barrier to magnetically switch the bit. One advantage of MAMR over HAMR is the scalability in areal density, as the required frequency of such a microwave pulse is again material dependent, therefore opening the opportunity to use multiple layers with different but selectable resonance frequencies [49–52].

**Bit Patterned Media:** Besides the above mentioned strategies another approach is changing the underlying media structure. In bit patterned media the bit is formed by a continuous island: The magnetic unit comprises an entire island instead of a single grain. Thus the island size instead of the grain size determines the energy barrier for reversal. Thus the stability of a bit can be increased while the write field can be kept low. In current magnetic recording systems one bit is represented by less than ten grains, as shown in Fig. 2.5. Another idea is to use lithographically patterned islands. The illustration highlights the amount of possible bits in a restricted area. On the left, a granular media surface storing approximately 4 bits. In contrast a pseudo-hexagonally aligned bit patterned media layout with 20 nm dot size capable of storing almost the same information as in the granular case. And on the right hand side media islands with 12 nm diameter, which will be further investigated in Chapters 6 and 7. In addition to a higher ratio of life time over switching field,  $\tau/H_{sw}$ , the advantage over granular media structures is an increased detectivity of patterned bits, due to clear transitions, and the increase of track density in cross-track direction. Still the fabrication of such patterned islands [53] is even more complicated than granular media but promises areal densities of about 50 Tb/in<sup>2</sup> [54].

This thesis will cover recording on bit patterned media only and the improvement of both the recording head and the media with numerical optimization techniques.

## 2.3 Extended Overview

In Section 2.1 a brief introduction of the three key parts of a recording system has been given. In addition the increase of areal density and the arising issues with possible solutions have been introduced.

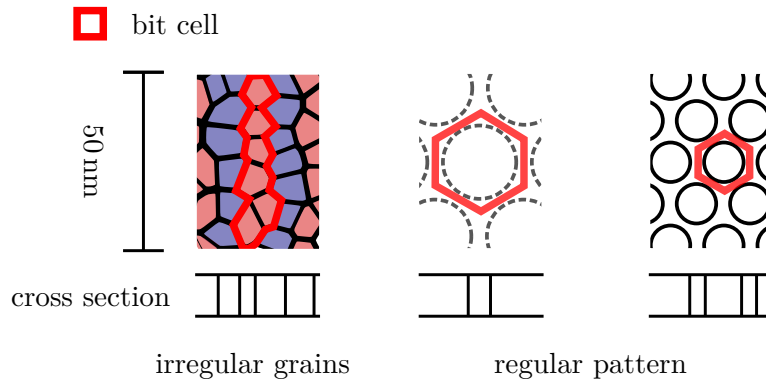


Figure 2.5: On the left hand side one single track of granular media with an average grain diameter of 7.5 nm. On the middle column bit patterned media with 20 nm diameter and on the right hand side a bit with 12 nm. The red contour highlights a single bit cell.

In the field of magnetic recording scientific publications and patents can be found for each part of the recording system by an overwhelming amount. In the following a brief explanation of those parts, which are subject of this work are given. Additional information required as a basis for this work is shown as well. Furthermore the bits magnetization reversal process and different strategies on how to write data onto the disc are explained.

### 2.3.1 Media and Media Reversal Modes

The software controlling the servo motor of the actuator arm and therefore the position of read/write processes is called the hard disc driver. It divides the storage media into sectors. Each sector consists of multiple tracks similar to the tracks on a gramophone record. Each track has a track width of approximately 10 nm to 30 nm [55]. The track width is measured in cross-track direction and the bit length in down-track direction. Track width and bit length describe a so-called "bit cell" ([56, p. 11–12], [57, Fig. 1]) as shown as a red contour in Fig. 2.5. The distances between "bit cells" are called down-track and cross-track pitch. And the number of bit cells on a square inch give us the areal density of such media. The areal density is often measured in units of bits per square inch B/in<sup>2</sup> or in bit patterned media also dots per square inch d/in<sup>2</sup>.

State of the art perpendicular magnetic recording heads [55] are capable of reversing just a few grains of a 10 nm to 15 nm thin CoCrPtSi-O crystal film [26, pp. 161]. These grains with an approximately diameter of 8 nm are weakly exchange coupled. The coupling is adjusted to minimize the transition parameter  $a$ . Each grain's magnetization state is influenced by the stray field of all neighboring grains. In bit patterned media one bit cell is represented by the magnetization of one magnetically separated island. Fig. 2.5 shows a comparison of a conventional granular media and two bit patterned media bit cells.

## Media Reversal

The field required to reverse a single grain or media island is denoted as media switching field  $H_{\text{sw}}$ . In reality this quantity is not constant throughout all grains or islands, as fabrication tolerances introduce slight changes in the material composition, bit size and position. Therefore this field  $H_{\text{sw}}$  is often represented as switching field distribution (SFD) with a certain standard deviation  $\sigma_{\text{sw}}$ . This will be important for the computation of media switching probabilities ( $p_{\text{sw}}$ ) [58] later on.

The magnetization of a bit or grain can reverse either in a homogeneous or inhomogeneous way. The reversal type depends on the magnet's size (particle diameter  $D$ ), shape and the material dependent critical diameter for uniform rotation  $D_{\text{crit}}$ , as formulated by Brown [59] and Kronmüller [60]. In Fig. 2.7 the nucleation field and reversal type as function of the particle diameter is presented.

**Homogeneous reversal** occurs for sufficiently small particles with a diameter below  $D_{\text{crit}}$ . There is no energetically favorable state in which opposing magnetic domains separated by domain walls would form in such a particle. The domain wall energy is proportional to the surface area of the domain wall inside a magnetic specimen.

Whether the particle reverses uniformly or by an expansion of a nucleated domain depends on the critical diameter  $D_{\text{crit}}$  [61], which is proportional to the exchange length  $l_{\text{ex}} = \sqrt{\mu_0 A_{\text{ex}} / J_s^2}$ . The main variables required to describe uniform reversal in a magnetic particle are shown in Fig. 2.6. The energy  $E$  of that magnetic particle with a defined easy axis  $\vec{k}$  under the influence of an externally applied magnetic field  $H_{\text{ext}}$  can be written as:

$$E = -\mu_0 H_{\text{ext}} M_s \cos \theta + K \sin^2(\varphi - \theta) \quad (2.3)$$

Where  $M_s = J_s / \mu_0$  and the angles  $\varphi$  and  $\theta$  are the angles enclosing the external field direction and the anisotropy axis  $\vec{k}$ , and the external field and the magnetization vector  $\vec{m}$ , respectively.  $\mu_0$  is the permeability constant in vacuum ( $\mu_0 = 4\pi \times 10^{-7} \text{m kg s}^{-2} \text{A}^{-2}$ ). If  $\varphi = \theta$  the second term of the right hand side in Eq. (2.3) vanishes and the energy term trying to align the magnetization with the external field remains.

The domain wall energy is proportional to the domain wall surface area or the particle diameter squared. In sufficiently small particles less energy is needed for uniform rotation than forming a domain wall inside. Due to exchange interactions the particle's magnetic moments  $\vec{m}$  simultaneously align with the externally applied magnetic field  $H_{\text{ext}}$ . Such a magnetic specimen is in a single domain state.

Switching occurs at the value of  $H_{\text{ext}}$  that makes the first and second derivative of  $E$  with respect to  $\theta$  zero.

The Stoner-Wohlfarth model suggests an external magnetic field angle  $45^\circ$ ,  $\phi = \pi/4$ , at which the switching field is one half the media's anisotropy field  $H_{\text{ani,media}}$  without affecting the bit's thermal stability.

**Inhomogeneous Reversal** can be observed for larger particles above a critical diameter  $D_{\text{crit}}$  (shown in Fig. 2.7). At intermediate particle size magnetization reversal

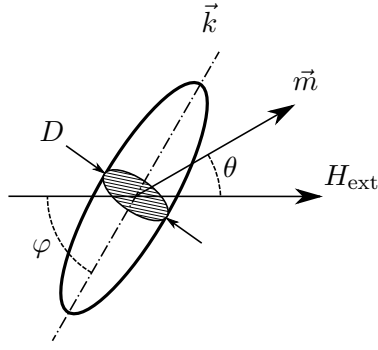


Figure 2.6: Stoner-Wohlfarth particle with a diameter  $D$ . The magnetization  $\vec{m}$  and the easy axis  $\vec{k}$  relative to an external applied field  $H_{\text{ext}}$  are expressed with the angles  $\theta$  and  $\varphi$  respectively.

will occur by curling, a nonuniform magnetic state reduces the magnetostatic energy during magnetization reversal. High aspect ratio particles reverse by the nucleation and expansion of a reversed domain.

The wall propagation field  $H_{\text{wall}}$  can be written as follows:

$$H_{\text{wall}} = \frac{1}{2\mu_0 M_s} \frac{\partial E_{\text{wall}}}{\partial z} \quad (2.4)$$

where

$$E_{\text{wall}} = 4\sqrt{A_{\text{ex}}K_u(z)} \quad (2.5)$$

Note, that in Eq. (2.5) the intrinsic anisotropy constant  $K_u$  is written as a function of the media's height  $z$ .  $A_{\text{ex}}$  is the exchange stiffness constant of the media, which will be explained in more detail in Chapter 4. Nonuniform rotation and expansion of a reversed domain can be enforced in composite media where magnetically soft and hard materials are combined (see Fig. 2.8b). This has been investigated for example by D. Hahn et al. [62] where the reversal behavior and required switching field changes by a gradually increasing anisotropy designed along the media's height. Such media is called graded media and it belongs to the group of exchange spring media (see Fig. 2.8c). They emphasized, that the domain wall propagation field has to be matched with the write field profile of a potential recording head in order to optimize their interplay.

The motivation of using exchange coupled composite (ECC) media is the reduction of the required switching field while keeping the thermal stability almost constant [15, 64–66]. In Fig. 2.8 the media dot in the middle represents such an exchange coupled composite structure. On the bottom a strongly anisotropic material is used, which is also referred to as the "storage layer". It can keep the information due to thermal stability. The layer above is soft magnetic and dubbed as "assisting layer". The soft layer will reverse at lower external field and a domain wall between those two layers will form. The stray fields from the soft layer assists then the depinning of the domain wall trough the hard layer[67], which

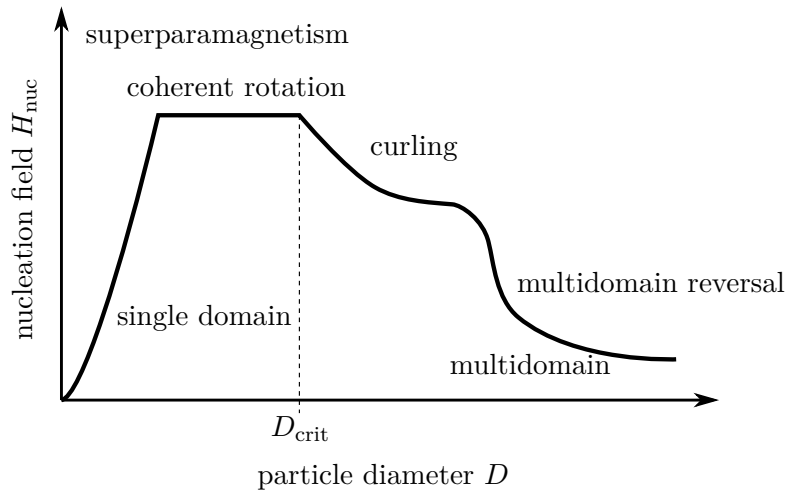


Figure 2.7: Nucleation field as a function of particle size, showing superparamagnetism, coherent rotation, curling and multi domain reversal. The nucleation field is an upper limit of the coercivity. Caption and illustration taken and adapted from [63].

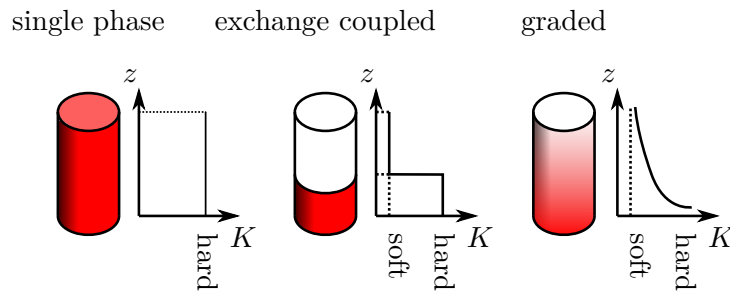


Figure 2.8: Three different media types each with a different anisotropy distribution along the media height. (a) Single phase media, (b) exchange coupled media and (c) graded media. Figure reproduced from [69].

needs less field than reversing a single domain particle as shown in Fig. 2.7. The switching field of such a composite cylinder can be estimated with a proposed model of Kalezhi et al. [67, 68]. Fine tuning both layers' material parameters and the exchange coupling in between allows a switching field reduction of one fifth of the initial anisotropy field of the media [66]. One promising ECC application might be a new media type suitable for microwave assisted magnetic recording [49, 52], as shortly outlined in Section 2.2.

### 2.3.2 Recorder and Recording Schemes

**Ring-Shaped Electromagnet with Airgap** is formed by the main pole and yoke surrounded by the coil, through the media and the soft underlayer back to the main pole via the return pole. By applying a current to the coils the main pole saturates. Through

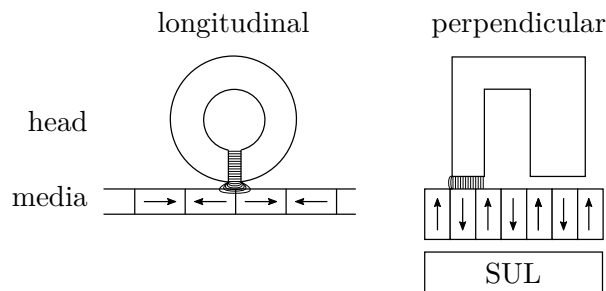


Figure 2.9: Left: In longitudinal recording the magnetization is reversed with the fringing field of the ring head. Right: In perpendicular recording the media is effectively placed in the air gap between main pole and soft under layer (SUL).

the soft under layer, which is a soft magnetic layer below the actual information layer, the flux is returned to the return poles. The surface area of the return pole facing the media has to be large as the flux should not be able to reverse any grains or bits in this area [63, pp. 530]. Besides the reader shields, the coils, main pole, yoke, soft under layer and return pole are the magnetically active parts during recording and are illustrated in Fig. 2.1b.

**Magnetic Spacing** The magnetic spacing refers to the distance between the head's air bearing surface and the magnetic layer. The air bearing surface denotes the pole tips surface facing the media. In [70] the minimum achievable distance of 6.5 nm is mentioned, considering the presence of surface roughness, a media-protection layer, lubricant and space for a few gas molecules.

### Recording Orientation

**Longitudinal** Previous magnetic recording systems stored the bits by magnetizing the bit cells in in-plane direction, either in positive or negative down-track direction, of the media (see Fig. 2.3 and 2.9). The recording head design has been different in contrast to today's perpendicular recording systems. The material of the longitudinal media was a composition of Co, Cr, Ta, Pt and B. In Fig. 2.9 both recording orientations are shown.

**Perpendicular** To increase areal density, Iwasaki proposed in 1975 to record the bit cells by magnetizing them in out-of-plane direction of the media [71]. This had the advantage of having less demagnetizing effects from neighboring bit cells and a higher areal density as compared to longitudinal recording. Still the recording head design and the reader elements had to be improved. For example the introduction of a soft underlayer was necessary to provide a flux return path back to the return poles of the write head. It took another 30 years, around 2005 to 2008, until this technology was mature enough for the industry to make the transition from longitudinal to perpendicular recording. The media's material is a composition of Co, Cr, Pt and Oxides [72]. Nowadays conventional

recording refers to perpendicular magnetic recording with a single pole head writing on granular media and reading with a giant magneto-resistive [73] reader stack, tunnel magnetic resistance [74] or spin orbit torque heads [75].

## Perpendicular Magnetic Recording Schemes

Design parameters of the recording head and media are usually optimized for one of three different writing schemes: Centered writing, staggered writing and shingled writing. These different writing schemes are especially of interest for bit patterned magnetic recording. Fig. 2.10 illustrates the three different writing schemes above a bit patterned media layout.

**Centered** Centered writing is the classical writing scheme and focuses on one track in the center only. Usually the smallest pole tip width allowed by the fabrication resolution dictates the track width on granular media. The recording head is centered above a single track. Having very slim pole tips comes with a disadvantageous decrease in write field strength.

**Staggered** Another clever way is to allow a pole tip width which covers two tracks and recording on it as it would be a one single but much denser track. This scheme is called staggered [76] and comes with additional requirements for the media, reader and recorder. This scheme allows an additional areal density increase of around 5–10 % governed by allowing the usage of harder media material. To sufficiently write on the same bit patterned media, the write head has to switch much faster in order to switch only one underlying bit.

**Shingled** Introduced by Wood et al [29, 70], this approach increases the effective field exerted on the medium by increasing the pole tip width even more. By writing in an overlapping manner like placing shingles onto a rooftop you can further increase the hardness of the media, consequently allowing a higher areal density.

### 2.3.3 Read Head

The reader or read-back of written bits is not considered within this work but a description of its functionality is added here for completeness.

Previously in longitudinal magnetic recording the reader used the magneto-resistive effect as shown in Fig. 2.3. As the name already implies, the change of electrical resistance in the reader element mainly governed by changes of the felt stray field can be measured. The relative change of electric resistance is in the range of 0.125 % to 0.25 % [77]. To get picked up by the read head, either the stray fields exerted by the magnetic transition must be relatively high or the gap between reader element and media surface must be very small (e.g. as in tape recording). With the discovery of the giant-magneto-resistive (GMR) effect in the late '80s [10, 11], read heads with much higher sensitivity were developed which replaced previous read heads in the late '90s. GMR read heads comprise

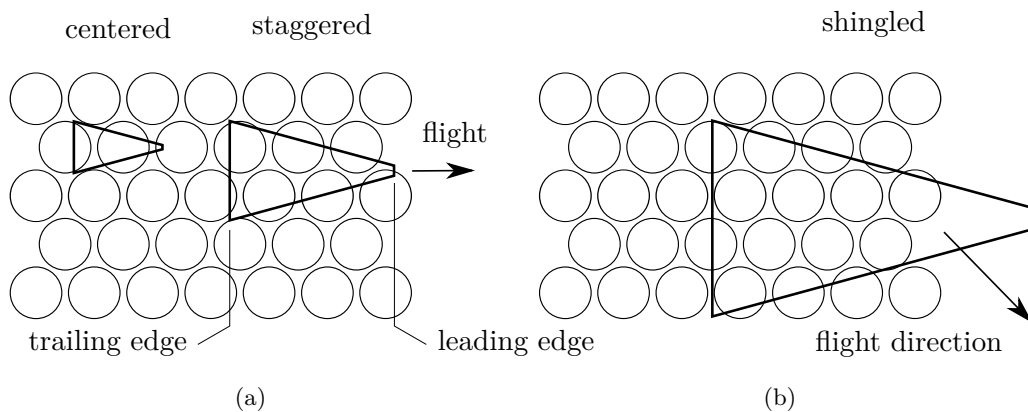


Figure 2.10: (a) Centered, staggered and (b) shingled magnetic recording scheme above a triangular bit patterned media layout. The bold lines indicate the air bearing surface of the corresponding write head. Here, the flight direction always goes from left to right, which means that the short edge of the pole tip represents the leading edge and the opposite, long one is the trailing edge. The trailing edge can be seen as the actual writing edge.

a thin film stack of alternating ferromagnetic and non-magnetic layers which show huge resistance changes due to changes of the media's stray field. The relative change of electric resistance of GMR heads typically increases by a factor of ten as compared to magneto-resistive heads [26, p. 81]. This opened up the opportunity to make more sensitive magnetic field sensors. The sensor itself is referred to as reader-stack, consisting of multiple different layers between two Cu leads which transfer the sensing current over the actuator arm to the hard disc's driver. Such a GMR reader-stack is illustrated in Fig. 2.11. This sensor stack consists of a *pinning layer*, *reference layer*, an insulator and a *free layer*. The pinning layer is strongly anti-ferromagnetically coupled with the reference layer with its magnetization pointing along cross-track direction. These two layers act as a stabilized reference magnetization for the free layer. The sensing current flows through the reference layer and the free layer. The free layer is picking up the stray field induced by the magnetization configuration coming from the underlying media surface. The angle between the magnetization of the free layer and the reference layer is proportional to the resistance. Therefore with changing stray field, the resistance and sequentially the sensing current changes.

As the free layer should only pick up fields from below its current position, the reader stack has to be surrounded by large micron scaled shields. These reduce the influences of other fields in cross- and down-track direction onto the free layer.

Another important aspect of the free layer is, that this layer has no favored magnetization direction. It's a magnetically "soft" layer (low  $K$  or  $K = 0$ ). There is a small chance that this layer flips its magnetization direction, which would result in read errors. This can be stabilized with a so-called *hard bias* magnet placed along the reader stack in cross-track direction. This magnet induces an additional guiding field for the free layer in case the layers magnetization direction displacement gets too large.



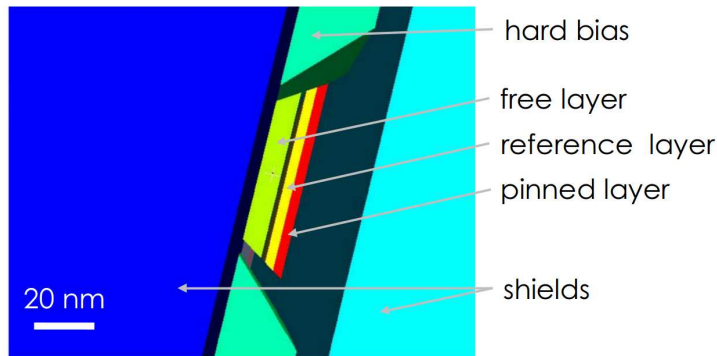


Figure 2.11: A finite element model of a perpendicular read head is shown. A thin GMR reader stack consisting of a free layer, a reference layer and a pinned layer. On the sides of the stack the hard bias can be seen. The big shields protect the reader stack from unwanted stray fields.

For tunnel magnetic resistance (TMR) the Cu layer is replaced by a non-conductive thin oxide layer. With TMR heads the signal amplitude could be tripled as compared to GMR heads [26, p. 81].

### 2.3.4 Writer Shields

The writer shields main objective is to protect regions of the media, which shall not be written by the recording head field. Thus, the shields narrow down the spatial distribution of the write field or in other words narrow down the writing window [78].

Mallary et al. [79] emphasized the importance of shielding as areal densities in hard drives increased further. They simulated the effect of shields and their gap distances to the pole tip. A trailing shield drastically increases the write field gradient compared to an unshielded monopole head, allowing for a much higher density of write transitions. By fine tuning the write head's geometry with respect to the side shields, the overall available write field is reduced, but the bit cells in neighboring tracks are better protected against unintentional switching [79, 80]. Fig. 2.2 shows a wrap-around shield which combines trailing shield and side shields in a single soft magnetic layer. Further reading about shield variations can be found in [81, p. 147, Fig. 3.7].

### 2.3.5 Skewing and Pole Tip Taper Angle

The term skewing describes the rotation of the air bearing surface relative to the media surface. This rotation occurs because the recording head is mounted on the actuator arm which has a different rotation center than the tracks on the medium. Fig. 2.12 shows magnified selections of the air bearing surface of write heads with the underlying bit pattern of the medium, at the outer most track (lower row) and inner most track (upper row). Comparing the track directions, denoted by the dot-dashed lines, between

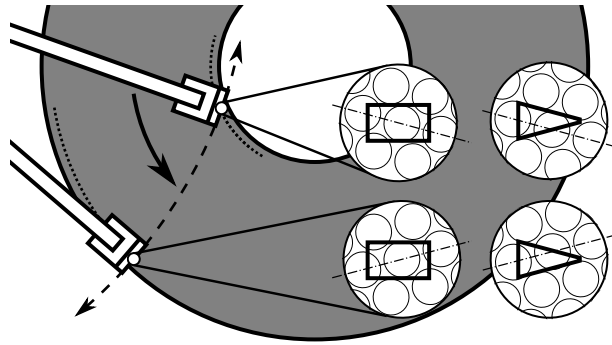


Figure 2.12: A recording head's air bearing surface rotates relative to the media surface. This becomes mostly relevant at the inner or outer most track of the hard drive disc. On the left side a rectangular shaped head profile is shown which is not considering this rotation and therefore would overwrite adjacent information. On the right hand side a tapered head is shown, perfectly fitting in-between the neighboring tracks.

the two actuator positions a significant rotation occurs with respect to the write head. A rectangular write head, shown in the left column of the selections, would overwrite adjacent tracks. A tapered head with a taper angle of  $15^\circ$ , shown in the right column, avoids this writing error. This is later taken into account in Chapter 7 and could be included into the optimization process, but is kept constant within this work. A useful schematic and a more in-depth view can be found in [82].

### 2.3.6 Recording Errors and their Occurrences

On a granular media, if one grain of a bit cell is not correctly switched, the reader would still pick up the transition with a slightly lower signal compared to a perfect transition. The noise in the read-back signal originating from the media's granularity [70] can be corrected by the design of the read head and medium. In contrast, if an island of a BPM gets written with wrong polarity, it is an erroneous bit. The switching field distribution of the media and the write and read synchronization becomes more relevant in bit patterned magnetic recording [83, pp. 252]. Different approaches will be described and explained in more detail in Section 5.1, Section 6.1.3 and 7.1.4. Albrecht et al. [57] assumed that a write error rate below  $10^{-2}$  is well recoverable with the employment of error correcting codes at the expense of additional storage overhead.

# Global Optimization Method

## Contents

---

3.1	Search Strategies . . . . .	24
3.2	Conclusion . . . . .	31

---

This chapter briefly explains terms of optimization and provides a more in-depth view of the methods used in this work. It starts with a formal description of an optimization problem, followed by a discussion about sampling methods and what methods would be better than just sampling. A more elaborate introduction to optimization algorithms may be found in [84].

In general an optimization consists of several evaluations of the objective function wherein one or multiple inputs are tested iteratively until one or multiple outputs of that function meet a predefined requirement. A requirement would be, for example minimize cost or maximize efficiency. The number of input and output dimensions will be denoted as  $k_{in}$  and  $k_{out}$  respectively. A deterministic function  $f(\cdot)$  maps the input values  $(y_1, y_2, \dots, y_{k_{in}})$  into output values also called responses  $(r_1, r_2, \dots, r_{k_{out}})$  which can also be written as  $f : \mathbb{R}^{k_{in}} \mapsto \mathbb{R}^{k_{out}}$ . The input and output values are usually described as vectors by

$$\begin{aligned}
 (y_1, y_2, \dots, y_{k_{in}})^T &= \mathbf{y} \in \mathbb{Y}^{k_{in}} \subseteq \mathbb{R}^{k_{in}} \text{ and} \\
 f(\mathbf{y}) = (r_1, r_2, \dots, r_{k_{out}})^T &= \mathbf{r} \in \mathbb{R}^{k_{out}}.
 \end{aligned}$$

$\mathbb{Y}$  is a subset of possible input values which constrain the optimization. This subset could represent e. g. fabrication ranges or can simply narrow down the design space region.  $\mathbb{Y}$  should be a convex, closed and solid space.

Typically a constrained optimization problem is formulated as

$$\text{minimize } f(\mathbf{y}) \tag{3.1}$$

$$\text{subject to } g_j(\mathbf{y}) \leq 0, \quad j = 1, 2, \dots, m. \tag{3.2}$$

In words, find a  $\mathbf{y}$  minimizing the objective or cost function  $f(\mathbf{y})$  while satisfying the conditions  $g_j(\mathbf{y})$ , where  $m$  is the number of applied conditions. The optimization's goal is defined by the objective function (3.1). This function has to be deterministic, meaning that its inputs are transformed into non-random outputs. The above mentioned restrictions are referred to as inequality constraint functions (3.2).

As the optimization itself is an iterative search for the perfect choice of input parameters an additional index (i) as superscript  $\mathbf{y}^{(i)}$  or  $\mathbf{r}^{(i)}$  is introduced denoting the current iteration where  $i = 1, 2, \dots, n$ . After an unknown amount of iterations the input vector which fulfills the objective in (3.1) following the boundary conditions from (3.2) will be denoted with  $\mathbf{y}^*$  and the resulting solution as  $\mathbf{r}^*$ .

Within this work one evaluation of  $f(\mathbf{y})$  is very time consuming, as it involves the construction, the mesh generation of a complex geometry and a finite element micromagnetic simulation. Two approaches with multiple input parameters are tested trying to grasp the full performance of the investigated system.

In Chapter 6 an approach with multiple objective functions to optimize a system is used. In this approach we maximize the effective write field and the write field gradient under the constraint that the effective write field at the adjacent track is smaller than media switching field. A self-updating weighted sum of responses is applied to combine multiple objectives and assess a calculated design.

The second approach is presented in Chapter 7, where the write error rate is used as a single objective function.

Several methods are suitable for exploring such a set of design parameters. The kind of search strategy – that is most suitable – depends on the balance between computational power and the degree of detail we want to describe and understand the recording system.

### 3.1 Search Strategies

In case of global optimization the worst-case path towards an optimal solution requires a large number of evaluations which scale exponentially with the parameter space dimensions  $k_{\text{in}}$  [20]. In order to understand the behavior of changes in all of those input dimensions different approaches are applied.

**Parameter Study** One way is to systematically test every possible parameter combination in a discretized parameter space within a certain range by constructing a multi-dimensional grid with equidistant grid points. This sampling method has the highest computational cost but will provide the most insight. It is suitable for studies involving design evaluations with low computational costs and low dimensional design space. The number of evaluations increases exponentially with the number of input parameters  $k_{\text{in}}$ .

**Random Sampling** Testing a random set of input numbers until the objective value is quantitatively improved is another time-intensive strategy. No intelligent search strategy

is applied but it is suitable if the computational time of each evaluation is very low. It is also called Monte Carlo Sampling.

**Meta Models** If the computational cost is high, a full parameter study in a high dimensional parameter space  $\mathbb{Y}^{k_{\text{in}}}$  with  $k_{\text{in}} > 3$  will be too time consuming to find the best set of design parameters.

As a rough estimate of the response space between evaluations, the already computed results can be fitted with a mathematical function, e.g. with a spline or a polynomial. Often referred to as response surface method too. This approximation is called meta modeling [85, 86]. By using meta models the computation time is reduced, hence more local or global optimization steps can be done. It can be used as a guide for possible optima candidates and to make an estimation where to find a better design compared to the current best one. As the response surface method describes the currently available evaluations with a mathematical function, the gradients can be easily computed and used for steepest descent methods to find minima and maxima. Although meta models allow computationally less expensive search towards an optimum, they require an already well explored parameter space without missing nonlinearities within that space. This is one common drawback of above mentioned random sampling approach as an evenly distributed set of input values is only reached after a very large number of evaluations.

However, the initial training set is a critical part. If the response for example is very noisy or very non-uniformly distributed, the surface interpolation of the response function might be strongly underrepresented by the interpolating surface. This would lead to an inefficient search.

**Optimized Latin-hypercube Space Filling** A nearly uniform distribution of input values throughout even high dimensional design spaces ( $k_{\text{in}} \geq 10$ ) is achieved by using an optimized Latin hyper-cube space-filling method [87, 88]. It is an expansion of common Latin Hyper Cube space filling with an additional quantity like entropy, discrepancy and minimax or maximin distances to be optimized. In order to get a representative amount of initial data points for the meta model, a rule of thumb states, that at least ten times  $k_{\text{in}}$  initial design points should be evaluated [89, 90]. This method is applied for the sake of producing a non-biased initial data set.

Standard random sampling produces a non-biased data set much faster in contrast to the optimized Latin-hypercube space filling method for problems of high dimensionality. This is because random sampling does not require knowledge about previous sampling points, whereas the Latin-hypercube sampling method does. Samples of the Latin-hypercube space filling method have in common that they do not share any individual coordinate which cannot be ensured with random sampling. In Fig. 3.1 fifty initial samples are produced with random Monte-Carlo and optimized Latin-hypercube sampling methods for comparison. One can see that clusters of sample points appear in random sampling in contrast to Latin-hypercube sampling.

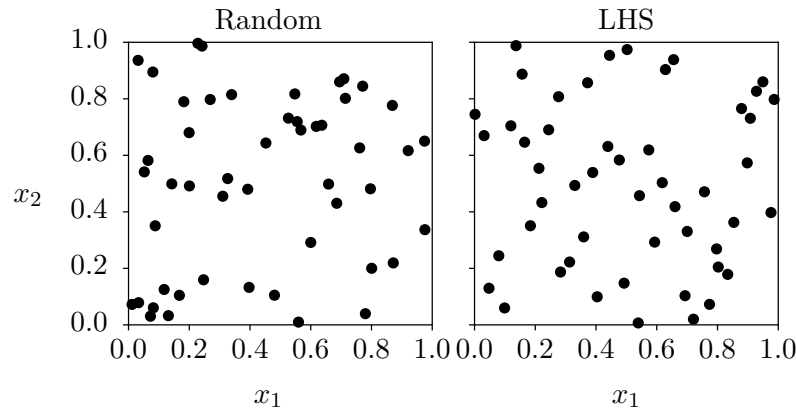


Figure 3.1: Fifty sampling points of a two-dimensional design space once sampled with a random uniform sampling strategy and once sampled with the optimized Latin-hypercube sampling (LHS) method.

**Meta Model with Uncertainty Measurement** Uncertainty measures help to iteratively improve a meta-model. In order to estimate the uncertainty evaluations of the objective functions are described by the mean value  $\mu^{(i)}$  and its deviation  $\sigma^{(i)}$ . The index (i) denotes the iteration number of successive function evaluations. Two evaluations located "close" to each other are assumed to show similar response values. Each already evaluated design point is defined with zero uncertainty. The uncertainty  $\sigma^2$  is defined to increase with distance  $d$  from already evaluated points whereas the mean value is derived from a simple approximating method. The measure of distance between those already evaluated design points act as a quantity of a prediction uncertainty. In contrast Linear Regression-Methods assume that each prediction error is independent from others [85, p. 4].

This idea is related with the term *kriging*. Kriging is an adjusted Gaussian Process regression method for Geology applications predicting locations of Gold with a small number of drill holes in a region in South Africa which dates back to the 60's. The method is similar to a response surface approach but describing the function space with a Gaussian process  $(\mu, \sigma^2)$ .

The uncertainty of prediction increases in unexplored regions. In an iterative process different strategies can be applied to find the point where the objective function should be evaluated at the next iteration. One strategy could be to evaluate the objective function at the point of maximum uncertainty. Another possibility is to evaluate the next point where the objective function where the current best design point can be improved. In a Gaussian process model not only a measure of uncertainty is tracked, but also needed information to compute the probability of improving the current best available design.

**Efficient Global Optimization** Efficient Global optimization evaluates the objective function at points where the expected improvement function is maximal. *The following*

part is a description of this algorithm from [85] reformulated with a slightly modified test example. This algorithm is implemented within the open-source optimization tool dakota [91] and is abbreviated with EGO. The algorithm in dakota initially fills the parameter space with an optimized Latin-Hypercube space filling method. After this setup phase the algorithm sequentially evaluates the point which currently maximizes the expected improvement function (EIF). The number of initial samples is recommended to be  $10k_{\text{in}}$  and can be computed in parallel. The sequential evaluation is then repeated until a previously defined number of maximum iterations is exceeded or no further improvement – in a certain tolerance spectra – can be found. In [91] the importance to understand the mechanism of maximizing the expected improvement function is emphasized. The authors also provide a good explanation of this method. By evaluating the current point at the highest improvement probability a trade-off mechanism between evaluating design points (i) promising of overcoming the current best design and (ii) evaluating design points in unexplored regions is introduced. They claim that this prevents the search algorithm from stopping at local minima which still strongly depends on the smoothness of the response space. However such a Gaussian regression method is performing better than gradient-based methods for problems with noisy responses. The authors in [85] propose that "EGO's methodology is especially good at modeling the non-linear, multi-modal functions that often occur in engineering".

In Figures 3.3 to 3.6 the functionality of Gaussian process optimization is illustrated. In this example the parameter space  $x \in \mathbb{R}$  is continuous and one-dimensional and so is the response space  $y(x) \in \mathbb{R}$ . The parameter space is constrained to the range  $0 \leq x \leq 13$ . The purpose of this example is on one hand to demonstrate how the algorithm basically works and on the other hand how it scopes with badly distributed initial training points. We assume the space filling method evaluated the first six design points in an uneven manner, as shown in Fig. 3.3 with black circles. The unknown function has been evaluated at  $x = 1, 2, 3, 4, 8, 12$ .

The black solid line in Fig. 3.3 shows the currently estimated mean response value  $\mu = \mu(x)$  which maximizes the likelihood function

$$\frac{1}{(2\pi)^{n/2} (\sigma^2)^{n/2} |\mathbf{R}|^{1/2}} \exp \left[ -\frac{(\mathbf{y} - \mathbf{1}\mu)^T \mathbf{R}^{-1} (\mathbf{y} - \mathbf{1}\mu)}{2\sigma^2} \right], \quad (3.3)$$

a  $\mathbf{1}$  is an  $n$ -vector of ones and  $n$  is the number of evaluations already carried out.  $\mathbf{y}$  is a vector which gathers the already computed values of the objective function for the design points collected in the vector  $\mathbf{x}$ . The mean response value  $\mu$ , its standard deviation  $\sigma$  and other unknowns in  $\mathbf{R}$  have to be optimized.  $\mathbf{R}$  is the correlation matrix formed by already observed design evaluations. Its components are acquired with

$$R_{ij} = \exp \left[ -d \left( \mathbf{x}^{(i)}, \mathbf{x}^{(j)} \right) \right]. \quad (3.4)$$

Each  $(i, j)$  entry is the error correlation between observed design points, as shown in Fig. 3.2.

The distance is computed with

$$d(\mathbf{x}^{(i)}, \mathbf{x}^{(j)}) = \sum_{h=1}^k \theta_h |x_h^{(i)} - x_h^{(j)}|^{p_h} \quad (\theta_h \geq 0, p_h \in [1, 2]), \quad (3.5)$$

where  $\theta_1, \dots, \theta_k$  and  $p_1, \dots, p_k$  inside the correlation matrix  $\mathbf{R}$  are tuning parameters required to be optimized for the likelihood function of Eq. (3.3). Fig. 3.2 gives two examples of error correlation functions with different  $\theta$ . Note that  $\mathbf{x}$  is written in vector form with  $k_{\text{in}}$  dimensions.

The model – as described in [85, pp. 460] – optimizes  $2k_{\text{in}} + 2$  parameters, where two of them are the mean response value  $\mu$  and its variance  $\sigma^2$  from (3.3). The other parameters  $\theta_1, \dots, \theta_{k_{\text{in}}}$  and  $p_1, \dots, p_{k_{\text{in}}}$  are inside the  $n \times n$  correlation matrix  $\mathbf{R}$ . Each  $(i, j)$  entry corresponds to the error correlation which is exponentially proportional to a weighted distance function between  $n$  design points, as shown in Fig. 3.2 and defined in Eq. (3.5) and Eq. (3.4).

The weights  $\theta_h \in \mathbb{R}_0^+$  are proportional to the "activeness" of the design parameters. The parameters  $p_h \in [1, 2]$  select between the Manhattan distance and the Euclidean distance measure. The current approximation of the mean response function value  $\mu$  and its variance  $\sigma^2$  is computed as

$$\mu = \frac{\mathbf{1}^T \mathbf{R}^{-1} \mathbf{y}}{\mathbf{1}^T \mathbf{R}^{-1} \mathbf{1}} \quad (3.6)$$

and

$$\sigma^2 = \frac{(\mathbf{y} - \mathbf{1}\mu)^T \mathbf{R}^{-1} (\mathbf{y} - \mathbf{1}\mu)}{n}. \quad (3.7)$$

This variance  $\sigma^2$  of the predicted response appears in Fig. 3.3 as green solid line. This is the main benefit of describing the function space with a Gaussian Process. To

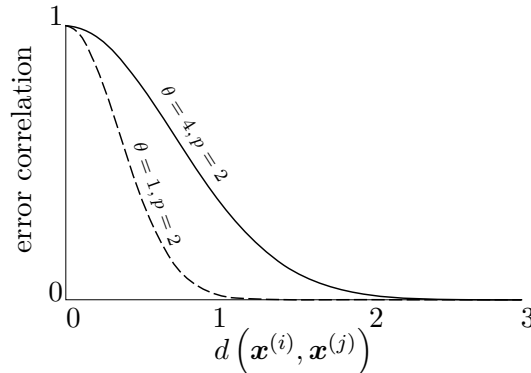


Figure 3.2: Example of error correlation between two points  $\mathbf{x}^{(i)}$  and  $\mathbf{x}^{(j)}$  with  $(\theta = 1, p = 2)$  as solid line and  $(\theta = 4, p = 2)$  as dashed line. Figure reproduced from [85, Fig. 1 p. 459]



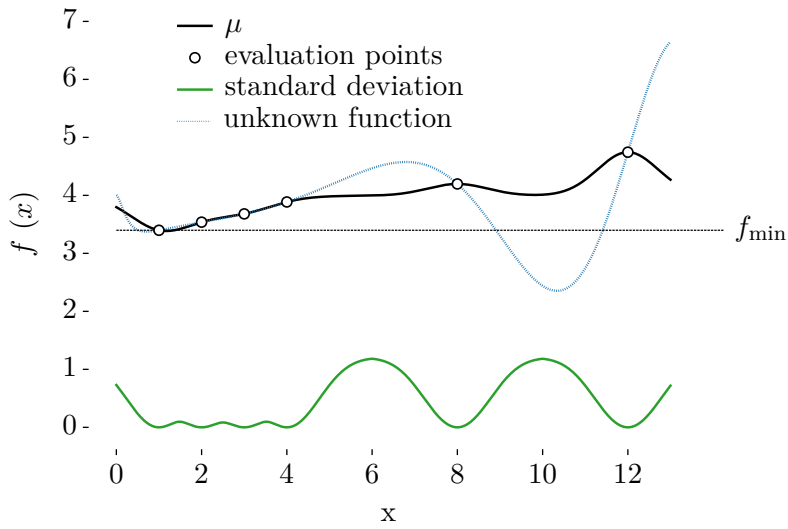


Figure 3.3: The design space is already evaluated at six data points shown as circles. The black solid line shows the computed mean value in Eq. (3.6) and the green solid line represents the variance from Eq. (3.7). The dotted blue line shows the actual response function  $f(x) = x \sin x$  unknown for the optimizer. (Efficient global optimization example compiled and adapted from [85, Fig. 8 and 9].)

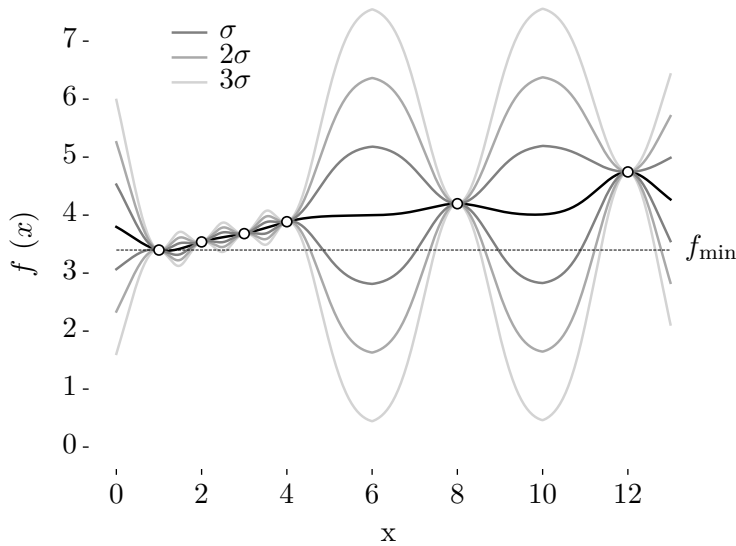


Figure 3.4: The prediction uncertainty highlighted as contours of one, two and three times the standard deviation  $\sigma$  along the predicted mean value  $\mu$  as solid black line.

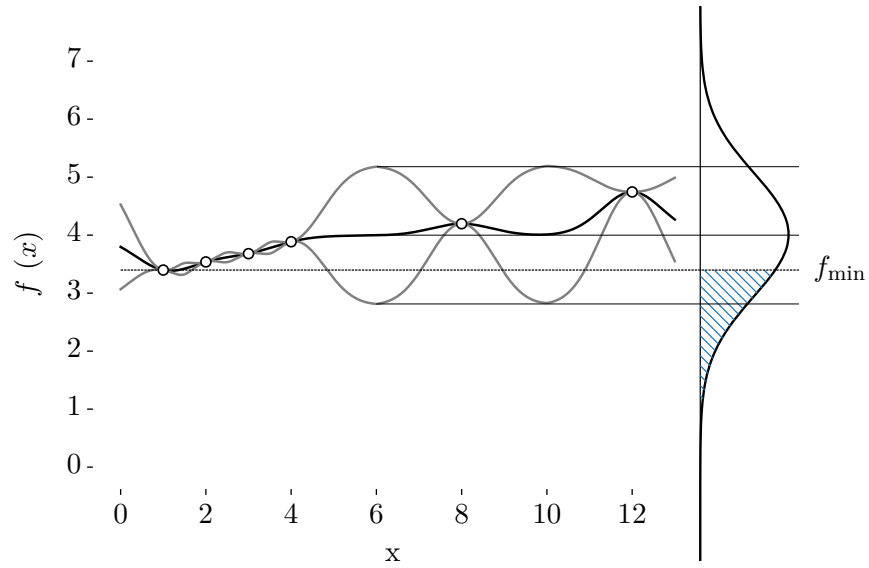


Figure 3.5: The expected improvement function is proportional to the probability of overcoming the current min ( $\mu$ ). Here at the right hand side the uncertainty for the prediction at  $x = 6$  is shown. The shaded area, which can be computed from the error function  $(f_{\min} - \mu) / (\sigma\sqrt{2})$ , here shown in blue is related to the expected improvement.

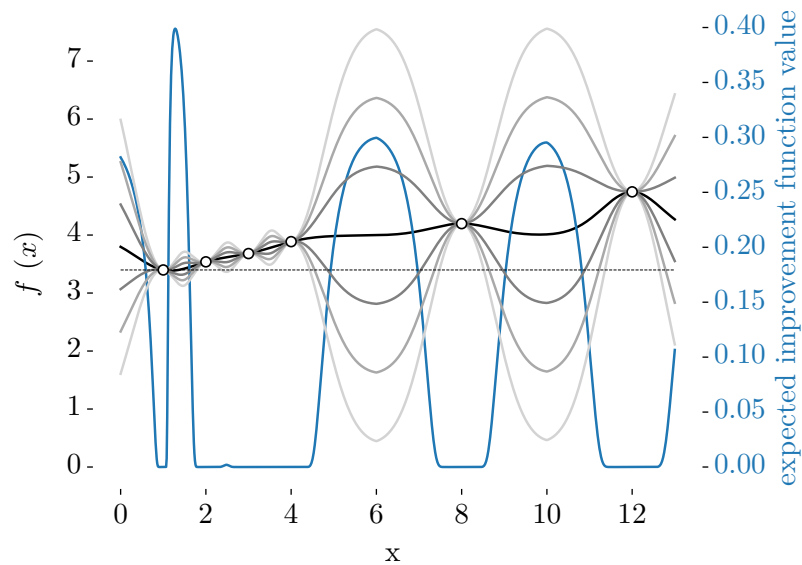


Figure 3.6: The current mean and uncertainty are shown in black and gray, similar to Fig 3.4. Now in blue the expected improvement function is plotted on a second axis (right). Between the evaluation points 1 and 2 the expected improvement maximizes. This will be the next evaluation point for the optimizer.

highlight the error of the estimation  $\mu$ , the unknown function is shown as a blue fine dotted line.

To make the view of the optimizer more clear we draw the uncertainty in Fig. 3.4. Here we see  $\mu$  as black line and one, two and three standard deviations as gray scaled lines from dark gray, gray and light gray respectively. The currently best design point marked with  $f_{\min}$  has been found at  $x = 1$ .

Now the expected improvement function is basically the probability of overcoming the current best design point  $f_{\min}$  with

$$\text{EIF}(\mathbf{x}) = (f_{\min} - \mu) \Phi\left(\frac{f_{\min} - \mu}{\sigma}\right) + \sigma \phi\left(\frac{f_{\min} - \mu}{\sigma}\right), \quad (3.8)$$

where the functions  $\Phi(\cdot)$  and  $\phi(\cdot)$  are the cumulative and the probability density functions, respectively [85]. An example is presented in Fig. 3.5 showing the distribution function for the certain point at  $x = 6$ . The blue patterned surface area on the right hand side is proportional to the probability of overcoming the currently best objective function value  $f_{\min}$ .

Fig. 3.6 shows the computed expected improvement function from Eq. (3.8) in blue on the right axis. The computed expected improvement shows three peaks, one lies between the evaluated points at  $x = 1$  and  $x = 2$ , another one with lower expected improvement between  $x = 4$  and  $x = 8$  and the third one between  $x = 8$  and  $x = 12$ . At each evaluated point the prediction uncertainty is zero and therefore the expected improvement is zero too.

At point  $x = 1.3$  as shown in Fig. 3.6 which is located near an already evaluated point  $x = 1$  the prediction uncertainty is increased. The expected improvement function maximizes at this point. Therefore the next response evaluated  $f(1.3)$  will turn out to be slightly better than the current  $f_{\min}$  and  $f_{\min}$  will be updated. Afterwards the response approximation  $(\mu, \sigma^2)$  and  $\text{EIF}(\mathbf{x})$  will be recomputed proposing either a point close to  $x = 6$  or  $x = 10$  which are regions lesser explored than others. The evaluation at  $x = 10$  will later lead to a much better response value and the model will end up close to the global minimum.

## 3.2 Conclusion

In this work each design evaluation is very costly to compute. Additionally the dimension of the parameter space is high, as we want to improve many geometrical features for a magnetic recording head at once. We want to have a method which finds minima/maxima in a small number of simulations ( $< 100$ ). Effective Global Optimization (EGO) as described above is a promising tool for optimizing expensive black box functions. Later in this work in Chapter 6 we also used SHERPA (Simultaneous Hybrid Exploration that is Robust, Progressive and Adaptive) for a constrained multi-objective approach where those objectives are combined within a weighted sum. SHERPA is a commercial software tool [92] that switches between various optimization methods adaptively. In Chapter 7 we combined the above described method EGO with our design evaluation.

No matter how promising those methods are, one has to consider that a certain noise level, a low number of initial training points or a lack of any systematic trend in the response might reduce the efficiency of the algorithm to a random search method [86].

# Micromagnetic Background

## Contents

4.1	Introduction . . . . .	<b>33</b>
4.2	Total Gibb's Free Energy . . . . .	<b>35</b>
4.2.1	Zeeman Energy . . . . .	35
4.2.2	Exchange Energy . . . . .	35
4.2.3	Anisotropy Energy . . . . .	36
4.2.4	Demagnetizing Energy . . . . .	37
4.3	Exchange lengths . . . . .	<b>38</b>
4.4	Magnetization Dynamics . . . . .	<b>39</b>
4.5	Energy barrier estimation . . . . .	<b>40</b>

## 4.1 Introduction

Kronmüller and Fähnle illustrated in [60, p. 6, Fig. 1.1] the interdisciplinary cooperation between micromagnetism and quantum theory (see Fig. 4.1). It is highlighted that micromagnetism tries to answer questions of material synthesis and constitution while quantum theory characterizes microstructure, delivers important intrinsic magnetic material properties and most importantly for micromagnetics, forms the basis to describe the effects in ferromagnetism. Micromagnetics is a suitable tool to investigate magnetic recording processes but also helps to understand intrinsic reversal processes and microstructural influences in permanent magnets or other magnet applications.

In micromagnetic theory the investigated length scales lie between nm and  $\mu\text{m}$ , being large enough to classically represent atomic spins and still small enough to resolve magnetic domains. Classically, in the sense of not resolving individual spins, but more a cluster of multiple spins which are oriented in the same direction due to the assumption of strong internal forces in the magnet. For the numerical solution of the micromagnetic equation the ferromagnetic object has to be spatially discretized. Clusters of multiple

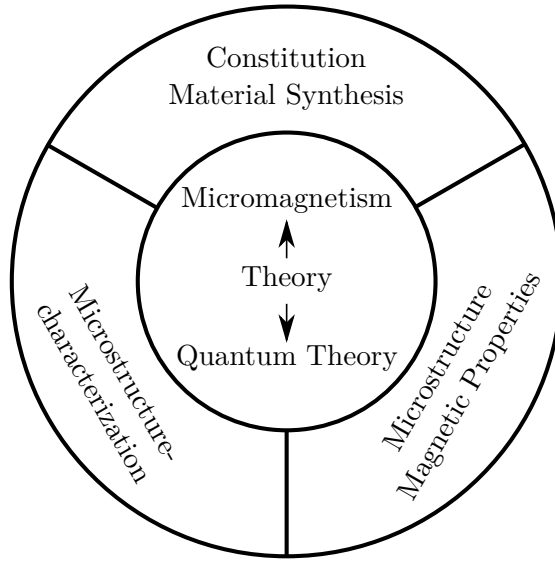


Figure 4.1: Scheme of interdisciplinary cooperation for developing and analyzing magnetic materials. Reproduced from [60, p. 6, Fig. 1.1].

spins with similar orientation are represented by a unit vector for each computational cell or for each node point of a finite element mesh, respectively.

This assumption holds for a sufficiently discretized geometry, where the mesh size has to be in the range of the exchange length scale  $l_{\text{ex}}$  of the investigated magnetic material.

The mesh size of such a geometry discretization is therefore a very important parameter which will be discussed more in Section 4.3. Too large mesh sizes lead to unacceptable discretization errors not capable of resolving domain walls.

In micromagnetic theory the magnetization is described as a classical three dimensional continuous vector field with space coordinates  $\mathbf{x} \in \mathbb{R}^3$  as  $\mathbf{M}(\mathbf{x})$  which approximates the discrete distribution of magnetic moments well enough. Each  $i$ -th vector  $\mathbf{M}(x_i)$  approximates an averaged atomistic magnetic moment divided by its corresponding finite element volume  $dV$ .

In general magnetization  $\mathbf{M}(T)$  is temperature dependent, but this work covers only constant temperatures through space and time. Temperature is implicitly considered within intrinsic material properties given by measurements at certain temperatures. Those intrinsic material properties are the magnetocrystalline anisotropy constant  $K$ , exchange stiffness  $A_{\text{ex}}$  and saturation polarization  $J_s$ . These values can be obtained via elaborate experiments or computed with ab-initio methods like the density functional theory. At constant temperature the length of each magnetization vector is normalized with the material's saturation magnetization  $\mathbf{m}(\mathbf{x}) = \mathbf{M}(\mathbf{x}, T = \text{const.}) / M_s(T = \text{const.})$ , therefore  $|\mathbf{m}(\mathbf{x})| = 1$ . For the sake of readability from now on  $\mathbf{m}(\mathbf{x})$  is denoted as  $\mathbf{m}$ .

In thermodynamic equilibrium a ferromagnetic object's most probable state can be described by the minimum of its Gibb's free energy  $E_{\text{tot}}$ .

## 4.2 Total Gibb's Free Energy

We have four major energy contributions, which are the exchange energy  $E_{\text{exc}}$ , describing the misalignment of neighboring spins, the magnetocrystalline anisotropy energy  $E_{\text{ani}}$ , describing a favored spin orientation due to the stray field energy, which is also called dipolar energy  $E_{\text{dip}}$ , describing the magnets self-demagnetization and the Zeeman energy  $E_{\text{zee}}$ , corresponding to the energy related to an externally applied magnetic field acting on the magnet

$$E_{\text{tot}} = E_{\text{exc}} + E_{\text{ani}} + E_{\text{dip}} + E_{\text{zee}}. \quad (4.1)$$

### 4.2.1 Zeeman Energy

The energy of a magnetization in an external field  $\mathbf{H}_{\text{ext}}$  is the Zeeman energy. By integration over the energy density

$$E_{\text{ext}} = -\mu_0 \int M_s (\mathbf{m} \cdot \mathbf{H}_{\text{ext}}) dV. \quad (4.2)$$

This energy defines the macroscopic potential for manipulating the magnetic state of the magnet with an external field.

### 4.2.2 Exchange Energy

There are several approaches to calculate the exchange energy (i) the Heisenberg model and (ii) the band-theory of ferromagnetism [93]. The former assumes localized magnetic moments, i.e. spins are fixed at certain crystallographic lattice positions, whereas the latter does not. With the Heisenberg model the exchange energy of two neighboring spins is

$$\phi_{i,j} = -2J_{ij}S_i \cdot S_j. \quad (4.3)$$

$S_i$  and  $S_j$  are the spin quantum numbers for the atoms  $i$  and  $j$  and  $J_{ij}$  is the exchange integral. The exchange integral depends on the state of the electron shell and the atomic core distances. The sign of this quantity determines if the spin coupling is parallel or anti-parallel [94, pp. 242]. In solid state physics we want to determine the exchange energy considering all spin pairs of a magnetic sample which is a non-trivial task for large systems. But it is possible to approximate  $J_{ij}$  such that it is constant for the next and next next neighboring spins while farther away it can be zero. With a so-called continuum approximation the spins are treated as classical normalized spin vectors  $m$ . Under the assumption that misalignments between neighboring spins are always small we can write the exchange energy like

$$E_{\text{ex}} = \int A_{\text{ex}} (\nabla \mathbf{m})^2 dV. \quad (4.4)$$

The exchange stiffness constant can then be expressed as  $A_{\text{ex}} = 2JS^2z/a$ , where  $J$  is now the constant exchange integral,  $z$  the number of neighbors depending on the crystal structure,  $a$  the lattice constant and  $S$  the spin quantum number.

### 4.2.3 Anisotropy Energy

Anisotropy is the property of being directional. In relation to hard magnetic materials, the magnetocrystalline anisotropy is one of the most important intrinsic properties of a magnet. The crystal structure of a ferromagnetic specimen defines which magnetization direction is most preferable in terms of energy. This direction, if one-dimensional, is often referred to as easy axis. The anisotropy energy is expanded in terms of the projection ( $\mathbf{m} \cdot \mathbf{k}$ ) of the magnetization  $\mathbf{m}$  onto the easy axis  $\mathbf{k}$ . For uniaxial magnetocrystalline anisotropy parallel orientation is the energetically favored state. Comparing the magnetic system to a mechanical system one could imagine the anisotropy energy as a rotational spring which is rotated out of its equilibrium state. For small rotations the energy is proportional to the deviation angle squared scaled by the spring constant  $K_1$ . The first anisotropy constant of a material composition is important for micromagnetic simulations, but difficult to estimate. It can be determined experimentally by measuring the anisotropy-dependent torque of a magnetized specimen as described in [95].

This preference of a certain magnetization direction has its roots from spin-orbit interactions. Electrons are linked to the crystal structure (also called crystal field) and their interactions with the spins, which let the spins align to well-defined crystallographic axes [96, pp. 84]. This crystal field depends on the crystal structure itself.

#### Hexagonal Crystals

Materials with a hexagonal crystal structure show a uniaxial anisotropy, where (4.5) shows the first two terms of a series expansion with  $K_1$  and  $K_2$ . The odd magnitudes of  $\cos \theta$  contributions vanish. In a uniaxial crystal the  $c$ -axis is an easy direction for  $K_1 > 0$  and  $K_2 > 0$  or  $K_1 > -K_2$  and  $K_2 < 0$  [60]. A uniaxial crystal shows an easy plane if  $K_1 < -K_2$  and  $K_2 < 0$  or  $K_1 < -2K_2$  and  $K_2 > 0$ . Fig. 4.2 shows the energy density of a uniaxial crystal for an easy axis and an easy plane.

The anisotropic contribution to the energy density can be written as

$$\varepsilon_u = K_1 \sin^2 \theta + K_2 \sin^4 \theta = K_1 (1 - m_z^2) + K_2 (1 - m_z^2)^2 \quad (4.5)$$

where  $\theta$  denotes the angle between the magnetization vector  $\mathbf{m}$  and the easy axis  $\mathbf{k}$ . In (4.5)  $\mathbf{k}$  is aligned in  $z$ -direction.  $K_1$  and  $K_2$  are constants which can be obtained by ab-initio calculations or better by experiments. Often the effect of  $K_2$  is neglected in micromagnetic simulations of ferromagnetic materials, when its absolute value is much smaller than  $K_1$ . Summing up the squared angles between  $\mathbf{k}$  and  $\mathbf{m}$  over the whole discretized ferromagnetic specimen with uniaxial anisotropy and neglecting the second anisotropy constant  $K_2$  gives us an anisotropy energy of

$$E_{\text{ani}} = - \int K_1 (\mathbf{k} \cdot \mathbf{m})^2 dV. \quad (4.6)$$

In the above equation constant terms that do not depend on  $\mathbf{m}$  have been dropped.



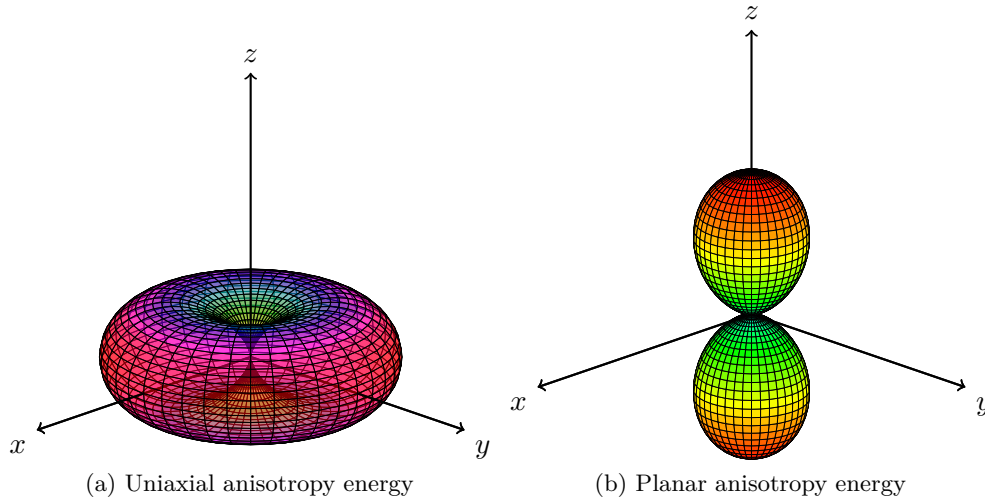


Figure 4.2: Anisotropy energy of hexagonal crystal structure with  $c$ -axis equal to  $z$  and (a)  $K_1 > 0$ : uniaxial anisotropy, (b)  $K_1 < 0$ : easy-plane anisotropy.

### Cubic crystals

For a cubic lattice, on the other hand, more than one crystallographic directions can be easy axes. Depending on the signs and relative magnitudes of the anisotropy constants  $K_1$  and  $K_2$  the preferred directions are either the axes or the diagonal of the cubic unit cell. The anisotropy energy density can be written in component form as

$$\varepsilon_c = K_1 (m_x^2 m_y^2 + m_y^2 m_z^2 + m_z^2 m_x^2) + K_2 m_x^2 m_y^2 m_z^2. \quad (4.7)$$

#### 4.2.4 Demagnetizing Energy

"Demagnetizing fields and stray fields arise whenever the magnetization has a component normal to an external or internal surface. They also arise whenever the magnetization is nonuniform in such a way that  $\nabla \cdot \mathbf{M} \neq 0$ ." [63, p.231]

While no external field acts, we can state together with the equation for flux density  $\mathbf{B} = \mu_0 (\mathbf{H} + \mathbf{M})$  and Gauss's law for magnetism  $\nabla \cdot \mathbf{B} = 0$

$$\nabla \cdot \mathbf{H}_{\text{demag}} = -\nabla \cdot \mathbf{M}. \quad (4.8)$$

The vector field  $\mathbf{H}_{\text{demag}}$  is rotation free ( $\nabla \times \mathbf{H}_{\text{demag}} = 0$ ) which will be ensured by defining it as a gradient of a magnetic scalar potential  $\nabla \phi_m$ . In order to receive a scalar potential satisfying Poisson's equation we put  $\mathbf{H}_{\text{demag}} = -\nabla \phi_m$  into (4.8):

$$\nabla^2 \cdot \phi_m = \nabla \cdot \mathbf{M} = -\rho_m \quad (4.9)$$

This equation holds in the entire space which includes the magnet's domain, giving

$$\nabla^2 \phi_m = \begin{cases} \nabla \cdot \mathbf{M} & \text{inside the magnet} \\ 0 & \text{elsewhere.} \end{cases} \quad (4.10)$$

From  $\nabla \cdot \mathbf{B} = 0$  all incoming flux  $\mathbf{B}_{\text{in}}$  normal to the magnet's surface has to be equal to all outgoing flux  $\mathbf{B}_{\text{out}}$  normal to the magnet's surface.

$$\mathbf{B}_{\text{in}} \cdot \mathbf{n} = \mathbf{B}_{\text{out}} \cdot \mathbf{n} \quad (4.11)$$

$$(\mathbf{H}_{\text{in}} + \mathbf{M}) \cdot \mathbf{n} = \mathbf{H}_{\text{out}} \cdot \mathbf{n} \quad (4.12)$$

$$(-\nabla \phi_{\text{in}} + \mathbf{M}) \cdot \mathbf{n} = -\nabla \phi_{\text{out}} \cdot \mathbf{n} \quad (4.13)$$

$$\mathbf{M} \cdot \mathbf{n} = (\nabla \phi_{\text{in}} - \nabla \phi_{\text{out}}) \cdot \mathbf{n} \quad (4.14)$$

We can express the stray field energy contribution with known magnetization configuration  $\mathbf{M}$  and the surface normals  $\mathbf{n}$ .

$$E_{\text{stray}} = -\frac{\mu_0}{2} \int_{\Omega} \mathbf{H}_{\text{demag}} \cdot \mathbf{M} dV = \frac{\mu_0}{2} \int_{\Omega} \nabla \phi_m \cdot \mathbf{M} dV \quad (4.15)$$

In order to compute the magnetic scalar potential one can either solve Poisson's equation (4.9) numerically or use the analytic expression for the magnetic scalar potential given below. The scalar potential, due to a limited magnetized volume [63, p.46] and application of Green's function is

$$\phi_m(\mathbf{x}) = \frac{1}{4\pi} \left( \int_v \frac{\rho_m}{|\mathbf{x} - \mathbf{x}'|} d^3 \mathbf{x}' + \oint_{\partial v} \frac{\sigma_m}{|\mathbf{x} - \mathbf{x}'|} d^2 \mathbf{x}' \right), \quad (4.16)$$

where  $\sigma_m = \mathbf{n} \cdot \mathbf{M}$  represents the magnetic surface density and  $\rho_m = -\nabla \cdot \mathbf{M}$  the magnetic charge density.

Within this work the solution of Poisson's equation for  $\phi_m$  is computed with the finite element method. The determination of the stray field energy is usually more complicated in comparison to all other mentioned energy contributions because an open boundary problem is involved [97]. The scalar potential  $\phi_m$  has to converge to zero at infinite distance. This would require a spatial discretization even outside of the magnet's domain. However, Fredkin and Köhler proposed a hybrid finite element/boundary element method in [98] which does not require the surrounding space of the magnet to be resolved by the finite element model. The computation with the magnetic scalar potential underestimates the magnetostatic energy the larger the mesh sizes in the discretized magnet are [99].

The contribution of  $H_{\text{demag}}$  usually complicates the determination of the energy minimum but cannot be neglected as demagnetization is often the main source of reversal, which prefers to start at corners, edges or other defects/inhomogeneities, where those fields are the largest.

### 4.3 Exchange lengths

In micromagnetics the Gibb's free energy has to be spatially discretized with the finite element method (FEM) or finite difference method (FDM). Depending on the curvature

of a magnet's geometry one method might be more suitable than the other. Within the presented work the magnetization states of recording head structures are computed on a tetrahedral finite element mesh. The mesh quality affects the solvers convergence.

One assumption in micromagnetism is the parallel alignment of the spins throughout each single finite element cell. The spin inhomogeneities are resolved by the so-called exchange lengths [60, p. 357]. This length should be considered as an upper bound for the spatial discretization of the finite element mesh. The following length in Eq. (4.17) defines the Bloch wall parameter  $\delta_0$  and (4.18) gives the exchange length, which is proportional to the Néel wall width. Both values are related to the intrinsic material properties of the magnetic specimen, whereas the former is related to magnetocrystalline anisotropy, the latter to demagnetization.

$$\delta_0 = \sqrt{\frac{A_{\text{ex}}}{K_1}} \quad (4.17)$$

$$l_{\text{ex}} = \sqrt{\frac{A_{\text{ex}}}{M_s J_s}} \quad (4.18)$$

The discretization has to be the minimum of both of those exchange lengths. If the mesh size is chosen larger, it won't be possible to resolve domain walls and their motion through the magnet correctly. Usual mesh sizes of hard ferromagnetic materials are around 1 nm to 3 nm.

## 4.4 Magnetization Dynamics

If the magnet reaches a relaxed state, an energy minimum, the torque on all magnetic moments vanishes. This can be written as Brown's equation [100]

$$\mathbf{m} \times \left( 2A_{\text{ex}} \nabla^2 \mathbf{m} + 2K_1 \mathbf{k} (\mathbf{m} \cdot \mathbf{k}) + J_s \mathbf{H}_{\text{demag}} + J_s \mathbf{H}_{\text{ext}} \right) = 0. \quad (4.19)$$

The term in brackets divided by  $J_s$  has the dimension of a magnetic field. Therefore it is called effective field  $\mathbf{H}_{\text{eff}}$ . The effective field

$$\mathbf{H}_{\text{eff}} = -\frac{\delta E_{\text{tot}}}{\delta \mathbf{m}} = \frac{2A_{\text{ex}}}{J_s} \nabla^2 \mathbf{m} + \frac{2K_1}{J_s} \mathbf{k} (\mathbf{m} \cdot \mathbf{k}) + \mathbf{H}_{\text{demag}} + \mathbf{H}_{\text{ext}}, \quad (4.20)$$

is the sum of the exchange field, the anisotropy field, the demagnetizing field and the external field. The effective field is of essential importance for magnetization dynamics.

The change of the micromagnetic normalized magnetization  $\mathbf{m}(\mathbf{x})$  over time

$$\frac{\partial \mathbf{m}}{\partial t} = -|\gamma| (\mathbf{m} \times \mathbf{H}_{\text{eff}}) + \alpha \left( \mathbf{m} \times \frac{\partial \mathbf{m}}{\partial t} \right) \quad (4.21)$$

is described with the Gilbert equation [101, 102]. Here  $\gamma$  is the gyromagnetic ratio and  $\alpha$  a phenomenological damping parameter introduced by Gilbert in order to describe a constant energy dissipation. Fig. 4.3 shows both terms separately and in their combined

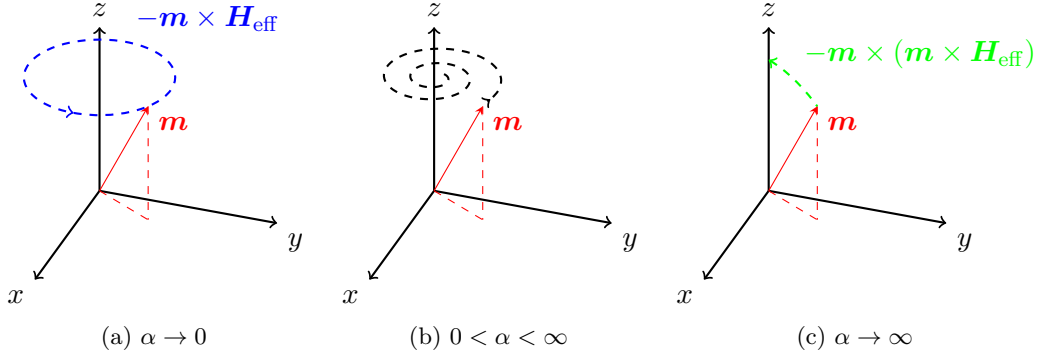


Figure 4.3: (a) Precessional motion around effective field vector  $\mathbf{H}_{\text{eff}}$  in this case acting in positive  $z$  direction, (c) the motion towards effective field vector and (b) both terms active.

form. The change of  $\mathbf{m}$  over time can also be written in the Landau-Lifshitz-Gilbert form as

$$\frac{\partial \mathbf{m}}{\partial t} = \underbrace{-c \mathbf{m} \times \mathbf{H}_{\text{eff}}}_{\text{precession}} - \underbrace{\alpha \mathbf{m} \times (\mathbf{m} \times \mathbf{H}_{\text{eff}})}_{\text{damping}}. \quad (4.22)$$

The prefactor

$$c = \frac{|\gamma|}{1 + \alpha^2} \quad (4.23)$$

in both terms is just covering constants for clarity, which can be later used as time scaling factor for time integration. Now damping is applied to both terms but differ in orders of magnitude. The right-hand side of (4.22) and (4.21) consists of two terms: (1) the precessional term, describing the rotational motion of a magnetic moment  $\mathbf{m}$  around that effective field  $\mathbf{H}_{\text{eff}}$  and (2) the damping term, describing the motion of the magnetic moment towards the effective field. For small  $\alpha$  damping is negligible and the precessional term dominates. The effects of this energy dissipation are still not fully understood [103, 104]. This phenomenological damping parameter was first introduced by Landau and Lifshitz. They introduced it to damp the magnetic system into the next energy minimum. The damping constant on its own scales how fast the magnetization  $\mathbf{m}$  gets pulled towards an acting field. Choosing a large damping constant would speed up the computation of relaxed magnetization states, if the dynamics in reaching such a state are not of interest.

## 4.5 Energy barrier estimation

An energy barrier is a barrier between two states with specific energies. In some applications of micromagnetics it might be important to know the minimum energy

barrier between a particle or magnet magnetized up and down. Since we can accurately describe the two states in micromagnetism, we only need to calculate the most likely path between these points through the energy landscape in order to make a statement about the required energy that is needed to jump from one energy minimum to the other. An estimate of that barrier can be used to calculate the transition probability from one state to another as Néel-Brown's theory suggests [105].

One way to micromagnetically estimate the required energy to overcome an energy barrier between two local energy minima is the nudged elastic band method, first introduced by Henkelman and Jónsson in [106] and applied in micromagnetic systems by Dittrich [107]. This method requires an exact description of both states and an initial guess for an energy path between those states. The initial path is represented by a sequence of magnetization states, also called images, along that path. This path is usually set as a straight line between those states. With an iterative approach each of these states will be relaxed in order to receive a path with lower energy barrier between above mentioned magnetization states compared to the previous path. This is repeated until the gradient of the energy is pointing parallel to the path's direction and the perpendicular energy gradient vanishes.

The energy landscape of a micromagnetic system depends on many parameters, such as the microstructure, intrinsic material parameters and external influences, such as an externally applied field. As a result, there are many local minima. With this method, however, two or more images can fall into the same energy minima. This leads to a reduced resolution of the energy landscape and a greater inaccuracy to predict the energy barrier.

By connecting the images like a chain of springs, or more precise like a nudged elastic band, the acting spring force keeps them away from each other, preventing clustering of multiple images in a single energy valley. However, this spring constant, which distributes all images evenly along the path, is unknown. The spring constant is an adjustable parameter which depends on the number of images, the size of the geometry and the number of finite elements.

Another, but very similar method is called the String-method [107–111], where images are kept equidistant with a slightly different approach. The String-method uses the full length of the energy path and divides it into a user-defined number of equidistant segments. Each new sampling point is moved downhill by a small step then the sampling points are interpolated on the path in order to achieve equidistant sampling. This process will be repeated until the energy gradients run parallel to the path or no energy difference with a predefined  $\epsilon$  as tolerance can be seen.

This method is more convenient as it guarantees evenly distributed images without the need of finding appropriate spring constants.



Die approbierte gedruckte Originalversion dieser Dissertation ist an der TU Wien Bibliothek verfügbar.  
The approved original version of this doctoral thesis is available in print at TU Wien Bibliothek.

# Initial Investigations

## Contents

5.1	Write field computation . . . . .	43
5.2	Manual Optimization . . . . .	46
5.3	Results and Discussion . . . . .	47
5.3.1	Centered Recording . . . . .	47
5.3.2	Staggered Recording . . . . .	48
5.3.3	Shingled Recording . . . . .	50

The effective write field and its gradient are key properties for successful writing on bit patterned media. Here we compute the effective write field profile for all major writing schemes and perform manual optimization of the write head geometry. The writing schemes: centered, staggered and shingled, are described in Fig. 2.10. The dependence of the write field profile on different coil currents, side shield gaps and media depths are presented.

For the centered writing scheme investigation of the effective field profile according to changes of side shield gaps of 20 nm, 10 nm and 5 nm are carried out. For staggered writing the field profile changes triggered by an increase of the side shield gap. Gap distances of 20 nm, 25 nm and 30 nm are investigated.

By matching the write field with the media values for the media anisotropy are derived and bit life times are estimated.

Magnetic recording terminology used in this chapter is explained in Ch. 2.

## 5.1 Write field computation

This section explains how micromagnetic simulations are used to evaluate the write field.

Before we are able to perform a micromagnetic simulation we have to define a domain where the computation of magnetization dynamics take place. This is done with a

Python script receiving these input design parameters. It constructs a full write head geometry with the computer aided design software SALOME [112]. This script meshes the geometry with a fine mesh size of 2.5 nm near the pole tip and coarser at the rest of the head. The meshing is done by the open-source program Netgen [113].

Within one micromagnetic simulation the write head's magnetization is relaxed for a time period of 2 ns. Afterwards we saturate the magnetic head by applying an 80 mA coil current pulse with a rise time of 0.1 ns.

According to the coil currents direction and the coils orientation a magnetic field is emitted. This field saturates the pole tip to the wanted magnetic field direction.

Note, that the main pole might still be in a multi domain state. And the write current pulse is mostly inducing a field to the main pole in order to push the currently preferred domain into the pole tip. The perpendicular component of the head magnetization only at the small pole tip has to either point in positive or negative  $z$ -direction. The domains forming and moving in the return poles, yoke and main pole far away from the media surface do not contribute much to the effective write field. Multi domain states are briefly explained in Section 2.3.1 in relation to incoherent media reversal behavior.

Within realistic hard drives the recording head won't see such a simple rectangular current pulse. Normally the current even overshoots in order to accelerate the reversal process of the head. The head reversal time strongly depends on the chosen material and geometry of the yoke and the head itself [114]. In this work the magnetic field below the head during recording is of interest, which allows us to neglect an accurate simulation of the magnetization dynamics of the whole recording head, return poles and soft under layer.

Keeping the write current applied for 2 ns, we compute the magnetic stray field below the pole tip inside a predefined rectangular grid, also referred to as *field box*. The resolution of the box was 2.5 nm in each spatial direction where its size covers two cross track pitches and three down track pitches. For a quick field estimation a two step process is applied [115]: (i) First we evaluate the magnetostatic scalar potential at the surface of a predefined field box using hybrid finite element/boundary element solver [98]. (ii) Then a fast Poisson Solver is used to compute the scalar potential inside the box and the magnetostatic field is computed by numerical finite differences.

Fig. 5.1 illustrates the write field of the predefined box located between the pole tip and the soft underlayer. The two extracted lines (dot-dashed colored red and green), which are used to evaluate the recording performance of its corresponding recording head geometry at the target track and the adjacent track. The field box data consists of a field vector for each cell. It is stored in an unstructured grid format. With the open-source multi-platform data analysis and visualization application ParaView [116], we compute the effective field with the directional field components inside the box similar to [117]:

$$H_{\text{eff}} = H_{\text{tot}} \left[ \sin^{\frac{2}{3}}(\Theta) + \cos^{\frac{2}{3}}(\Theta) \right]^{\frac{3}{2}} \quad (5.1)$$

where  $H_{\text{tot}}$  is the Euclidean norm of all directional components

$$H_{\text{tot}} = \sqrt{H_x^2 + H_y^2 + H_z^2} \quad (5.2)$$



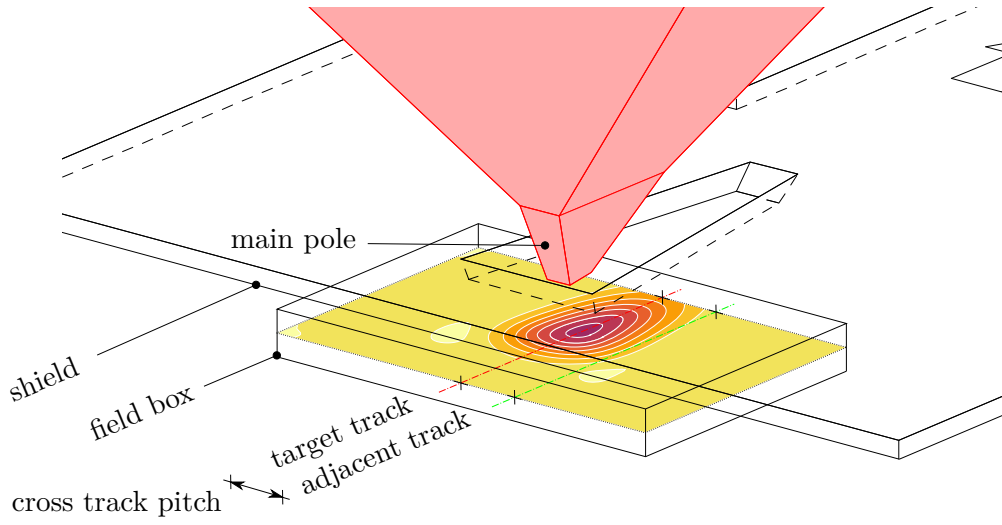


Figure 5.1: Micromagnetic setup and evaluation regions. The main pole in red and shield contours. The field box is the area in which the Poisson equation of the scalar potential is solved. The dot-dashed lines inside this field profile slice highlights the center of the target and adjacent track.

and the field angle  $\Theta$  between the media's easy axis and field vector

$$\Theta = \arctan \left( \sqrt{\frac{H_x^2 + H_y^2}{H_z^2}} \right) \quad (5.3)$$

The effective field  $H_{\text{eff}}$  is the stray field scaled by the field angle dependent Stoner-Wolfarth model as shown in Fig. 5.2. When maximizing the effective field at the target track angles around  $45^\circ$  have to be favored whereas  $30^\circ$  or  $60^\circ$  result in a scaling factor of 1.9 instead of 2. The usage of an effective field term allows direct comparison with the media anisotropy field.

Note that the size of the field box in Fig. 5.1 is much larger for illustration purpose only. During optimization the field box's size is reduced to a much smaller region to optimize physical memory occupation for evaluation. Accidentally magnetic domains may form in the shields. The associated domain walls would emit perpendicular stray fields towards the media capable of switching bits.

The intrinsic material parameters applied for the main pole represent CoFe having an exchange coupling constant  $A_{\text{ex}} = 20.15 \text{ pJ m}^{-1}$ , a saturation polarization  $J_s = 2.4 \text{ T}$  and an anisotropy constant  $K_1 = 800 \text{ J m}^{-3}$ .

Initially the recording system's magnetization is relaxed for 50 ns with no coil current applied. Afterwards with a rise time of 0.1 ns a target coil current is reached and flows through the coils surrounding the yoke and saturates the pole tip magnetization. Applying three different coil currents 20 mA, 40 mA and 60 mA we investigate the changes

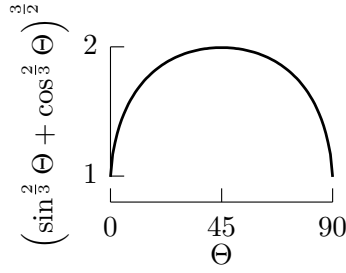


Figure 5.2: Stoner-Wohlfarth effective field scaling factor.  $\Theta$  is angle of the field vector relative to media's easy axis.

in effective field magnitude and gradient. The current is applied with a frequency of 0.5 GHz which translates into a write rate of 1 bit/ns.

## 5.2 Manual Optimization

After simulating four coil current switching events the field profile at 13 nm and 9 nm below the air bearing surface is computed. The different depths shall provide information about the switching probabilities for different media types in which one has a thickness of 10 nm and the other 5 nm. The assumed underlying patterned media layout reflects an areal density of 2.21 Td/in<sup>2</sup> (tera dots per square inch). Each media island has a diameter of 12 nm, a cross-track pitch of 19 nm and a down-track pitch of 16 nm. The saturation polarization is assumed to be  $\mu_0 M_{s,med} = 0.7$  T reflecting a CoCrPt media material [118].

The effective field value which draws a contour, also called a field bubble, on the cross-track down-track plane has a certain width. Matching the cross-track width of the specific recording scheme (shown in Fig. 2.10) gives us a rough estimate of the media's maximum switching field. Fig. 5.3 shows this contour matching in a sketch for a staggered recording scheme. Under the assumption that the media switching field  $H_{sw,med}$  is close to its anisotropy field (as described in Section 2.2) we further can assume the media's anisotropy constant to be  $K_{1,med} \approx \mu_0 M_{s,med} H_{ani,med} / 2$ .

Adjusting the media anisotropy to the write field ensures that we can write the dots on the target track. However, we also have to avoid accidentally switching of dots on adjacent tracks.

The approximated anisotropy field of the media allows an estimation of a zero field energy barrier for a single bit with specific volume  $V$

$$E_{B,0} = K_{1,med} V. \quad (5.4)$$

In order to approximate the adjacent track error rate, we need to estimate the energy barrier of the dot in the fringing field of the head at the adjacent track  $H_{adj}$ . According to Victora [119] the energy barrier for a particle switching by uniform rotation in an

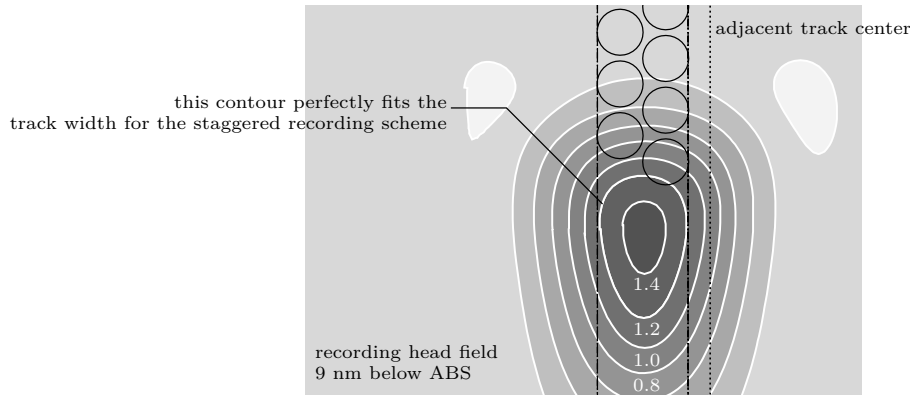


Figure 5.3: The grey-scaled plane shows an example of an effective field profile below 9 nm of the recording head's surface. The white contours and the numbers indicate the field strength in units of Tesla. The field contour which, in this example, fits the track width (dashed lines) of such a bit patterned media layout while planning to write in a staggered manner, is approximately the media's switching field  $H_{sw,med}$  (in this case 1.2 T). The dotted line highlights the center of the adjacent track along down-track direction  $H_{adj}(x)$ .

oblique applied field is given by

$$E_B(x) = E_{B,0} \cdot \left(1 - \frac{H_{adj}(x)}{H_{ani,med}}\right)^{3/2}. \quad (5.5)$$

This approximated energy barrier  $E_B$  of a bit in a neighboring track together with the Arrhenius-Néel's equation gives us the average life time of a bit

$$\tau = \frac{1}{f_0} \cdot e^{\frac{E_B}{k_B T}}. \quad (5.6)$$

Dividing the average life time by the average field exposure time for a bit gives the approximated number of head passes before the bit unintentionally loses its stored information.

## 5.3 Results and Discussion

Field profiles at the target and adjacent track centers are presented according to the different recording types presented in Section 2.3.2.

### 5.3.1 Centered Recording

A recording head with a 12 nm wide pole tip is designed for centered recording according to the above outlined media layout. In Fig. 5.4 the effective fields are computed at two

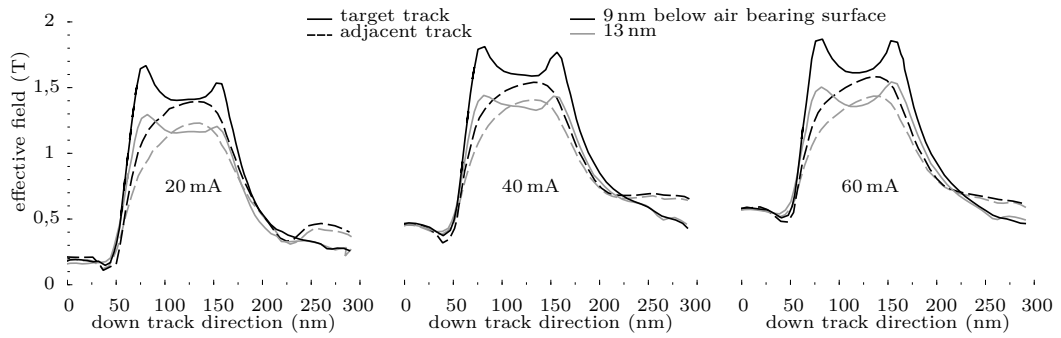


Figure 5.4: A recording head designed for centered recording scheme with a pole tip width of 12 nm, a side shield gap of 20 nm and a trailing shield gap of 20 nm. The effective field within the target and adjacent track is shown 9 nm and 13 nm below the air bearing surface. From left to right three different applied coil currents are compared. The different air bearing surface distances are color-coded and the track line-style coded.

different distances from the pole tip's air bearing surface in order to cover two possible single phase media thicknesses. An increase of the head-media distance by 4 nm translates to 0.5 T field reduction at the target track center and 0.25 T at the adjacent track. The effective field increases with increasing coil current, depicted from left to right. The closer the media can be brought to the air bearing surface, the higher the possible effective fields. 13 nm below the air bearing surface the difference between the maximum field of the adjacent and target track is less than 100 mT. This is not enough as it will cause adjacent track erasure. For this recording head the effective field created by 40 mA or 60 mA coil current are almost the same while a coil current of 20 mA reduces the field from 1.8 T to 1.65 T.

Initially, with a side shield gap of 20 nm, the shield is now brought closer to the pole tip. Fig. 5.5 shows the computed effective fields 13 nm below the air bearing surface for two different coil currents. In the adjacent track at an elevated coil current of 40 mA large fields are still observed, even far behind the recording head. The same occurs at a lower coil current but with a narrow gap between the shield and the recording head. This indicates a reversed domain within the shield increasing the fields inside the adjacent track.

The most promising design is with a current of 40 mA and a side shield gap of 10 nm. Using a media material with an anisotropy constant of  $0.35 \text{ MJ/m}^3$  would have a zero field energy barrier of  $80.9 k_B T$ . The energy barrier in a bit located at the adjacent track is  $22.6 k_B T$  which can be expressed as  $5 \times 10^7$  writing head passes before erasure.

### 5.3.2 Staggered Recording

A staggered recording head is designed with the same geometry as in Section 5.3.1 but in contrast with an increased pole tip width of 19 nm covering two tracks. The effective field

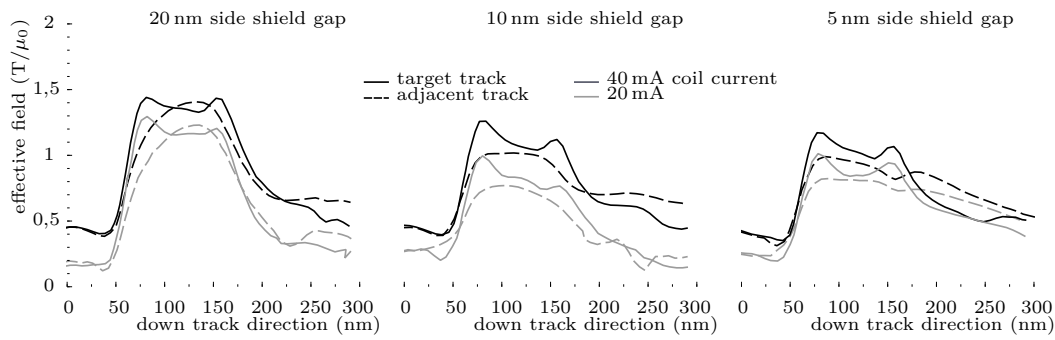


Figure 5.5: A recording head designed for centered recording scheme with a pole tip width of 12 nm and a trailing shield gap of 20 nm. The field is computed 13 nm below the air bearing surface. From left to right the effective field within the target and adjacent track is shown, for 20 nm, 10 nm, 5 nm side shield gap respectively. Dashed lines correspond to adjacent track and solid lines to the target track. The line brightness highlights the different coil currents.

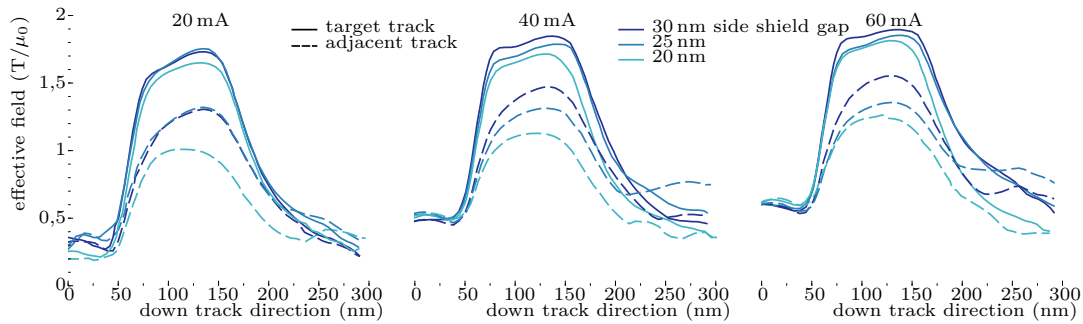


Figure 5.6: A recording head designed for staggered recording scheme with a pole tip width of 19 nm and a trailing shield gap of 20 nm. Field is computed 13 nm below the air bearing surface. From left to right the effective fields within the target track and adjacent track for different coil currents are shown. Different brightnesses of the lines show three different side shield gaps ranging from darkest 30 nm to brightest 20 nm. Solid lines correspond to target track and dashed lines to adjacent track.

is computed 13 nm below the air bearing surface for different applied coil currents and is shown in Fig. 5.6. Additionally the influence of different side shield gaps is investigated. At an 20 mA applied current increased side shield gaps show almost no difference (below 100 mT) at the target track. At the adjacent track a 20 nm distance to the side shield reduces the effective field by 300 mT.

The most promising staggered head design is controlled with 60 mA and has a side shield gap of 20 nm. A media material with an anisotropy constant of  $0.49 \text{ MJ/m}^3$  would have a zero field energy barrier of  $115 k_B T$ . The adjacent track energy barrier is  $48.2 k_B T$

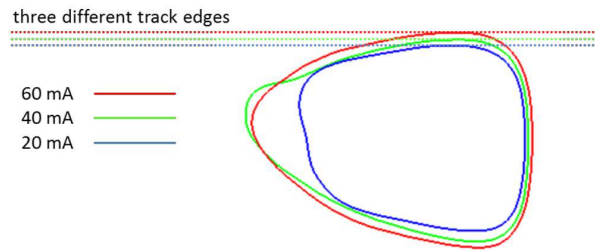


Figure 5.7: Field contour difference with different applied coil currents consequently changing the track edge, at which the effective field has to be evaluated. For shingled writing the side shield is only required at one side, the writing track edge. Therefore the field bubble is asymmetric.

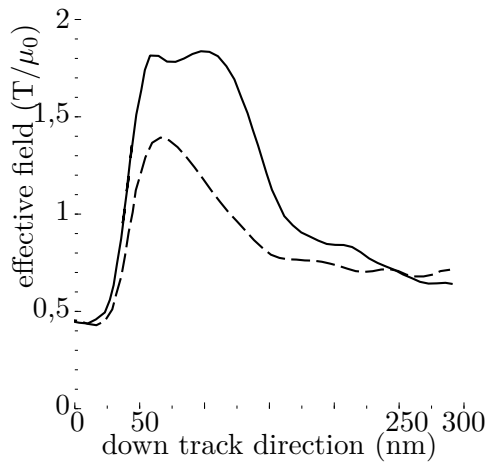


Figure 5.8: A recording head designed for shingled recording scheme with a pole tip width of 80 nm, a trailing shield gap of 20 nm and a side shield gap of 15 nm. Applied coil current was 40 mA. The field is computed 13 nm below the air bearing surface. The solid line corresponds to the field in the target track and the dashed line to the adjacent track.

which can be expressed as  $1.9 \times 10^{18}$  passes before erasure.

### 5.3.3 Shingled Recording

For shingled recording the pole tip width was 80 nm. We also used a taper angle of  $75^\circ$  as shown in Fig. 2.12.

A maximum effective write field of 1.8 T is computed at the target track and 1.4 T at the adjacent track. The field gradient at the target track is 56 mT/nm.

In contrast to centered and staggered writing the shingled recording head is writing

with one of its corners at the trailing edge. Around this corner much larger field gradients arise allowing the recording on densely packed bit cells [55, 120]. Now the possible media anisotropy is not governed by the underlying track width. Here the media anisotropy is chosen equal to the one for the staggered recording head with  $0.49 \text{ MJ/m}^3$ . This translates to a anisotropy field of 1.4 T. Under different applied coil currents this field contour changes in shape, which consequently changes the target track centers. This is outlined in Fig. 5.7.

The most promising shingled head is controlled with 40 mA and its effective field profile shown in Fig. 5.8. The same media material as for the staggered head is used. An anisotropy constant of  $0.49 \text{ MJ/m}^3$  would have a zero field energy barrier of  $115 k_B T$ . The adjacent track energy barrier is  $46.9 k_B T$  which can be expressed as  $1.8 \times 10^{18}$  passes before erasure.



Die approbierte gedruckte Originalversion dieser Dissertation ist an der TU Wien Bibliothek verfügbar.  
The approved original version of this doctoral thesis is available in print at TU Wien Bibliothek.



# Multi-objective optimization of static recording simulation

*Portions of this chapter were previously published in [24] and have been reproduced with the permission of the co-authors. Content which was not generated by the author of this thesis is explicitly denoted.*

## Contents

6.1	Strategy . . . . .	<b>54</b>
6.1.1	Design Evaluation . . . . .	54
6.1.2	Optimization Process . . . . .	54
6.1.3	Error Rate Approximation . . . . .	56
6.2	Geometrical Setup . . . . .	<b>60</b>
6.2.1	Predefined Media Design . . . . .	60
6.2.2	Parametrized Recording Head Design . . . . .	60
6.3	Results . . . . .	<b>62</b>
6.4	Remarks . . . . .	<b>64</b>

In this chapter a first version of an automated pole-tip shape optimization tool chain is presented. The combination of micromagnetic finite element simulations [115] and a multi-objective optimization software [121] is described in Section 6.1. The optimization maximizes the difference of two field values and one field value at specific locations along the targeted track. In order to prevent adjacent bits from getting overwritten an additional constraint keeps the head field below the media switching field at the adjacent track. After optimization we approximate the achieved error rates. Section 6.2 describes the chosen recording media and the recording head’s geometry in detail. Section 6.3 reports on first optimized head structures which are discussed in Section 6.4.

Xia and co-workers investigated the influence of head-shield-, head-media-spacings and track widths on areal density with a 3D finite element head for perpendicular magnetic recording systems [122]. Shute and co-workers performed similar distance property

optimizations by using a two-dimensional analytical Fourier approach computing the magnetic potential between main pole, return pole and soft underlayer [123].

## 6.1 Strategy

The optimization cycle consists of two major parts. First the *optimization process*, which varies several input parameters of a black box system iteratively to minimize or maximize one or more output values of that same system. The second part is located inside this black box. The *model evaluation*, which mostly has to be implemented from scratch, has to read in the given input parameters and return an output value which ideally describes the performance of a given set of input parameters. The optimization algorithm minimizes such an output value by iterating through several combinations of design parameters, ideally in a reasonable amount of model evaluations. In the following two chapters a description of both parts is provided.

### 6.1.1 Design Evaluation

We perform micromagnetic simulations in order to evaluate the write field of different head designs as outlined in Chap. 5. Now the geometry is automatically constructed with a Python script controlled via input values, which are defined in Sec. 7.2. The input values are provided by the optimizer and therefore the optimizer needs the values of the objective function and the associated constraint.

In Fig. 6.1 the perpendicular field contribution  $\mu_0 H_z$  and the effective field  $\mu_0 H_{\text{eff}}$  following the Stoner-Wohlfarth-Model in (5.1) are plotted along the target and adjacent track. The figure highlights the three response quantities used for optimization: (1) the maximum effective field gradient and (2) the effective field at the position of maximum field gradient, both along the target track. And for the constraint (3) the maximum effective field along the adjacent track. These three values are handed over to the optimization software HEEDS<sup>®</sup>, which itself and its functionality is described in the section below.

### 6.1.2 Optimization Process

Within the first approach of optimizing recording head shapes in terms of write performance the commercial software HEEDS<sup>®</sup> by RED CEDAR TECHNOLOGY<sup>®</sup> software is used. It promises an automated design space exploration for single and multi-objective optimizations [92]. The default search method is called SHERPA, which apparently uses multiple search strategies during optimization in the background. SHERPA is the abbreviation of "simultaneous hybrid exploration that is robust, progressive and adaptive". However, it has to be mentioned, that it is kept secret which and how many search strategies are used simultaneously within HEEDS<sup>®</sup>.

In order to compute the best shape of a recording head for a specific media and writing scheme two objectives and one constraint were defined. Fig. 6.1 highlights the return values for the optimization after a design evaluation with red circles.

These three quantities are used for the multi-objective function

$$\max_{\mathbf{y}} f_{\text{obj}}(\mathbf{y}) := (f_1(\mathbf{y}), f_2(\mathbf{y})), \mathbf{y} \in \mathbb{Y}^{k_{\text{in}}} \subseteq \mathbb{R}^{k_{\text{in}}} \quad (6.1)$$

$$\text{subject to } g(\mathbf{y}) < H_{\text{sw}}, \quad (6.2)$$

where  $f_1(\mathbf{y})$  and  $f_2(\mathbf{y})$  are both objective functions and  $g(\mathbf{y})$  the constraint.  $\mathbf{y}$  represents a single set of  $k_{\text{in}}$  design parameters  $(y_1, y_2, \dots, y_{k_{\text{in}}})^\top$ . These design parameters are limited in the design space to a feasible set  $\mathbb{Y}$  shown in Table 6.2 on page 62. However, within those bounds, the design parameters were treated as continuous variables.

The first objective (6.3) is to maximize the effective field gradient  $dH_{\text{eff}}/dx$  along the target track. By maximizing the gradient, head designs with field angles around  $45^\circ$  will be favored. Huge gradients also translate into head field profiles with a large field at the targeted bit and a small field at the previously written bit.

$$f_1(\mathbf{y}) := \left[ \max \left( \frac{dH_{\text{eff}}}{dx} \right) \right]_{\text{targ}} \quad (6.3)$$

In conventional recording on granular media large field gradients produce sharper transitions between bitcells. In contrast, with recording on bit patterned media, large field gradients in both down- and cross-track-direction are favored because they will allow narrow track pitches in both directions. Therefore higher areal densities are possible. Consequently the objective function also implicitly let the optimization favor head designs capable of writing on media with larger areal density. High down-track field gradients are important for island addressability.

The intrinsic material parameters applied for the main pole represent CoFe having an exchange coupling constant  $A_{\text{ex}} = 20.15 \text{ pJ m}^{-1}$ , a saturation polarization  $J_s = 2.4 \text{ T}$  and an anisotropy constant  $K_1 = 800 \text{ J m}^{-3}$ .

But if maximizing the gradient is the only objective function of the optimizer, we won't find the solution for the best head design. Additionally we have to favor recording heads which induce a strong stray field on the target track. Therefore, as second objective function we define

$$f_2(\mathbf{y}) := [H_{\text{eff}}(x_{\text{max}})]_{\text{targ}}, \quad (6.4)$$

where  $x_{\text{max}}$  denotes the down-track position where the effective field gradient  $dH_{\text{eff}}/dx$  has its maximum. This specific position will be called the "working point" of our recording field profile. The higher the achievable writing field, the more thermally stable materials can be chosen for a bit (see thermal stability in Eq. 2.1). We adjust the media anisotropy such that the anisotropy field matches  $H_{\text{eff}}(x_{\text{max}})$ .

With above defined objective functions (6.3 and 6.4) a mechanism is constructed to increase the overall write performance on the target track as outlined in Fig. 6.2. But the bits on neighboring tracks need to be treated with care. Therefore, the following inequality constraint

$$g(\mathbf{y}) := [\max(H_{\text{eff}})]_{\text{adj}} < H_{\text{sw,med}} \approx H_{\text{ani,med}} = 2K_u/J_s =: H_{\text{eff}}(x_{\text{max}}) \quad (6.5)$$

is defined. This will keep the maximum effective field at the adjacent track below the media's switching field  $H_{sw,med}$ , as the optimization software will drop all designs violating that constraint. The small media diameter again allows the assumption of coherent reversal and therefore the media anisotropy field can be defined as the media's switching field  $H_{ani,med} \approx H_{sw,med}$ . Please note that instead of reducing the switching field according to the Stoner-Wohlfarth equation for oblique field angles we increase the write field accordingly. Multiplying the computed write field with the Stoner-Wohlfarth scaling factor (see Fig.5.2) gives the effective write field.

Stray fields from neighboring bits contribute to the switching field distribution, which is taken into account when estimating the bit error rate (see Eq. (6.7)).

Fig. 6.2 summarizes the optimization strategy. Maximizing the field gradient and the write field at point of maximum gradient increases the difference between the effective write field at the target island and the previously written island.

Within this chapter we focus on optimizing the shape of the recording head and its surrounding shield for bit patterned media. Such numerical optimization methods are iterative and require many evaluations of the objective function. Without a search strategy good designs are commonly found by performing a so-called Design of Experiments (DOE). But in DOEs the number of evaluations scales drastically with the number of design space dimensions. In combination with high computational cost it is a very time consuming strategy. Within the scope of the presented work, to reduce the number of finite element micromagnetic field evaluations, a response surface method that locally approximates the objective functions within the design space is applied [121]. The benefit of this method is, that you are able to apply a gradient descent method to search for better designs.

Of course, a gradient descent method does not guarantee, that it will end up in the global minimum. Often the method might be trapped in a local minimum. It is a critical task for the optimization software to initially fill the space with evenly and well distributed training points.

We performed optimizations for three different writing schemes. The script optimized a recording head shape for a specific but fixed underlying media layout. After several design evaluations the design with the maximum field gradient and effective field is used to compute the error rates described in Section 6.1.3. Optimizations were performed for a single-phase bit patterned media island of cylindrical shape.

### 6.1.3 Error Rate Approximation

In general we have to differentiate the following three error occurrences during a writing process on bit patterned media:

1. accidentally not writing the currently targeted bit
2. accidentally overwriting the previously written bit while writing the targeted bit
3. accidentally overwriting bits in neighboring adjacent tracks

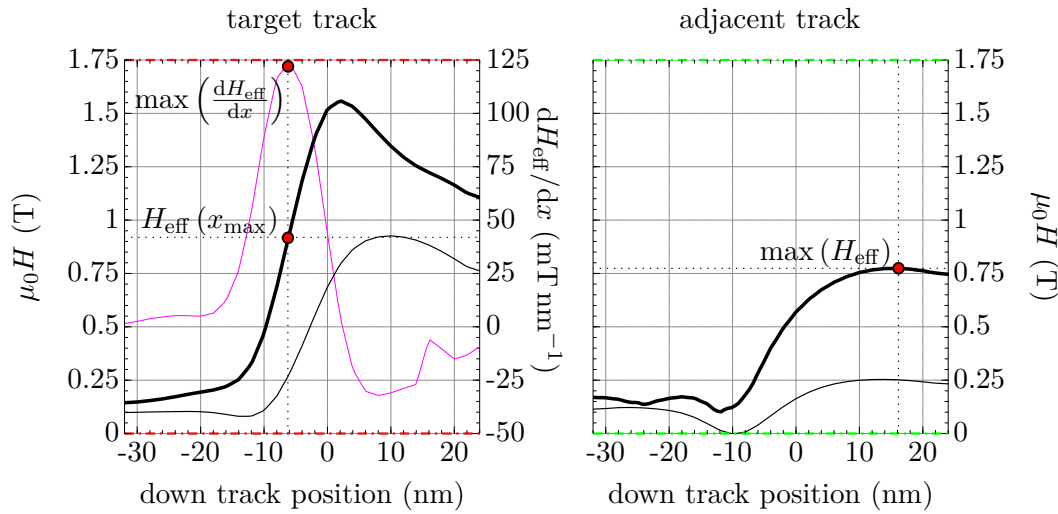


Figure 6.1: The effective field (bold) plotted along the center of the target (left) and adjacent track (right). For comparison  $\mu_0 H_z$  shown in thin black and the effective field gradient in pink. Highlighted with red dots, both objective function values at the target track: (i) maximum effective field gradient and (ii) effective field at  $x_{max}$ . The optimization constraint (iii) maximum effective field at the adjacent track is shown on the right hand side. Note that the red and green dash dotted lines highlight the locations of the target and adjacent track shown before in Fig. 5.1.

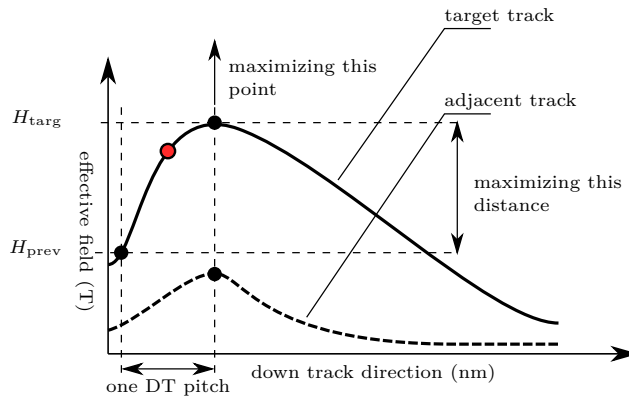


Figure 6.2: Schematic of multi-objective function optimization. Maximizing the effective field and its down-track gradient will maximize the difference between  $H_{prev}$  and  $H_{targ}$ . The solid and dashed lines indicate the effective field along the target track and the adjacent track respectively. The distance between  $H_{prev}$  and  $H_{targ}$  is one down-track pitch. The red dot highlights the point of maximum effective field gradient.

Mallary and co-workers pointed out that the goal of 1 Td/in<sup>2</sup> in perpendicular recording is feasible as long as a long term error of 0.01% is not exceeded [117]. They also emphasize that every aspect of the recording system must be optimal to achieve such error rates.

How these three error are treated is explained in the following three sections:

### Not Writing the Target Bit

If the effective writing field acting on the target bit lies below the bit's switching field ( $\mu_0 H_{sw,med} \approx \mu_0 H_{ani,med} \approx 2K_u/J_s$ ) we assume that the bit has not been written successfully. In this study we define  $\mu_0 H_{eff}(x_{max})$ , the effective field value at our working point  $x_{max}$ , to be the media's switching field. More accurately  $\mu_0 H_{eff} := 2K_1/J_s$  where  $J_s$  is fixed to  $J_s = 0.724$  T and  $K_1$  is calculated with this relation. As previously proposed in [124, 125], the error rate for not writing the targeted bit  $BER_{targ}$  can be approximated with the statistical approach

$$BER_{targ} = \frac{1}{2} \left[ 1 - \operatorname{erf} \left( \frac{H_{targ} - H_{ani}}{\sqrt{2\sigma_{sw}^2}} \right) \right]. \quad (6.6)$$

$H_{targ}$  is the effective field half a down-track pitch along head flight direction. In Fig. 6.3 the working point and the assumed target and previous bit position is illustrated. In the denominator of (6.6)  $\sigma_{sw}$  represents the switching field distribution

$$\sigma_{sw} = \sqrt{\sigma_{H,pos}^2 + \sigma_H^2 + \sigma_K^2}, \quad (6.7)$$

where  $\sigma_H$  gives the interaction field distribution,  $\sigma_K$  the deviations in anisotropy field of each bit due to fabrication tolerances. The misalignment or synchronization error for writing on bit patterned media is given by

$$\sigma_{H,pos} = \sigma_{pos} \frac{dH_{eff}}{dx}, \quad (6.8)$$

where  $\sigma_{pos}$  reflects the head positioning jitter above a bit. The deviations have been extracted from Schabes and co-workers [126]:  $\sigma_H = 0.02$  T,  $\sigma_{pos} = 0.8$  nm,  $\sigma_K = 0.05$  T.

### Accidentally Re-Writing the Previously Written Bit

An insufficiently large field gradient might re-write previously written bits, because the effective field is still large enough to overcome the media's switching field. Analogue to Equation 6.6 the following statistical relation can be drawn for this error occurrence.

$$BER_{prev} = \frac{1}{2} \left[ 1 - \operatorname{erf} \left( \frac{H_{prev} - H_{ani}}{\sqrt{2\sigma_{sw}^2}} \right) \right], \quad (6.9)$$

where  $H_{prev}$  is the effective field extracted half a down-track pitch before the recording head's working point (see Fig. 6.3).

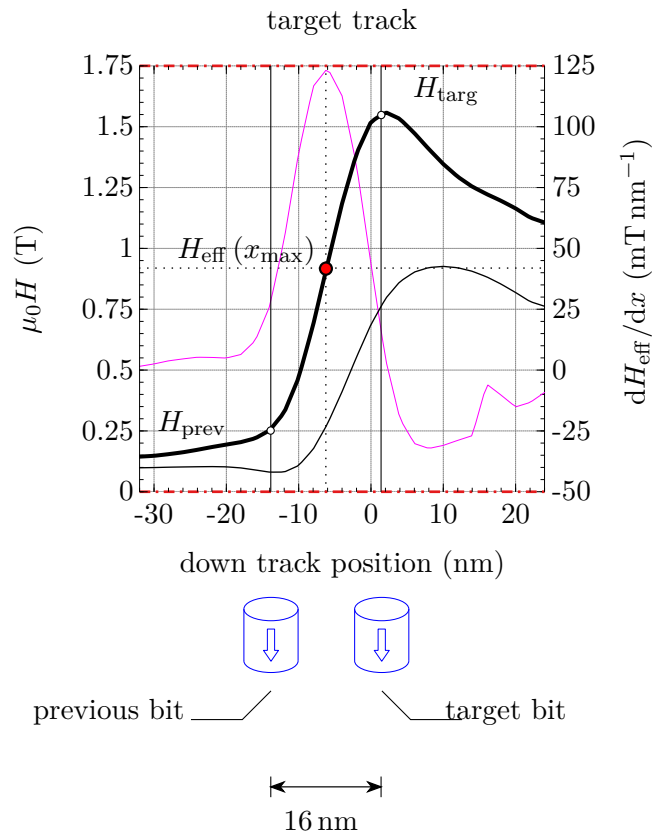


Figure 6.3: Perpendicular head field profile (black) along the target track in down-track direction. The field gradient in down-track direction is colored pink. The media's anisotropy field  $H_{\text{ani,med}}$  is extracted from this recording field profile. It is chosen to be the effective field at the point of highest field gradient of the profile. The field values for the statistical error rate calculation approach  $H_{\text{targ}}$  and  $H_{\text{prev}}$  are each extracted half a down-track pitch in and opposing head flight direction respectively.

## Accidentally Overwriting the Adjacent Track

The constraint defined in (6.5) filters out all recording head designs where the adjacent track field is larger than the media’s anisotropy field. From the perspective of a bit located on an adjacent track it is not sufficient to withstand the fringing field of one single recording head passing. Instead it has to keep its information after multiple passes of this recording head.

Therefore, in this third error scenario we approximate the thermally induced track erasure [127] by placing a single bit at the position where the fringing field reaches its maximum and compute its energy barrier  $E_B$  with the Nudged-Elastic band method. With the Arrhenius Power Law we can estimate the average life time of the bit’s magnetization at a certain temperature

$$\tau = \frac{1}{f_0} \exp\left(\frac{E_B}{k_B T}\right). \quad (6.10)$$

The prefactor  $f_0^{-1}$  is the inverse of the attempt frequency [127] assumed to be  $f_0 = 1.3 \times 10^{11}$  Hz. Temperature  $T$  is set to room temperature and  $k_B$  is the Boltzmann constant. Eq. 6.10 estimates the lifetime of a bit before spontaneously overcoming an energy barrier  $E_B$ . By assuming a field exposure time of  $t_{\text{write}} = 1$  ns, we get the number of passes before erasure with  $\tau/t_{\text{write}}$  and the corresponding error rate as

$$\text{BER}_{\text{adj}} = \frac{t_{\text{write}}}{\tau}. \quad (6.11)$$

## 6.2 Geometrical Setup

In the previous section 6.1, we explained how we will optimize our recording head designs and how we categorize and evaluate them. Now a detailed description of how we model the media and recording head follows. All geometries are constructed with the help of a parametrized Python script.

### 6.2.1 Predefined Media Design

While the pole tip shape and the shield distance vary, a predefined bit patterned media layout is used as shown in Fig. 6.4. Single phase cylindrical dots with a diameter of 12 nm were used in this media layout. The media was designed to be 10 nm thick. By separating each bit by 19 nm in cross-track direction (cross-track pitch) and 16 nm in down-track direction (down-track pitch) we get a media layout with an areal density of 2.12 Td/in<sup>2</sup> and a filling factor of 30 %. The distance between the recording head’s air bearing surface and the media surface is 8 nm.

### 6.2.2 Parametrized Recording Head Design

The write head uses a helical coil with 4 turns. In Fig. 6.5 the full finite element model is illustrated. The coil carries a current of 80 mA and induces a magnetic field



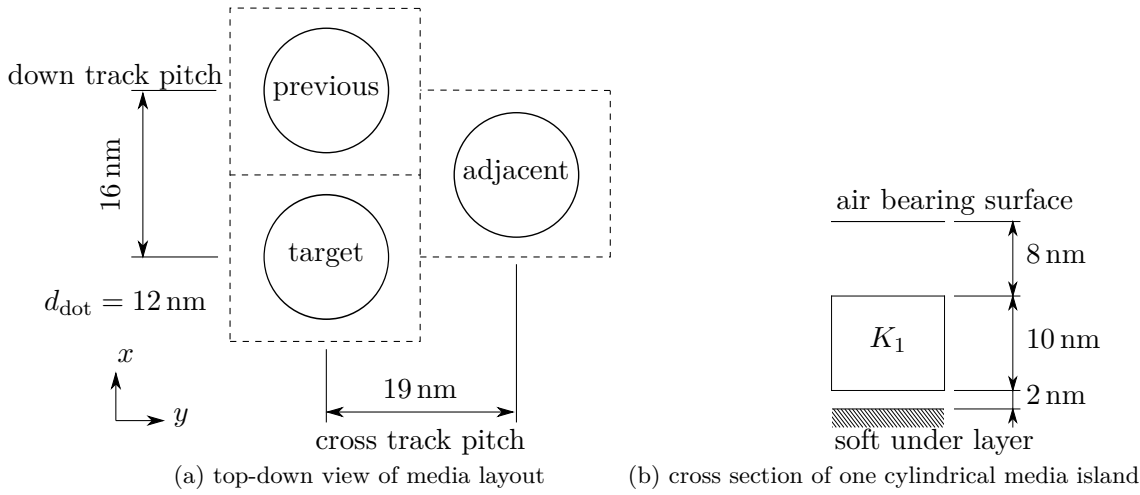


Figure 6.4: Media layout (a) top-down view and (b) cross section of 2 Td/in<sup>2</sup> single phase media with a dot diameter of  $d_{\text{dot}} = 12$  nm. The islands on the medium are distributed in a triangular pattern with a 19 nm cross-track pitch and 16 nm down-track pitch.

in the main pole and yoke of the write head. For the main pole we use a magnetic saturation magnetization of 2.4 T and an exchange constant of 20.15 pJ m<sup>-1</sup>. These intrinsic properties were chosen to reflect a CoFe main pole [63, p. 450]. The applied intrinsic material properties of the main pole and all other parts are summarized in Table 6.1.

part	material	$\mu_0 M_s$ (T)	$A_{\text{ex}}$ (pJ m <sup>-1</sup> )	$K_1$ (J m <sup>-3</sup> )
main pole	CoFe	2.4	20.15	800
yoke	Ni <sub>45</sub> Fe <sub>55</sub>	2	13.5	0
return pole	Ni <sub>45</sub> Fe <sub>55</sub>	2	13	0
shield	NiFe	2	13	0
soft underlayer	Ni <sub>45</sub> Fe <sub>55</sub>	1	13	0

Table 6.1: The applied intrinsic material properties of the recording head model.

Return pole, yoke and soft underlayer possess the similar intrinsic material properties as the main pole itself, but without magnetocrystalline anisotropy. Those parts are soft magnetic. Where the main pole has a favoring magnetization axis in  $y$  or cross-track direction and a magnetocrystalline anisotropy constant  $K_1 = 800$  J m<sup>-3</sup>. This helps to bring the write pole into a well defined magnetic state if the write current is zero.

The write head geometry is constructed with the CAD software Salome [112] and meshed with Netgen [113]. The air bearing surface is discretized with a mesh size of 2.5 nm near the pole tip and coarsens with increasing distance. In Fig. 6.6 all relevant parameters are shown, whereas the parameter space restrictions are summed up in Table 6.2. While we optimized both shield gaps and edge angles for all three writing schemes we made

some exceptions for shingled recording heads regarding their pole tip width. For shingled writing the pole tip width can be much larger because no centered track needs to be addressed. The width of the shingled recording head tip is kept constant at 80 nm and additionally the cross-track position is optimized, as it was not clear where to put the write corner. This is only necessary for this one writing scheme, because the other two have the recording heads centered above one or two target tracks.

parameter	unit	lower bound	upper bound
trailing shield gap	nm	5	20
trailing edge angle	°	0	45
side shield gap	nm	5	20
side edge angle	°	0	45
pole tip width <sup>1</sup>	nm	10	30
cross-track offset <sup>2</sup>	nm	-10	10

Table 6.2: The search range for each geometrical parameters. All parameters are in the same optimization loop.

### 6.3 Results

The free parameters listed in Table 6.2 have been optimized for minimum bit error rates. For each recording scheme, we reached a stopping condition after 140 design evaluations. About 30 percent of the evaluations violated constraints defined in (6.5) and have been discarded. For each recording scheme, the optimized parameters along with their bit error rates are summarized in Table 6.3.

Note that the optimization maximized the objective function defined in Section 6.1.2 and the error rate calculations have been performed afterwards as described in Section 6.1.3.

The thermally induced adjacent track erasure  $BER_{adj}$  is clearly dominating for these optimized recording head designs. By shifting the working point within the field profile, as pointed out in Section 6.1, we are able to use media materials with a larger anisotropy field. We simple re-evaluated the write error for the optimized head design for a larger media anisotropy. This increases the thermal stability of the recording media leading to a reduced adjacent track erasure, but makes it harder to write the bits in the target track. The shingled recording head design clearly outperforms the two other investigated writing scheme heads. A shingled recording head has a significantly larger air bearing surface capable of emitting way more stray field towards the media allowing thermally more stable bits. The shingled recording head has a tapered pole tip shape which translates into lower adjacent error rates compared to rectangular shaped air bearing surfaces. The optimized pole tip widths were 14 nm, 29 nm and fixed 80 nm, for centered, staggered

<sup>1</sup>For shingled recording the pole tip width was fixed at 80 nm

<sup>2</sup>Optimized only for shingled recording and is kept 0 nm for centred and staggered writing

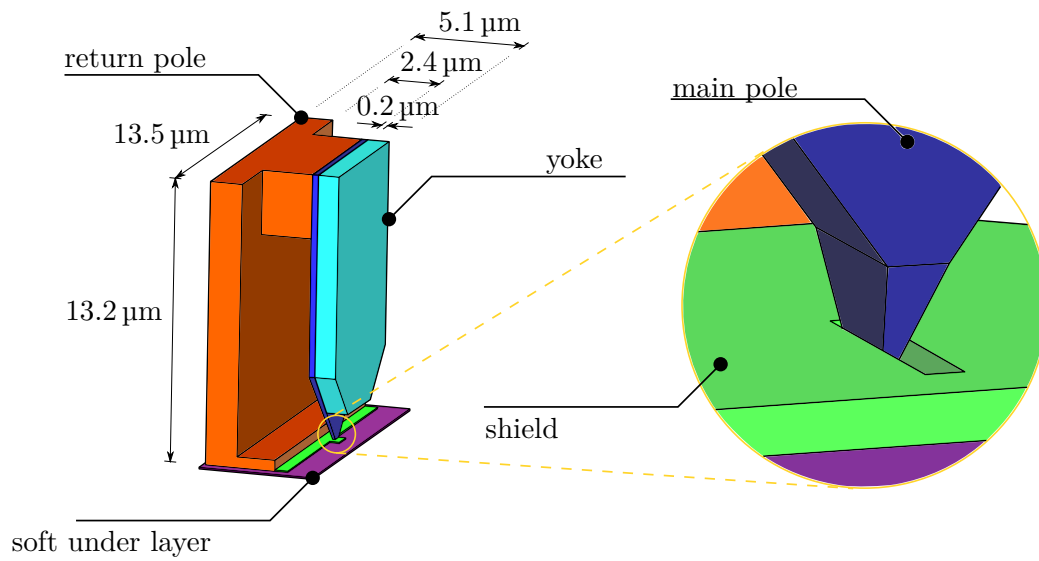


Figure 6.5: Geometry dimensions of the recording head, soft underlayer, wrap-around shield and return poles. The soft underlayer has a thickness of 60 nm. The distance between the air bearing surface and soft under layer is 20 nm as shown in Fig. 6.4b. Material properties of each part are summarized in Table 6.1

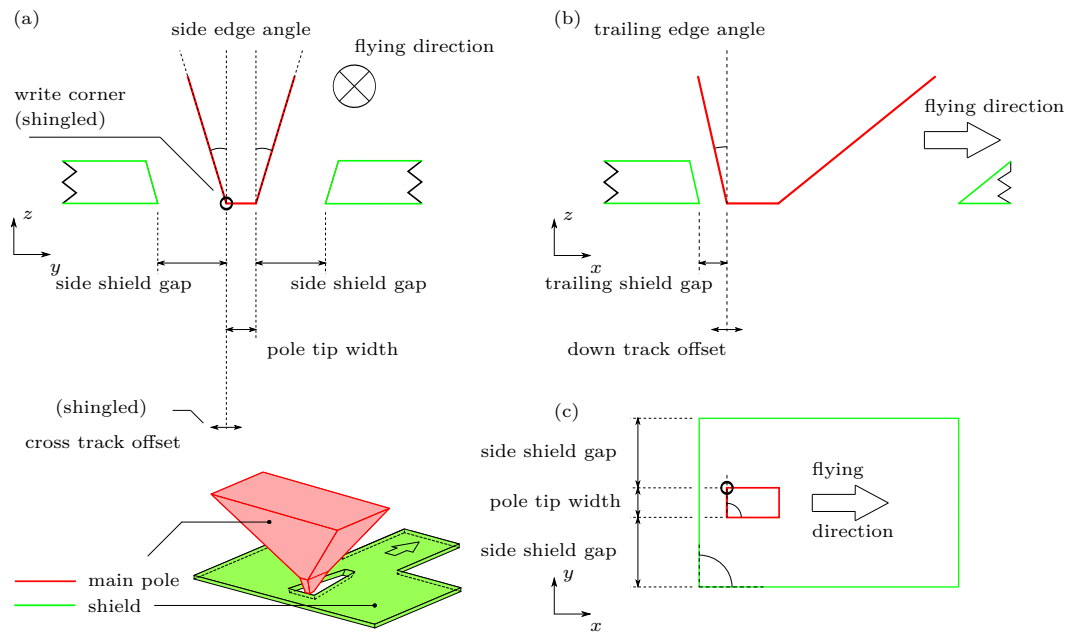


Figure 6.6: Main pole (red), wrap around shield (green) and their free parameters. (a) Down-track view of pole tip and shield with the writing scheme dependent cross-track offset, (b) Cross-track view and (c) Top view. The pole tip taper angle is always kept  $90^\circ$  except for shingled recording it is  $75^\circ$ . In the lower right sub-figure the taper angle is highlighted as right angle sign.

$BER_{\text{targ}}$	$BER_{\text{prev}}$	$BER_{\text{adj}}$	$\mu_0 H_{\text{ani}}$ (T)	trailing shield gap (nm)	trailing edge angle ( $^\circ$ )	side shield gap (nm)	side edge angle ( $^\circ$ )	pole tip width (nm)
<b>centered writing</b> $\square$								
$5.1 \times 10^{-5}$	$1.3 \times 10^{-5}$	$> 1$	0.75	9	20	16	15	14
$1.9 \times 10^{-2}$	$9.4 \times 10^{-7}$	$5.5 \times 10^{-1}$	0.90	9	20	16	15	14
<b>staggered writing</b> $\square$								
$1.3 \times 10^{-6}$	$4.7 \times 10^{-6}$	$> 1$	0.82	13	35	11	10	29
$2.9 \times 10^{-2}$	$7.2 \times 10^{-8}$	$5.2 \times 10^{-2}$	1.07	13	35	11	10	29
<b>shingled writing</b> $\nabla$								
$1.2 \times 10^{-5}$	$1.1 \times 10^{-5}$	$5.5 \times 10^{-6}$	1.00	14	45	12	5	80
$1.4 \times 10^{-4}$	$2.3 \times 10^{-6}$	$2.7 \times 10^{-8}$	1.10	14	45	12	5	80

Table 6.3: Bit error rates and parameters for best designs for each writing scheme. For each optimized writer design we picked two working points, which determines the media anisotropy field  $H_{\text{ani}}$ : one at the point of maximum field gradient and one at higher media anisotropy field. This results in better error rates throughout all writing schemes. All values are rounded to two significant digits. Writing schemes marked with  $\square$  and  $\nabla$  have been designed with a pole tip taper angle of  $90^\circ$  and  $75^\circ$  respectively.

and the shingled recording head, respectively. In Fig. 6.7 we can observe the effective write fields along the target tracks for the three different writing schemes. The largest difference between the write field on the target track and on the filed at the adjacent track occurs for shingled writing. The field gradients throughout all writing schemes are within a range of  $30 \text{ mT nm}^{-1}$  to  $40 \text{ mT nm}^{-1}$ .

Additionally we observe that a pole tip width of 14 nm for centered recording is slightly above one bit diameter of 12 nm. As for staggered recording the opposite is observed, as the optimized pole tip width is 29 nm, which is slightly below two bit diameters plus their distance in cross-track direction. This underlines the importance of the pole tip width according to the underlying media layout as we want to keep as less write field as possible in the adjacent tracks.

## 6.4 Remarks

A fully-automated pole-tip shape optimization tool has been developed. It involves the construction of a write head with the open source computer-aided design software SALOME [112]. This is all done within a single Python script constructing a parametrized recording head geometry and performing multiple simulations to finally compute error rates. Optimization was done with the framework HEEDS<sup>®</sup> using a multi-objective

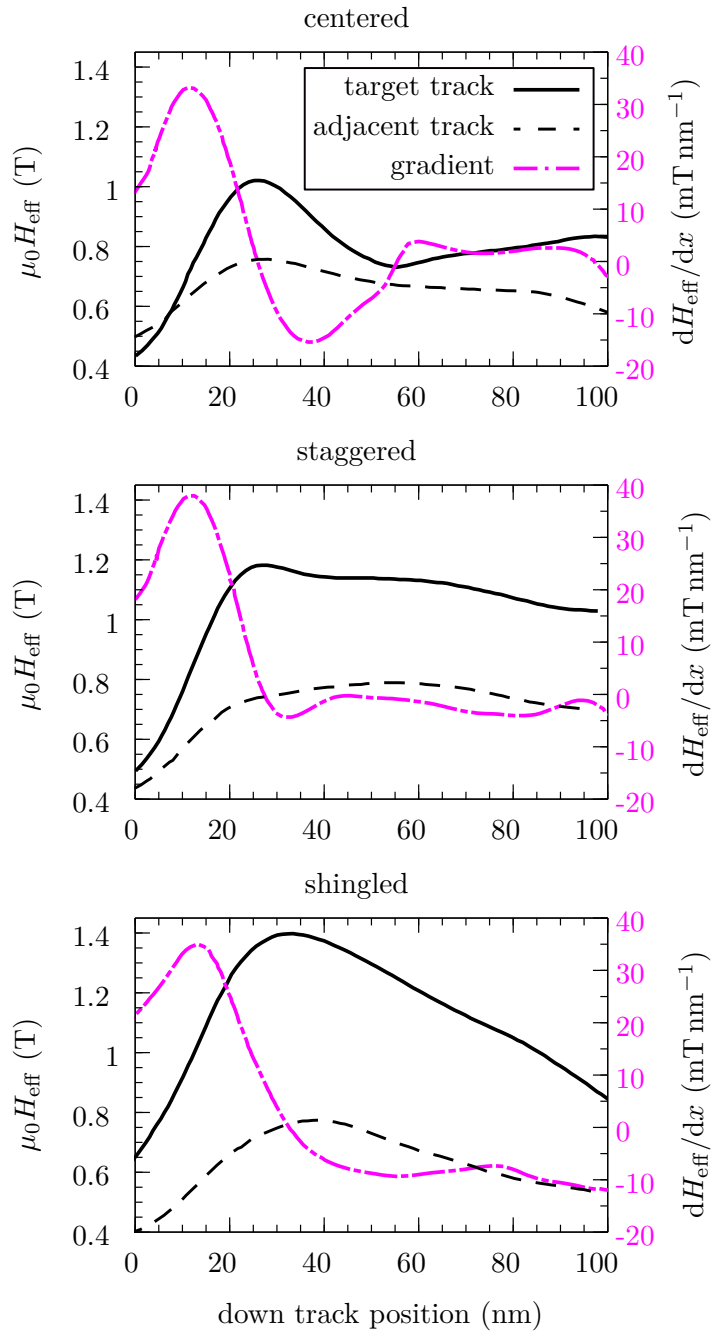


Figure 6.7: Effective field profiles of each writing scheme's best recording head design. The solid and dashed lines show target track and adjacent track field profiles respectively. The target track's effective field gradient is depicted as a dot-dashed line.

optimization algorithm called SHERPA. The script constructs a write head geometry described by 5 free design parameters: trailing shield gap, trailing edge angle, side shield gap, side edge angle and pole tip width. These parameters were optimized so that the effective field and its gradient is maximized in order to minimize the bit error rate during recording. We varied and optimized the recording head shapes for three different writing schemes: centered, staggered and shingled recording. A more detailed description of those schemes can be found Section 2.3.2. It was assumed that the working point of a recording head's flux, shown in Fig. 6.3, should be at the point with highest field gradient and the best recording performance is achieved if the point of highest field gradient is located near the maximum field point as well. Our simulations show that taking into account the write error rate it is beneficial to move the working point towards higher write fields.

As assumed by Albrecht et.al [57] a write error rate below  $10^{-2}$  is tolerable and potential loss of data can be recovered with the help of error correction codes. This error rate is achieved only for the shingled writing scheme. Shingled recording clearly outperforms the other two writing schemes, which is explained through a much larger achievable flux caused by allowing larger head dimensions and tapering. First results show that the adjacent track error is the most critical error rate throughout all optimized writing schemes. Adjusting the anisotropy field of the investigated media allows tuning the adjacent track error while decreasing write-ability on the targeted track.

Looking at the optimized shingled recording head a ten percent increase in the media anisotropy field leads to a one to two order reduction of  $BER_{adj}$  and  $BER_{prev}$ , while  $BER_{targ}$  is increased by an order of magnitude.

Higher areal densities not only require a high local field gradient, but also a very fast magnetic switching of the pole tip to ensure an acceptable write speed. It is assumed that this recording system is capable of switching sufficiently fast for the underlying media layout and writing scheme. Only the head's final produced stray field is taken into account for the error rate approximations.

To evaluate the field in the middle of the track, and therefore in the middle of the bit only is too optimistic, because in other areas of a media island a magnetic field larger than the medias switching field might prevail as illustrated in Fig. 6.8. This means that at one side, designs which would be capable of switching the targeted bit have been dropped while on the other side designs which would overwrite the adjacent bit have been kept as a feasible design. A more elaborate treatment of the currently acting field on a media island has to be developed considering not a single field value but the full field acting on the media dot.

The above mentioned issues are addressed in Chap. 7 where both the 3-dimensional distribution of the write field and its change in time are taken into account. Simulating the recording process also considers the dynamic switching process of the individual islands.

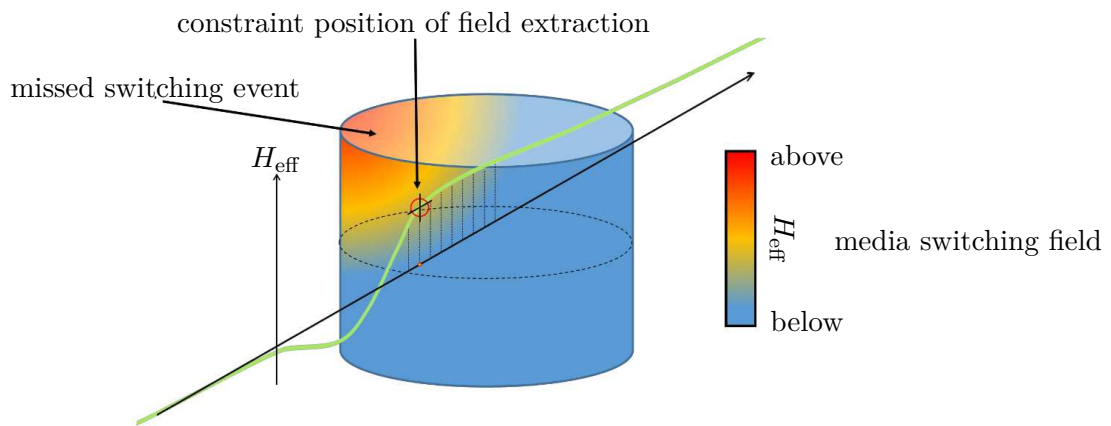


Figure 6.8: The effective write field is strongly non-uniform within the target bit and the bits of the adjacent track. The definition of the objective function treats this scenario as not capable of writing the bit because the region of evaluation is chosen too pessimistic. Vice-versa this treatment would lead to a too optimistic decision regarding the field evaluation within the adjacent track. Designs which are actually capable of switching the target bit were dropped while designs capable of switching the previous or adjacent bits have been considered as viable. Here the field distribution in an island of the adjacent track is shown.



Die approbierte gedruckte Originalversion dieser Dissertation ist an der TU Wien Bibliothek verfügbar.  
The approved original version of this doctoral thesis is available in print at TU Wien Bibliothek.



# Single objective optimization of dynamic recording simulation

*Portions of this Chapter were previously published in [25] and have been reproduced with the permission of the co-authors. Content which was not generated by the author of this thesis is explicitly denoted.*

## Contents

---

7.1	Strategy . . . . .	<b>70</b>
	7.1.1 Design Evaluation . . . . .	70
	7.1.2 Optimization Process . . . . .	71
	7.1.3 Comprehensive Objective Function . . . . .	72
	7.1.4 Improved Error Rate Approximation . . . . .	72
7.2	Geometrical Setup . . . . .	<b>75</b>
	7.2.1 Exchange Coupled Composite Media Design and Layout . . .	75
	7.2.2 Parametrized Recording Head Design . . . . .	76
7.3	Results . . . . .	<b>78</b>
7.4	Remarks . . . . .	<b>80</b>

---

In Chapter 6 the recording process has been described statically. The effective field below the pole tip’s air bearing surface has been computed and extracted at two specific locations in order to evaluate the error rates. By fine-tuning the media’s intrinsic properties the error rates could be improved. Within the following Chapter a more elaborate approach is presented. Media properties are now optimized together with the recording head geometry. The media type has changed from single phase to exchange coupled composites (ECC) with a doubling areal density media layout (see Section 7.2.1). In order to compute the contributions to the total error rate multiple finite element micromagnetic recording simulations are performed considering the complete head field felt by each targeted, previous or adjacent bit.

## 7.1 Strategy

M. Schabes analyzed how bit patterned media fabrication tolerances translate into areal density restrictions and field gradient requirements at a fixed write error rate [126]. He emphasized that the "field distributions, fabrication tolerances, write-synchronization tolerances, as well as the field gradient have to be well controlled in a balanced bit patterned system." Kanai and coworkers investigated the influence of shields surrounding a single pole recording head tip [128]. They computed the magnetic recording head field with a finite element micromagnetic solver and simulated the recording process onto many different Voronoi tessellated granular media with areal densities around 400 Gb/in<sup>2</sup>. They co-optimized features of the head and the media together. In their work they emphasized the importance of trailing shields and that a head structure can be found through numerical optimization, in order to record on such presented media layouts. Fukuda and co-workers presented a method simultaneously optimizing writer and granular media parameters for perpendicular recording, using a genetic algorithm together with a finite element static Maxwell solver and a micromagnetic solver [129]. Li et al. utilized a second order response surface method in order to co-optimize bit patterned media and write head properties maximizing the effective writing field gradient for shingled magnetic recording [130]. They showed that the reduction of trailing shield gap increases the effective field gradient and that the media's coercivity influences the geometrical requirements of the shields.

The head-media spacing is one of the most important parameters, as higher fields at the media allow the use of more thermally stable materials. In order to achieve lower error rates reduced the magnetic spacing to 6 nm.

In the following Sections we document how the optimization strategy has been improved relative to the method presented in Chapter 6. Section 7.1.2 introduces a newly implemented optimization software, Section 7.1.3 the definition of a new objective function, and Section 7.1.4 an improved version of the error rate calculation.

### 7.1.1 Design Evaluation

In the following Fig. 7.1 a flow chart of a single design evaluation is presented. In contrast to the previous evaluation from Chapter 6, the computation of the head field is the first of multiple steps of acquiring the sum of all writing error rates. The computed 3D head field profile is afterwards used for dynamic recording simulations. Each target and previous bit error computation consists of 12 parallelly executed writing simulations which will be described in Section 7.1.4. Those will lead to a more comprehensive investigation of the media switching field distribution. Through joint optimization of head and media properties the error rates are reduced as compared to those presented in Chapter 6.

To prevent wasting computational resources for useless head designs the error rate contributions are computed in a sequentially manner beginning with the target-, then the previous- and at last the adjacent track error. If the head design fails to write the target bit, an early stopping criteria is met, in which all further simulations will be aborted.

This criterion will also be met if the previously written bit is overwritten. The dashed boxes in Fig. 7.1 indicate this stopping criteria.

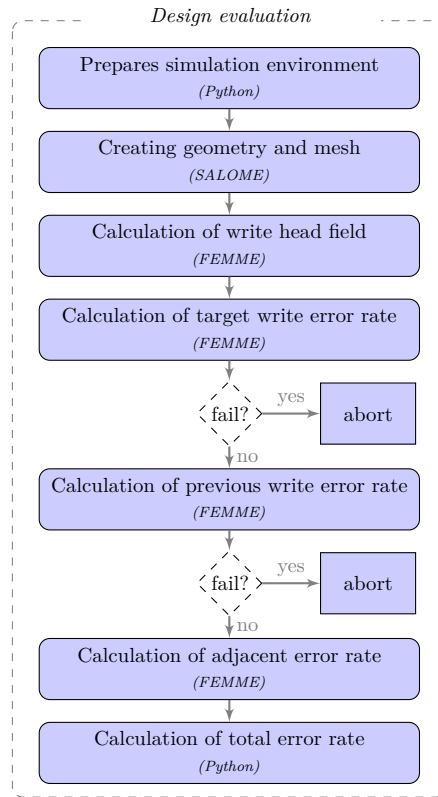


Figure 7.1: The flow chart of a single model evaluation which returns the sum of all error rates after sequentially evaluating the write error rate of the targeted bit, the error rate of accidentally writing the previously written bit and the error rate of accidentally writing a bit located at an adjacent track. The design evaluation is handled by a Python script which calls different other software packages noted in the rounded brackets below each task description.

### 7.1.2 Optimization Process

In this Chapter we switched to the open source software toolkit Dakota (**D**esign **A**nalysis **K**it for **O**ptimization and **T**erascale **A**pplications)[91] for optimization. Within this toolbox many different optimization algorithms are implemented and can be easily used and adapted within a command shell. One promising algorithm which suits the problem at hand is called *efficient global optimization* (EGO) [85, 86]. In EGO the design space is described with a Gaussian Process and promises a good trade-off between design space exploration and exploitation [85]. A more detailed description of EGO and its expected improvement function (EIF) can be found in Section 3.1.

### 7.1.3 Comprehensive Objective Function

The definition of the objective function has been reconsidered as we are now performing recording simulations within the optimization cycle. This opens the opportunity to include the error rates into the objective function itself. The new single objective is defined to minimize the total bit error rate, which is the sum of all three error rates.

$$\min_{\mathbf{y}} f_{\text{obj}}(\mathbf{y}) := \text{BER}_{\text{tot}}(\mathbf{y}), \mathbf{y} \in Y^{k_{\text{in}}} \subseteq \mathbb{R}^{k_{\text{in}}} \quad (7.1)$$

where  $\mathbf{y}$  represents a single set of  $k_{\text{in}}$  design parameters  $\{y_1, y_2, \dots, y_{k_{\text{in}}}\}$  explained in more detail in Section 7.2.  $\text{BER}_{\text{tot}}$  is the total bit error rate used as response value calculated by

$$\text{BER}_{\text{tot}} = \text{BER}_{\text{targ}} + \text{BER}_{\text{prev}} + \text{BER}_{\text{adj}}. \quad (7.2)$$

The simulations for each kind of error rate are computationally expensive, hence they are calculated sequentially to be able to omit the remaining *design evaluation* as soon as one error rate doesn't meet the requirement. For example if the current evaluated write head design can't reverse the target bit with its write field, there is no reason to compute the other error rates. Similarly, if the head design has a low target bit error rate but always re-writes the previous bit, the computation of the adjacent error rate is obsolete.

### 7.1.4 Improved Error Rate Approximation

The error rate calculation for the target and the previous bit error rate has been updated. Previously we computed the error based on the static write field and the media switching field neglecting the 3-dimensional distribution of the write field and magnetization dynamics. In Fig. 6.8 the flaws of the error rate estimation presented in Chapter 6 are highlighted.

Now we derive the write error from multiple simultaneous dynamic recording simulations. As done in Section 6.1.3 we still apply the statistical relation presented in [124, 126, 131] to estimate the error rates.

An alternative method was applied by Kalezhi and Miles [68], where they used an analytical model to compute the energy barrier for write errors of a two-layer exchange coupled composite bit patterned media island. They replaced the magnetization of both the hard and soft layer with a single spin. The method fits well with micromagnetic simulations performed by Greaves et al. [55]. These methods treat the externally applied writing field constant over the entire magnetic body and static over time. In this work we use a similar approach but consider the full field distribution acting on a single media island and dynamically move the head field along the targeted track.

## Target and Previous Bit Error

Until now the error rate

$$\text{BER}_{\text{targ}} = \frac{1}{2} \left[ 1 - \text{erf} \left( \frac{H_{\text{targ}} - H_{\text{ani}}}{\sqrt{2\sigma_{\text{sw}}^2}} \right) \right]$$

takes the difference between the effective field at the target bit  $H_{\text{targ}}$  and the theoretical switching field of that same bit. The theoretical switching field of the bit is assumed to be its anisotropy field  $H_{\text{ani}} = 2K_1/J_s$ . Now two reasons do not allow that simple field difference anymore: (i) the recording head field is not treated homogeneously anymore and (ii) the anisotropy field as media switching field holds as a rough estimate for single phase media only but not for bits with two different phases.

This field difference can be rethought as an interference field  $H_{\text{interf}}$  interfering with the head field  $H_{\text{head}}$ . By knowing how strong that opposing  $H_{\text{interf}}$  can be until the  $H_{\text{head}}$  is not sufficient to switch the bit anymore will give us insight about the target bit error rate  $\text{BER}_{\text{targ}}$ . By knowing how strong an amplifying  $H_{\text{interf}}$  can be until the head field unintentionally switches the previous bit as well, will give us the  $\text{BER}_{\text{prev}}$ . The error rate equations are rewritten to

$$\text{BER}_{\text{targ}} = \frac{1}{2} \left[ 1 - \text{erf} \left( \frac{H_{\text{crit,targ}}}{\sqrt{2\sigma_{\text{sw}}^2}} \right) \right] \quad \text{and} \quad (7.3)$$

$$\text{BER}_{\text{prev}} = \frac{1}{2} \left[ 1 - \text{erf} \left( \frac{H_{\text{crit,prev}}}{\sqrt{2\sigma_{\text{sw}}^2}} \right) \right], \quad (7.4)$$

where  $H_{\text{crit,targ}}$  and  $H_{\text{crit,prev}}$  are the opposing critical field hindering the applied head field from switching the target bit and the critical amplifying field causing an unintentional switching event in the previously written bit, respectively.

To find those critical opposing or amplifying fields, several field values have to be sampled with the help of micromagnetic simulations. During a single micromagnetic simulation the previously computed write head field is locally applied. The 3-dimensional field profile is shifted with previously defined down-track and cross-track offsets accordingly. During writing the field is scaled with the wave form of the write current. The current rise time was 0.1 ns. In addition an external homogeneous field  $H_{\text{interf}}$  is globally applied, acting as the described interference field. The interference field acts as a counter force to the write head field. Fig. 7.2 illustrates the initial simulation setup to find the critical fields for both error rates,  $\text{BER}_{\text{targ}}$  and  $\text{BER}_{\text{prev}}$ .

Those critical fields will be searched along an assumed switching field distribution which is a rough estimate. The bit islands have a switching field distribution which is modeled by a Gaussian distribution. Its standard deviation is proportional to the anisotropy field of the hardest phase of the multiphase media island  $\sigma_{\text{sw,est}} = 0.015 H_{\text{ani}}$  where  $H_{\text{ani}} = 2K_{1,\text{hard}}/J_s$ . Along this initial estimated field distribution, not to be confused with the switching field distribution considering position jitter and fabrication tolerances, we perform micromagnetic recording simulations. For recording simulations, twelve evenly distributed interference field magnitudes  $H_{\text{interf}}$  were picked in the interval

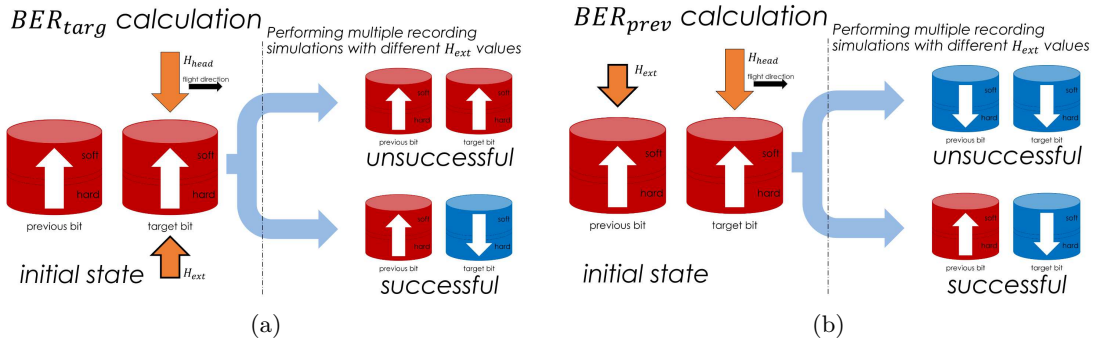


Figure 7.2: The initial state of each recording simulation search for the critical interfering field causing either an unsuccessful or successful write attempt. (a) illustrates the scenarios for the target error and (b) for the previous error rate acquisition.

of 0 to  $4\sigma_{sw,est}$ . These simulations can be done in parallel. Each of 12 CPUs perform a recording simulation where only the interference field varies (see Fig. 7.3). The additionally applied disturbance field is anti-parallel or parallel aligned to the head field for calculating the target bit or previous bit error rate, respectively.

After determining the maximal allowed disturbing fields  $H_{crit,targ}$  and  $H_{crit,prev}$  we are able to obtain both bit error rates by integrating over the tail of the Gaussian function with the critical fields as lower bound [124], as equations (7.3) and (7.4) show.

The part of the evaluation script, which searches for the critical field  $H_{crit}$  is able to refine the search range multiple times. In this work the search has been refined twice with an initial search discretization of half the estimated switching field distribution  $\sigma_{sw,est}$ , which is indicated by long and short tic marks on the  $H_{interf}$ -Axis in Fig. 7.3 as first and second refinement step, respectively. For these recording simulations the write field moves with  $13.5 \text{ m s}^{-1}$  in down-track direction. This results in a writing time of one nano second per bit.

### Adjacent Bit Error

In order to calculate the thermally induced adjacent track erasure error  $BER_{adj}$ , a single bit is placed into the fringing field of the head. The placement of the adjacent bit for each writing scheme can be seen in Fig. 7.7. At this position the field is mapped onto the bit and assumed to be the worst case field exposure for an adjacent bit. Using the nudged elastic band method [106], we compute the energy barrier  $E_B$  for magnetic reversal of the adjacent bit under the influence of the fringing field. The energy path is discretized into 40 images (see Section 4.5) and has been computed with a relative and absolute tolerance of  $1 \times 10^{-8}$ . It is assumed that the highest field exposure and the lowest barrier occurs at the down-track location where the pole tip has its maximum width shifted 2 nm in flight direction. From the energy barrier we calculate the life time of the bit  $\tau = f_0^{-1} \exp(E_B/k_B T)$  with an attempt frequency of  $f_0 = 130 \text{ GHz}$  [127]. We assume

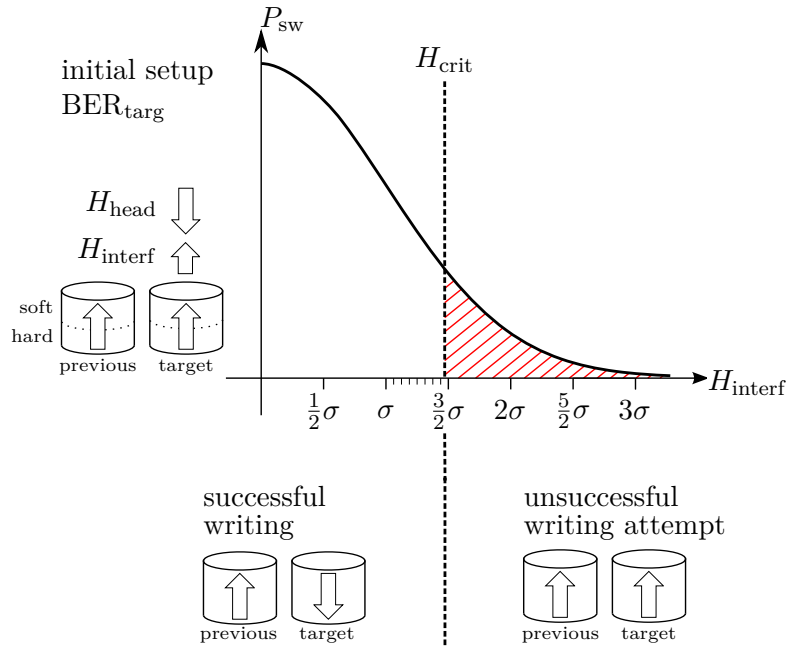


Figure 7.3: Calculation of Target Bit Error Rate with Assumed Switching Field Distribution  $P_{sw,est}$  with  $\sigma_{sw,est} = 0.015H_{ani}$ .  $H_{crit,targ}$  is the anti-parallel aligned external field  $H_{interf}$  which is needed to prevent switching of the target bit. Calculation of the previous bit error rate is analogue. We search for  $H_{crit,prev}$  which is the parallel applied field  $H_{interf}$  where the previous bit gets rewritten with  $H_{head}$ .

a field exposure time during writing  $t_{write} = 1$  ns. Then the number of passes before erasure is  $\tau/t_{write}$ , i.e.  $BER_{adj} = t_{write}/\tau$ .

The total bit error rate is the sum of the above described error rates  $BER_{tot} = BER_{targ} + BER_{prev} + BER_{adj}$ .

## 7.2 Geometrical Setup

A more dense media layout and composite media which switches by non-uniform rotation are introduced. New parameters for the recording head such as the pole tip taper-angle and shield thickness are optimized. The position of the recording head in cross- and down-track direction is now a free parameter as well.

### 7.2.1 Exchange Coupled Composite Media Design and Layout

Results from optimizing the recording head geometry of Section 6.4 show that the adjacent track erasure dominates the total error rate due to the high field magnitude in the neighboring tracks. The goal is to increase storage capacity and therefore we need to look at optimizations for higher areal densities. One promising way is to change

the switching type of the underlying media by adding additional exchange coupled layers. Bashir et al. demonstrated a head optimization using the software IOSO, while writing on bit patterned, exchange coupled graded media with an areal density of around 2.5 Tb/in<sup>2</sup> [23]. For their optimization they used the product of the write field gradient times the write field as objective function.

Exchange coupled composite media as shown in [132] allows a reduction of the required switching field while keeping a certain thermal stability (see Section 2.2). Introducing this media type promises more stable bits within a passing head's fringing field improving the previous and adjacent track error. In Fig. 7.4a the triangular media layout is shown with a down-track pitch of 13.5 nm, cross-track pitch of 11.7 nm and a dot diameter of 12 nm. The bits have a height of 12 nm and a distance to the head's air bearing surface of 6 nm. This results in an estimated areal density of 4.08 Tb/in<sup>2</sup> and a filling factor of 71.6%. In order to reproduce exchange coupled composites the finite element mesh of the media island is separated into three sections. A hard phase acting as the storage layer, a soft phase acting as the switching assist layer and a 1 nm thick coupling interface. A cross-sectional view can be seen in Fig. 7.4b.

New free parameters are the hard phase's magnetocrystalline anisotropy  $K_{1,\text{hard}}$  and the interface exchange constant  $A_{\text{ex,int}}$  of the coupling layer. The soft phase anisotropy is changed proportionally to the hard phase anisotropy  $K_{1,\text{soft}} = (1/5) K_{1,\text{hard}}$ . The magnetic saturation polarization of both phases is 0.7 T. In order to also consider position jitter, a corresponding distribution could be embedded into  $\sigma_{\text{sw}}$  in Equation (7.3) and (7.4) like described in (6.7) following [126]. Here also fabrication tolerances are included into the switching field distribution  $\sigma_{\text{sw}}$ .

## 7.2.2 Parametrized Recording Head Design

For each optimization of a specific writing scheme (centered, staggered and shingled), the free parameters are the trailing shield gap, trailing edge angle, side shield gap, side edge angle and trailing edge down-track position. Those are presented in Fig. 7.5. All angles are defined relative to their next main pole surface. The wrap around shield surfaces are constructed parallel to their opposing pole tip surface. Considering skewing (see Fig. 2.12), the taper angle from trailing edge to leading edge of the write head's air bearing surface (see Fig. 7.5c) is kept constant at 75° during optimization. Note that this trapezoidal or triangular air bearing surface shape is the reason for non-planar pole tip cross-track faces which might be restricted by manufacturability.

For centered and staggered writing an optimal cross-track offset of 0 nm is assumed due to symmetry of the scheme. For shingled recording this offset is included as free parameter. The shield thickness is included as parameter for the optimization process as well. The pole tip width and the shield thickness at 80 nm and 50 nm respectively are kept constant for this writing scheme.

In Fig. 7.5 the free design parameters of the write head and the contour of a wrap around shield are shown. In Fig. 7.5a the main pole and shield is pictured in down-track direction, with the side gap of the shield, the shield thickness, the side edge angles, the pole tip width and the cross-track offset parameter. Fig. 7.5b represents a cross



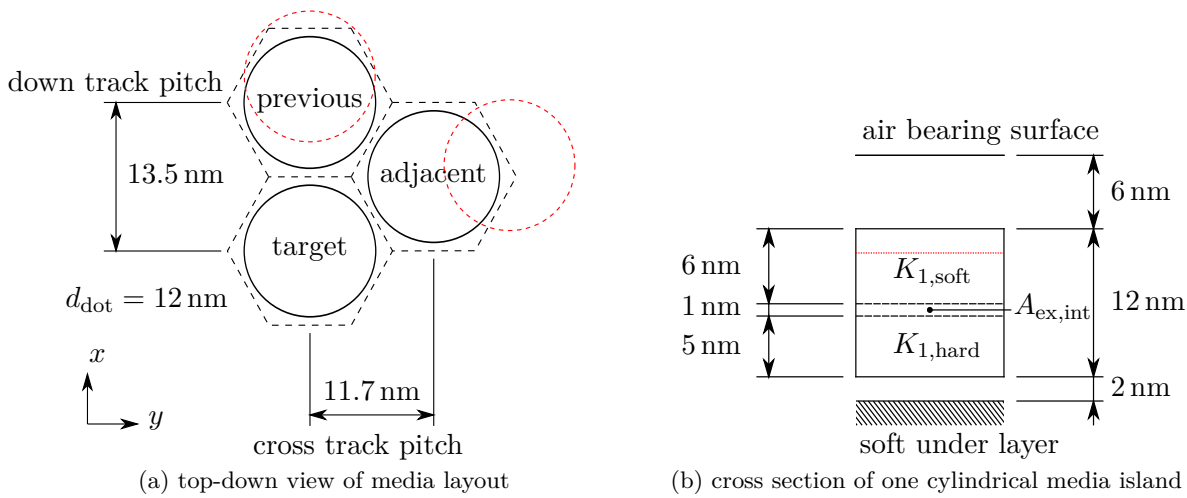


Figure 7.4: Media layout (a) top-down view and (b) cross section of 4 Tb/in<sup>2</sup> exchange coupled composite media with a dot diameter of  $d_{\text{dot}} = 12$  nm. The media is pseudo-hexagonally aligned with a 11.7 nm cross-track pitch and 13.5 nm down-track pitch.  $K_{1,\text{hard}}$  and  $A_{\text{ex,int}}$  are included as design parameters into the optimization procedure. Soft phase anisotropy is one fifth of hard phase anisotropy. Media filling factor = 71.6%. (Red dashed lines show the 2 Tb/in<sup>2</sup> media layout of Chapter 6.)

section of the geometry in cross-track direction illustrating the trailing shield gap, trailing edge angle and the down-track offset parameter. In Fig. 7.5c the write head and wrap around shield is shown from the media's perspective looking up to the air bearing surface, depicting the definition of the pole tip taper angle.

The wrap-around shield geometry has been improved for shingled magnetic recording heads, as an increased gap opposing the write corner cross-track direction has been introduced.

In order to reduce computational time, the recording head geometry has been simplified. In contrast to our work in Chapter 6, the finite element model comprises only the main pole and shield and not the full recording head structures. We cut the writer at yoke height and replace the influence of the yoke with magnetic surface charges at the cut plane. We set the surface charges  $\sigma_m$  to 2.4 T which has been acquired from previous full recording head simulations. This reduces the finite element mesh complexity of the write head while the cost in head field precision is tolerable. The method that mimicks the yoke with a simple charge sheet goes back to the work of Victora [133, 134]. In order to efficiently treat the soft underlayer we mirror pole tip and shield at the mirror plane. Fig. 7.6 shows how charge sheets and mirroring are used to model the yoke and the soft underlayer, respectively.

Table 7.1 summarizes the free parameters used during optimization and their parameter search range. All design parameters in this work are treated as continuous variables by the optimization algorithm.

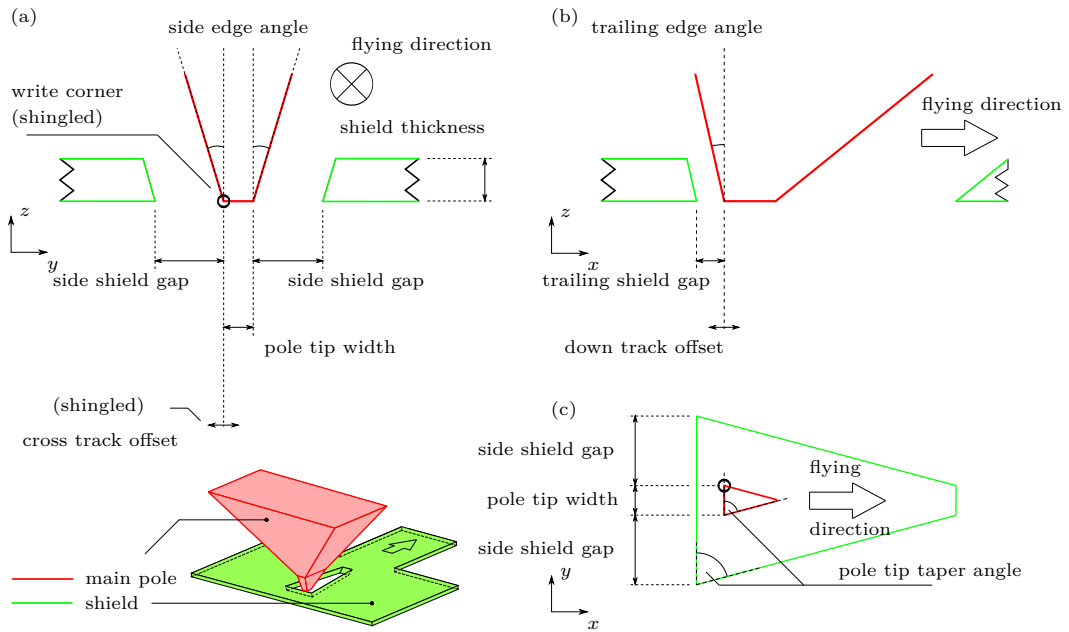


Figure 7.5: The main pole (red), wrap around shield (green) and their free parameters. The (a) down-track view of pole tip and shield with the writing scheme dependent cross-track offset, (b) cross-track view and (c) top view. The pole tip taper angle is always kept at  $75^\circ$ .

### 7.3 Results

The use of several design parameters during an optimization may result in an objective function landscape which has more than one local minimum with comparable objective function values. Thus more than one design with similar performance is possible. The two best designs for each writing scheme are summarized in Table 7.2. The field profiles of each writing scheme's best design are shown in Fig. 7.7. Each field profile is shown from the top, cross- and down-track direction. The top view shows a  $xy$ -plane slice of the field profile 9 nm below the air bearing surface, which corresponds to the middle of the media's soft phase. The cross- and down-track slices are taken depending on the location of the target bit which is furthermore dependent on optimized down- and cross-track offset. The location of target, previous and adjacent bit are illustrated as labeled contours.

For **centered writing** (Fig. 7.7a) the number of free parameters was 9. After 46 function evaluations the total bit error rate  $BER_{tot}$  was minimized to  $2.9 \times 10^{-3}$ . The target bit error rate  $BER_{targ}$  dominates for both optimized designs, which show considerable difference with respect to their geometry. One design has a very narrow pole tip of 5.3 nm while the other one has pole tip width of 18 nm. The narrow recording head is writing on a slightly softer media than the broad recording head. Making the media softer results

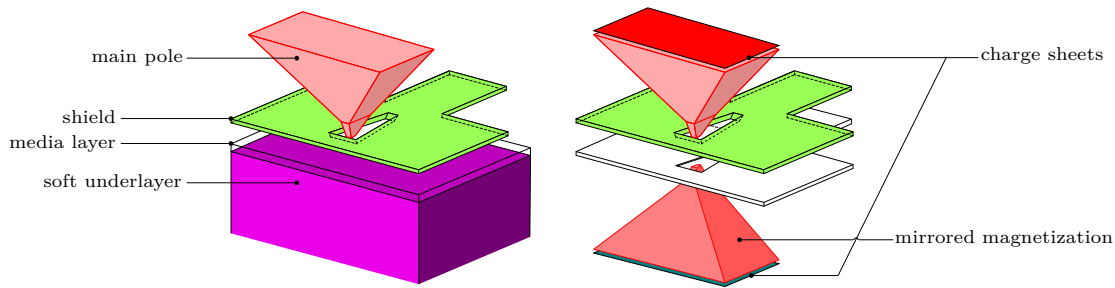


Figure 7.6: A focused view of the pole tip, shield, soft underlayer and location of the media layer. On the left hand side the soft underlayer is meshed with finite elements whereas on the right hand side the effect of the soft underlayer is mimicked by a mirrored pole tip, with charge sheets applying 2.4 T to the main pole.

in better writeability but also increases the chance of accidentally writing other bits. By increasing the uniaxial magnetocrystalline anisotropy of the media island we reduce the chance of unwanted switching of the previous and adjacent bit but also decrease the writeability of the target bit.

The narrow pole tip cannot apply much flux to the media, which can be seen by a higher target error rate. In contrast the wide tip reduces the target error but slightly increases adjacent track erasure. The wide tip needs a much sharper angle of  $18^\circ$  on the side walls to obtain similar adjacent error rates compared to the narrow tip with  $45^\circ$ .

For **staggered writing** (Fig. 7.7b) the number of free parameters was 9 as well. After 94 function evaluations the total bit error rate  $BER_{tot}$  was minimized to  $1.8 \times 10^{-2}$ . Due to the halved bit distance in down-track direction, in staggered recording overwriting of the previous bit becomes more likely as compared to the results in centered writing. However, adjacent track erasure is drastically decreased due to a narrow pole tip width of 12 nm. For the best two designs, optimized head and media parameters are very similar and do not vary much in error rates.

For **shingled writing** (Fig. 7.7c) the number of free parameters was 8. The total bit error rate was  $1.5 \times 10^{-8}$  after 62 function evaluations. The overall bit error rate is dominated by the probability of thermally switching an island on the adjacent track. A similar performance, with slightly changed trailing edge angle and side shield gap but with interfacial exchange coupling  $A_{ex}$  halved, was reached after 68 function evaluations with a total bit error rate of  $BER_{tot} = 8.4 \times 10^{-8}$ . For both designs the overall bit error rate is dominated by equal errors  $BER_{targ}$  and  $BER_{prev}$ , no matter if the media's hard and soft phase are strongly or weakly coupled. It is worth noting that the optimization found an exchange spring and an exchange break setting for the media design.

Additionally we calculated the zero field energy barriers  $E_{B,0}$  (shown in Table 7.2 as well) with the nudged elastic band method, for each best exchange coupled-composite media design. The zero field energy barrier of the two best centered writing designs are  $140k_B T$  and  $110k_B T$  respectively with  $T = 300$  K. For staggered writing both barriers are identical at  $110k_B T$  and for shingled writing we calculated zero field energy barriers

of  $140k_B T$  and  $130k_B T$ .

parameter	unit	lower bound	initial	upper bound
trailing shield gap	nm	5.0	9.0	20.0
trailing edge angle	°	5.0	20.0	45.0
side shield gap	nm	5.0	16.0	20.0
side edge angle	°	5.0	15.0	45.0
pole tip width	nm	5.0	14.0	20.0
pole tip taper angle	°	75.0	75.0	75.0
shield thickness	nm	3.0	10.0	20.0
$K_{1,\text{hard}}$	MJ/m <sup>3</sup>	0.5	0.8	1.2
$A_{\text{ex,int}}$	pJ/m	1.0	2.0	10.0
down-track offset	nm	0.0	6.8	8.0
cross-track offset	nm	-8.0	0.0	8.0

Table 7.1: Initial value, lower and upper bound for each free parameter. All parameters, of both the head and media, are treated simultaneously.

## 7.4 Remarks

An algorithm has been developed for the joint optimization of writer and media properties. Optimal design parameters for high-density bit patterned media recording were acquired. The areal density was doubled from 2 Tb/in<sup>2</sup> to 4 Tb/in<sup>2</sup> compared to the first approach (in Chapter 6). The evaluation of the error rate is fully based on micromagnetic simulations which take into account magnetization dynamics for computing on-track errors and also the thermally induced adjacent track erasure. The computational framework has been deployed on a computer cluster enabling a fast search for solutions of optimization problems with rich design spaces.

The optimization runs show that shingled writing clearly outperforms all the other investigated writing schemes for high areal densities with respect to write error rates. In centered or staggered writing the conflicting demands of a high field gradient and a high write field cause a poor on track performance of the writer. In the design parameters found for centered and staggered writing the perpendicular write field is well below 1 T. Decreasing the air bearing surface to media spacing of 6 nm as used in our simulations will be essential to achieve error rates below  $10^{-3}$  with centered writing on 4 Tb/in<sup>2</sup> exchange coupled composite bit patterned media. On the other hand write error rates in the range of  $10^{-8}$  were achieved for shingled writing.

One remark has to be made regarding the response space in relation to the early stopping criteria which is reached when designs couldn't even write the targeted bit. When such a stopping criteria is met the objective function was set to a total error rate above 1. This definitely led to a distorted response space making it more difficult to fit approximating functions to the total error rate.

BER <sub>tot</sub>	BER <sub>varg</sub>	BER <sub>prev</sub>	BER <sub>adj</sub>	BER <sub>radj</sub>	$E_{B,0}$ ( $k_B T$ )	$T = 300$ K	trailing shield			side edge			pole tip			down cross track		
							shield	gap	angle	shield	gap	angle	width	taper	angle	thickness	shield	offset
<b>centered writing</b>																		
$1.3 \times 10^{-2}$	$5.9 \times 10^{-3}$	$3.8 \times 10^{-3}$	$3.4 \times 10^{-3}$	$3.4 \times 10^{-3}$	140	15	31	12	45	5.3	75	12	660	2.6	5.4	0.0		
$2.9 \times 10^{-3}$	$2.8 \times 10^{-3}$	$3.2 \times 10^{-5}$	$3.6 \times 10^{-6}$	$3.6 \times 10^{-6}$	110	14	38	14	18	18	75	9.9	800	1.3	2.9	0.0		
<b>staggered writing</b>																		
$2.1 \times 10^{-2}$	$2.1 \times 10^{-3}$	$1.9 \times 10^{-2}$	$5.3 \times 10^{-17}$	$5.3 \times 10^{-17}$	110	13	24	11	31	12	75	12	620	1.1	3.6	0.0		
$1.8 \times 10^{-2}$	$8.9 \times 10^{-3}$	$8.9 \times 10^{-3}$	$2.8 \times 10^{-18}$	$2.8 \times 10^{-18}$	110	14	22	12	31	12	75	12	660	1.2	3.8	0.0		
<b>shingled writing</b>																		
$8.4 \times 10^{-8}$	$4.2 \times 10^{-8}$	$4.2 \times 10^{-8}$	$3.2 \times 10^{-15}$	$3.2 \times 10^{-15}$	130	10	19	11	31	80	75	50	730	5.3	7.2	5.6		
$1.5 \times 10^{-8}$	$9.9 \times 10^{-10}$	$9.9 \times 10^{-10}$	$1.3 \times 10^{-8}$	$1.3 \times 10^{-8}$	140	13	27	16	33	80	75	50	810	10	3.3	5.1		

Table 7.2: Bit error rates and parameters for two best designs of each of the three recording schemes: centered writing, staggered writing and shingled writing. All values are rounded to two significant digits.

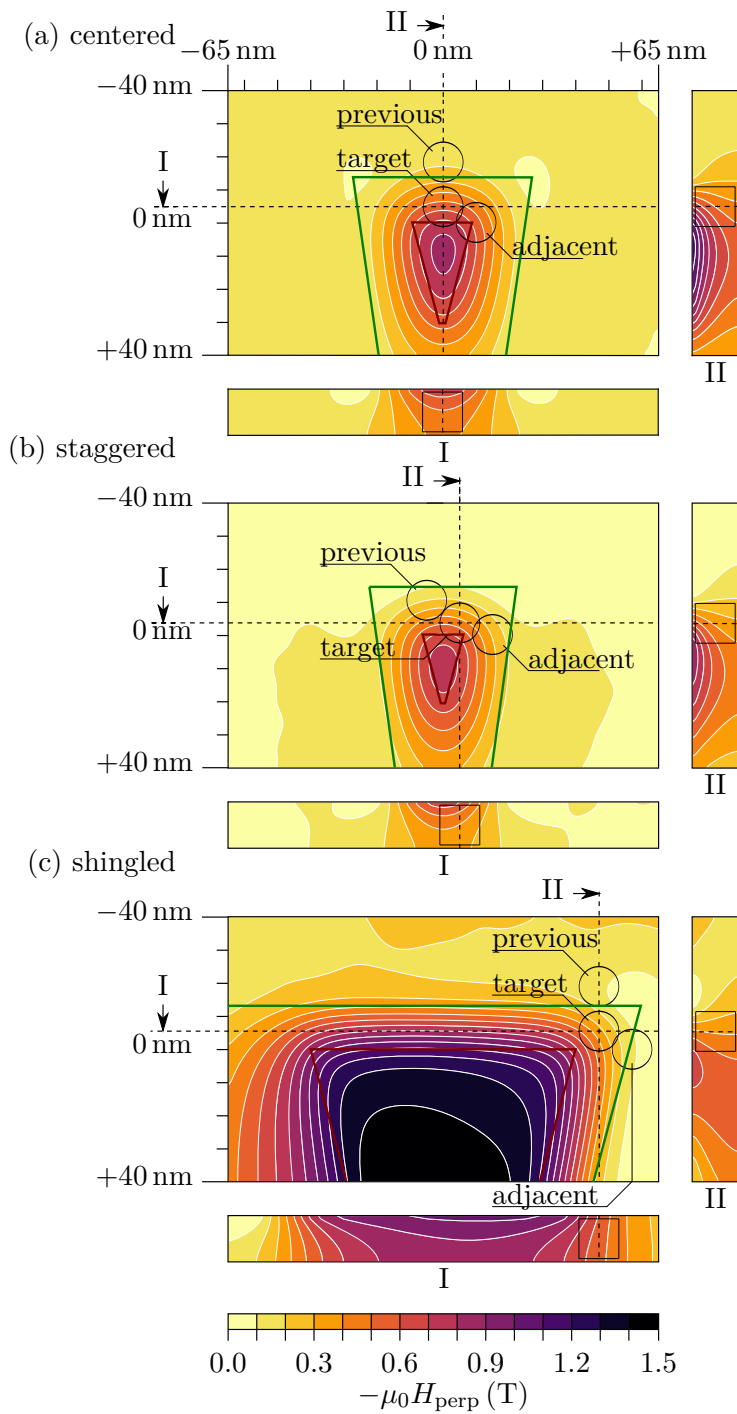


Figure 7.7: Perpendicular field profile of the optimized design for (a) centered writing (b) staggered writing and (c) shingled writing. Each field profile is shown in three perspectives: top view 9 nm below the air bearing surface, (I) cross-track view along down-track offset and (II) down-track view along cross-track offset. Each top view shows the contours of the best head's air bearing surface in red and shield in green.

# Conclusion and Outlook

## 8.1 Conclusion

Bit patterned media is a candidate for extending magnetic data storage towards 10 Tb/in<sup>2</sup>. Many papers have been published showing its potential [36, 70, 124, 126, 135]. Writing on conventional granular media, where a bit cell is formed by a large group of grains, no immediate loss of information appears if just a few grains are not switched by the write field. This is different with bit patterned media, where each bit is now represented by one cylindrically shaped grain (see Fig. 2.5). Now it has to be assessed whether switching has occurred or not and requires the introduction of error rates [27, 135].

This work's purpose is to demonstrate the capability of a fully automated recording head geometry optimization framework to find the best possible combination of recording head and bit patterned media design.

How well such a recording geometry performs in writing on a specific media type and layout, can be estimated by performing micromagnetic recording simulations of bit patterned media ensembles [126] and counting how many write errors occurred. This has to be repeated several times resulting in high computational cost. Another possibility is the use of a statistical approach to compute the write error rates [135]. Within this work, under the assumption of a Gaussian media switching field distribution, the statistical approach is applied with a maximum allowed disturbance field (see Section 7.1.4). This allowed to see the suitability of a specific recording head shape. Errors on adjacent or previously written bits could be observed while writing a targeted bit.

From first simple parameter and coil current variations (see Chapter 5) to an optimization framework including four to five varying parameters with multiple objectives (see Chapter 6) evolved a head-media co-optimization tool with a meaningful and informative single objective function improving nine different parameters (documented in Chapter 7).

The optimization improved the performance for writing on a single phase media with an areal density of 2 Td/in<sup>2</sup> (tera dots per square inch) and on exchange coupled composite media with an areal density of 4 Td/in<sup>2</sup>. The head-media system for centered

writing improved from a 50 % chance of a write error each write attempt to an acceptable error rate of  $3 \times 10^{-3}$ . The staggered recording head system's error rates reached a value of  $1 \times 10^{-2}$  to  $2 \times 10^{-2}$ . Results showed that the shingled writing scheme – due to its much wider tip width – is the most promising candidate. It achieves high effective fields of 1.8 T in the target track while 0.4 T low field is seen from bits at the adjacent track. This allows the use of highly thermally stable media material. Low error rates in the range of  $1 \times 10^{-5}$  for high density magnetic recording with a conventional perpendicular recording head are achieved. Much lower error rates of  $1 \times 10^{-8}$  are found if the geometrical features of the head are matched with the underlying media.

Since a large number of parameters are freely selectable by the optimizer, various parameter combinations can reach an error rate minimum. Due to the exchange constant between the hard and soft magnetic layer as a free parameter of the optimization two media switching types are found. One with an interface exchange of  $10 \text{ pJ m}^{-1}$  and one with half of the exchange constant. The high exchange coupling corresponds to an exchange spring behavior whereas the lower coupling value shows an exchange break behavior which has also been found in [136, 137].

### 8.1.1 Possible Model Improvements

Within this work several assumptions were made and certain effects have been neglected. Most importantly we neglected the effects of thermal fluctuations in the simulation of the writing process. In our simulation we used temperature dependent intrinsic material properties but neglect random thermal fluctuations. For fast writing these fluctuations may influence the switching time. Considering the full thermal effects would involve the introduction of a stochastic fluctuation term for each magnetic moment  $\mathbf{m}$  on the nodes of the finite element mesh [46, 138, 139].

In addition flying height, head position and the size of writer elements may fluctuate with temperature [140, 141]. Taking this effect into account would require the re-modeling and meshing of the recording system.

## 8.2 Outlook

While several geometrical parameters have been examined in this work, still more complex structures could be included into the optimization process. For example a filed patent showed cutouts in the trailing shield at different positions next to the pole tip which could be parametrized [142]. The stray field profile emitted by the recording head can be fine tuned by introducing such notches in the shield geometry [143]. This becomes more important for the promising shingled recording scheme.

By replacing the rather restrictive geometrical recording head description with a more flexible level-set method [144] better recording head and shield shapes could be found. Topology optimization has already been proven worth considering, if certain fabrication tolerances can be met [145]. In future we can foresee the combination of level-set methods for shape optimization combined with the dynamics of magnetic recording simulation for



computing the total error rate.

More parameters could be allowed to change for the underlying media, as for example the cross- and down-track pitches. This raises questions about media island to island interaction and its effects onto the assumed switching field distribution.

In a more production oriented perspective the design space could be configured to exactly match the possible manufacturing precisions, media layouts, etc. Economically speaking one could gain insight which production routine might be most beneficial in terms of error rate and areal density.

Besides conventional recording energy assisted magnetic recording features could be optimized. For example the heat spot or near field transducer shape in heat assisted magnetic recording (HAMR). Or the frequency, position and shape of spin-torque oscillators for microwave assisted magnetic recording (MAMR) could be analyzed. Conventional perpendicular recording will most likely be replaced by those new methods to reach areal densities of 10 Tb/in<sup>2</sup> [126].

The combination of micromagnetic simulations capable of resolving magnetization dynamics with an optimization framework does not only improve magnetic recording system. The joint optimization of various parameters like the shape of a magnetic recording head and properties of the media reduces the write error rate. Similarly micromagnetic simulations combined with numerical optimization can be used for optimizing magnetic materials and devices. An example are the optimization of permanent magnets with respect to their granular structure, in order to maximize the energy density product, which is the key figure of merit for permanent magnets [146].



Die approbierte gedruckte Originalversion dieser Dissertation ist an der TU Wien Bibliothek verfügbar.  
The approved original version of this doctoral thesis is available in print at TU Wien Bibliothek.

# Bibliography

- [1] O. Smith, *Some possible forms of phonograph*. Electrical World, 1888.
- [2] United States. Bureau of Labor, “Wages in the United States and Europe, 1870-1898,” Sep. 1898, (Accessed on 21/09/2020).
- [3] V. Poulsen, “Method of recording and reproducing sounds or signals.” Nov. 13 1900, US Patent 661,619.
- [4] V. Poulsen, P. O. Pedersen, and C. Schou, “Telegraphone.” May 9 1905, US Patent 789,336.
- [5] V. Poulsen, “Apparatus for effecting the storing up of speech or signals.” May 29 1906, US Patent 822,222.
- [6] V. Poulsen and P. O. Pedersen, “Telegraphone.” Dec. 10 1907, US Patent 873,083.
- [7] V. Poulsen, “Telegraphone.” Dec. 10 1907, US Patent 873,084.
- [8] P. O. Pedersen and V. Poulsen, “Electromagnet for telegraphone purposes.” Dec. 10 1907, US Patent 873,078.
- [9] F. Pfleumer, “Recording and reproducing device for magnetic sound writing,” Dec. 1941, US Patent 2247847.
- [10] M. N. Baibich, J. M. Broto, A. Fert, F. N. Van Dau, F. Petroff, P. Eitenne, G. Creuzet, A. Friederich, and J. Chazelas, “Giant magnetoresistance of (001)Fe/(001)Cr magnetic superlattices,” *Physical Review Letters*, vol. 61, no. 21, pp. 2472–2475, Nov. 1988.
- [11] G. Binasch, P. Grünberg, F. Saurenbach, and W. Zinn, “Enhanced magnetoresistance in layered magnetic structures with antiferromagnetic interlayer exchange,” *Physical Review B*, vol. 39, no. 7, pp. 4828–4830, mar 1989.
- [12] “IBM100 - The Application of Spintronics,” Mar. 2012, (Accessed on 09/05/2018).
- [13] S. Iwasaki, “Perpendicular magnetic recording - Its development and realization,” *Proceedings of the Japan Academy, Series B*, vol. 85, no. 2, pp. 37–54, Feb. 2009.

- [14] D. Suess, T. Schrefl, M. Kirschner, G. Hrkac, F. Dorfbauer, O. Ertl, and J. Fidler, "Optimization of exchange spring perpendicular recording media," *IEEE Transactions on Magnetics*, vol. 41, no. 10, pp. 3166–3168, 2005.
- [15] R. H. Victora and X. Shen, "Composite Media for Perpendicular Magnetic Recording," *IEEE Transactions on Magnetics*, vol. 41, no. 2, pp. 537–542, 2005.
- [16] "List of defunct hard disk manufacturers - Wikipedia," (Accessed on 02/02/2018). [Online]. Available: [https://en.wikipedia.org/wiki/List\\_of\\_defunct\\_hard\\_disk\\_manufacturers](https://en.wikipedia.org/wiki/List_of_defunct_hard_disk_manufacturers)
- [17] D. Rodic, "gnuclad: gnuclad tries to help the environment by creating trees. it's primary use will be generating cladogram trees for the gnu/linux distro timeline project." <https://launchpad.net/gnuclad>, 2010–2013.
- [18] D. Reinsel, J. Gantz, and J. Rydning, "IDC White Paper - The Digitization of the World - From Edge to Core," 2018.
- [19] Organisation for Economic Co-operation and Development, "Mobile data usage per mobile broadband subscription per month, 2019," 2020.
- [20] S. Boyd and L. Vandenberghe, *Convex Optimization*. Cambridge University Press, 2004.
- [21] L. Wang, P. K. Basu, and J. P. Leiva, "Automobile body reinforcement by finite element optimization," *Finite Elements in Analysis and Design*, vol. 40, no. 8, pp. 879–893, 2004.
- [22] F. Parasiliti, M. Villani, S. Lucidi, and F. Rinaldi, "Finite-Element-Based Multiobjective Design Optimization Procedure of Interior Permanent Magnet Synchronous Motors for Wide Constant-Power Region Operation," *IEEE Transactions on Industrial Electronics*, vol. 59, no. 6, pp. 2503–2514, Jun. 2012.
- [23] M. Bashir, T. Schrefl, J. Dean, A. Goncharov, G. Hrkac, D. Allwood, and D. Suess, "Head and bit patterned media optimization at areal densities of 2.5 Tbit/in<sup>2</sup> and beyond," *Journal of Magnetism and Magnetic Materials*, vol. 324, no. 3, pp. 269–275, 2012.
- [24] A. Kovacs, H. Oezelt, S. Bance, J. Fischbacher, M. Gusenbauer, F. Reichel, L. Exl, T. Schrefl, and M. Schabes, "Numerical optimization of writer geometries for bit patterned magnetic recording," *Journal of Applied Physics*, vol. 115, no. 17, p. 17B704, 2014.
- [25] A. Kovacs, H. Oezelt, M. E. Schabes, and T. Schrefl, "Numerical optimization of writer and media for bit patterned magnetic recording," *Journal of Applied Physics*, vol. 120, no. 1, p. 013902, 2016.

- [26] G. Varvaro and F. Casoli, *Ultra-high-density magnetic recording: storage materials and media designs*. CRC Press, 2016.
- [27] H. Muraoka, S. Greaves, and Y. Kanai, “Modeling and Simulation of the Writing Process on Bit-Patterned Perpendicular Media,” *IEEE Transactions on Magnetics*, vol. 44, no. 11, pp. 3423–3429, Nov. 2008.
- [28] K. Yamakawa, Y. Ohsawa, S. Greaves, and H. Muraoka, “Pole design optimization of shielded planar writer for 2 Tbit/in<sup>2</sup> recording,” *Journal of Applied Physics*, vol. 105, no. 7, p. 07B728, Apr. 2009.
- [29] R. Wood, M. Williams, A. Kavcic, and J. Miles, “The Feasibility of Magnetic Recording at 10 Terabits Per Square Inch on Conventional Media,” *IEEE Transactions on Magnetics*, vol. 45, no. 2, pp. 917–923, Feb. 2009.
- [30] D. Albrecht and T. Yoon, “Spindle motor winding for miniature hard disk drive,” Apr. 14 2009, US Patent 7,518,823.
- [31] T. Takahashi, A. Nanba, and M. Mochizuki, “Method of manufacturing a perpendicular magnetic recording head,” Dec. 24 2009, US Patent App. 12/487,306.
- [32] T. Albrecht, R. Fontana, P. Kasiraj, E. Klaassen, R. Payne, and T. Reiley, “Flying height adjustment for air bearing sliders,” Feb. 5 2002, US Patent 6,344,949.
- [33] H.-S. Jung, “Conventional Perpendicular Magnetic Recording Media,” in *Ultra-High-Density Magnetic Recording*. Pan Stanford, Mar. 2016, pp. 133–193.
- [34] A. Shukh, M. and N. Amin, “Magnetic head for perpendicular recording with suppressed side writing and erasing,” Jun. 30 2009, US Patent 7554765B2.
- [35] A. Goncharov, T. Schrefl, G. Hrkac, J. Dean, S. Bance, D. Suess, O. Ertl, F. Dorfbauer, and J. Fidler, “Recording simulations on graded media for area densities of up to 1 Tbit/in. 2,” *Applied Physics Letters*, vol. 91, no. 22, p. 222502, 2007.
- [36] H. J. Richter, a. Y. Dobin, R. T. Lynch, D. Weller, R. M. Brockie, O. Heinonen, K. Z. Gao, J. Xue, R. J. M. V. D. Veerdonk, P. Asselin, and M. F. Erden, “Recording potential of bit-patterned media,” *Applied Physics Letters*, vol. 88, no. 22, p. 222512, 2006.
- [37] D. Suess, T. Schrefl, and J. Fidler, “Reversal modes, thermal stability and exchange length in perpendicular recording media,” *IEEE transactions on magnetics*, vol. 37, no. 4, pp. 1664–1666, 2001.
- [38] H. N. Bertram and M. Williams, “SNR and density limit estimates: A comparison of longitudinal and perpendicular recording,” *IEEE transactions on magnetics*, vol. 36, no. 1, pp. 4–9, 2000.

- [39] F. Jeffers, “High-density magnetic recording heads,” *Proceedings of the IEEE*, vol. 74, no. 11, pp. 1540–1556, 1986.
- [40] R. Hunt, “A magnetoresistive readout transducer,” *IEEE Transactions on Magnetics*, vol. 7, no. 1, pp. 150–154, 1971.
- [41] M. Kief and R. Victora, “Materials for heat-assisted magnetic recording,” *MRS Bulletin*, vol. 43, no. 2, pp. 87–92, 2018.
- [42] H. Oezelt, A. Kovacs, J. Fischbacher, P. Matthes, E. Kirk, P. Wohlhüter, L. J. Heyderman, M. Albrecht, and T. Schrefl, “Switching field distribution of exchange coupled ferri-/ferromagnetic composite bit patterned media,” *Journal of Applied Physics*, vol. 120, no. 9, p. 093904, 2016.
- [43] S. Batra, J. Hannay, H. Zhou, and J. Goldberg, “Investigations of Perpendicular Write Head Design for 1 tera bit per square inch,” *IEEE Transactions on Magnetics*, vol. 40, no. 1, pp. 319–325, Jan. 2004.
- [44] V. K. M. V. A. Inomata and V. S.-y. Hasegawa, “Thermally assisted magnetic recording,” *Fujitsu Sci. Tech. J.*, vol. 42, no. 1, pp. 158–167, 2006.
- [45] D. Weller, G. Parker, O. Mosendz, A. Lyberatos, D. Mitin, N. Y. Safonova, and M. Albrecht, “Review Article: FePt heat assisted magnetic recording media,” *Journal of Vacuum Science & Technology B, Nanotechnology and Microelectronics: Materials, Processing, Measurement, and Phenomena*, vol. 34, no. 6, p. 060801, 2016.
- [46] C. Vogler, “Thermal effects in micromagnetism - from ultrafast magnetization reversal to long term stability,” Ph.D. thesis, Vienna University of Technology, 2015.
- [47] C. Vogler, C. Abert, F. Bruckner, D. Suess, and D. Praetorius, “Heat-assisted magnetic recording of bit-patterned media beyond 10 Tb/in<sup>2</sup>,” *Applied Physics Letters*, vol. 108, no. 10, pp. 1–6, 2016.
- [48] R. F. L. Evans, R. W. Chantrell, U. Nowak, A. Lyberatos, and H.-J. Richter, “Thermally induced error: density limit for magnetic data storage,” *Applied Physics Letters*, vol. 100, no. 10, p. 102402, Nov. 2011.
- [49] M. A. Bashir, T. Schrefl, J. Dean, A. Goncharov, G. Hrkac, S. Bance, D. Allwood, and D. Suess, “Microwave-assisted magnetization reversal in exchange spring media,” *IEEE Transactions on Magnetics*, vol. 44, no. 11 PART 2, pp. 3519–3522, Nov. 2008.
- [50] S. Li, B. Livshitz, H. N. Bertram, E. E. Fullerton, and V. Lomakin, “Microwave-assisted magnetization reversal and multilevel recording in composite media,” *Journal of Applied Physics*, vol. 105, no. 7, p. 07B909, Apr. 2009.

- [51] S. Li, B. Livshitz, H. N. Bertram, M. Schabes, T. Schrefl, E. E. Fullerton, and V. Lomakin, “Microwave assisted magnetization reversal in composite media,” *Applied Physics Letters*, vol. 94, no. 20, p. 202509, May 2009.
- [52] *11th Joint MMM-Intermag Conference, BB-12, "Microwave-assisted magnetic recording using multi-level exchange-coupled composite bit patterned media design"*, A.Kovacs, S.Li, B.Livshitz, T.Schrefl and V.Lomakin, 2010.
- [53] J. Lohau, A. Moser, C. Rettner, M. Best, and B. Terris, “Writing and reading perpendicular magnetic recording media patterned by a focused ion beam,” *Applied Physics Letters*, vol. 78, no. 7, pp. 990–992, 2001.
- [54] D. Weller, H. Brändle, G. Gorman, C.-J. Lin, and H. Notarys, “Magnetic and magneto-optical properties of cobalt-platinum alloys with perpendicular magnetic anisotropy,” *Applied Physics Letters*, vol. 61, no. 22, pp. 2726–2728, Nov. 1992.
- [55] S. John Greaves, H. Muraoka, and Y. Kanai, “The feasibility of bit-patterned recording at 4 Tb/in.<sup>2</sup> without heat-assist,” *Journal of Applied Physics*, vol. 109, no. 7, p. 07B702, 2011.
- [56] H. N. Bertram, *Theory of Magnetic Recording*. Cambridge University Press, 1994.
- [57] T. R. Albrecht, H. Arora, V. Ayanoor-Vitikkate, J. M. Beaujour, D. Bedau, D. Berman, A. L. Bogdanov, Y. A. Chapuis, J. Cushen, E. E. Dobisz, G. Doerk, H. Gao, M. Grobis, B. Gurney, W. Hanson, O. Hellwig, T. Hirano, P. O. Jubert, D. Kercher, J. Lille, Z. Liu, C. M. Mate, Y. Obukhov, K. C. Patel, K. Rubin, R. Ruiz, M. Schabes, L. Wan, D. Weller, T. W. Wu, and E. Yang, “Bit-patterned magnetic recording: Theory, media fabrication, and recording performance,” *IEEE Transactions on Magnetics*, vol. 51, no. 5, pp. 1–44, 2015.
- [58] H. Oezelt, A. Kovacs, P. WohllhÄijter, E. Kirk, D. Nissen, P. Matthes, L. J. Heyderman, M. Albrecht, and T. Schrefl, “Micromagnetic simulation of exchange coupled ferri-/ferromagnetic composite in bit patterned media,” *Journal of Applied Physics*, vol. 117, no. 17, p. 17E501, 2015.
- [59] W. F. Brown, “Micromagnetics, Domains, and Resonance,” *Journal of Applied Physics*, vol. 30, no. 4, pp. 62–69, 1959.
- [60] H. Kronmüller and M. Fähnle, *Micromagnetism and the Microstructure of Ferromagnetic Solids*. Cambridge University Press, 2003.
- [61] R. Skomski, *Simple Models of Magnetism*. Oxford University Press, 2008.
- [62] D. Hahn, M. A. Bashir, T. Schrefl, A. Cazau, M. a. Gubbins, and D. Suess, “Graded media design for area density of up to 2.5 Tb/in<sup>2</sup>,” *IEEE Transactions on Magnetics*, vol. 46, no. 6, pp. 1866–1868, 2010.

- [63] J. M. D. Coey, *Magnetism and Magnetic Materials*. Cambridge University Press, 2014.
- [64] D. Suess, T. Schrefl, S. FÄdhler, M. Kirschner, G. Hrkac, F. Dorfbauer, and J. Fidler, “Exchange spring media for perpendicular recording,” *Applied Physics Letters*, vol. 87, no. 1, p. 012504, 2005.
- [65] D. Suess, “Multilayer Exchange Spring Recording Media,” Dec. 20 2007, US Patent App. 11/424,859.
- [66] D. Suess, M. Fuger, C. Abert, F. Bruckner, and C. Vogler, “Superior bit error rate and jitter due to improved switching field distribution in exchange spring magnetic recording media,” *Scientific Reports*, vol. 6, no. 1, p. 27048, Jul. 2016.
- [67] H. Kronmüller and D. Goll, “Micromagnetic theory of the pinning of domain walls at phase boundaries,” *Physica B: Condensed Matter*, vol. 319, no. 1-4, pp. 122–126, 2002.
- [68] J. Kalezhi and J. J. Miles, “An energy barrier model for write errors in exchange-spring patterned media,” *IEEE Transactions on Magnetics*, vol. 47, no. 10, pp. 2540–2543, Oct. 2011.
- [69] G. Varvaro, S. Laureti, and D. Fiorani, “{L10} FePt-based thin films for future perpendicular magnetic recording media,” *Journal of Magnetism and Magnetic Materials*, vol. 368, pp. 415–420, 2014.
- [70] R. Wood, “The feasibility of magnetic recording at 1 Terabit per square inch,” *IEEE Transactions on Magnetics*, vol. 36, no. 1, pp. 36–42, 2000.
- [71] S. Iwasaki and K. Takemura, “An analysis for the circular mode of magnetization in short wavelength recording,” *IEEE Transactions on Magnetics*, vol. 11, no. 5, pp. 1173–1175, 1975.
- [72] M. T. Moneck, T. Okada, J. Fujimori, T. Kasuya, M. Katsumura, T. Iida, K. Kuriyama, W. Lin, V. Sokalski, S. Powell, J. A. Bain, and J. Zhu, “Fabrication and recording of bit patterned media prepared by rotary stage electron beam lithography,” *IEEE Transactions on Magnetics*, vol. 47, no. 10, pp. 2656–2659, oct 2011.
- [73] S. S. Parkin, “Digital magnetoresistive sensor based on the giant magnetoresistance effect,” Dec. 17 1996, US Patent 5,585,986.
- [74] Z. Gao, S. Mao, K. Tran, J. Nowak, and J. Chen, “Tunneling barrier material for a magnetic recording head,” Sep. 14 2004, US Patent 6,791,806.
- [75] Q. Le, D. J. Seagle, X. Liu, D. Mauri, Y. Ahn, H. Jiang, G. Liu, D. P. Druist, and J.-l. Li, “Magnetic sensor using spin hall effect,” Dec. 13 2018, US Patent App. 15/826,578.



- [76] H. J. Richter, A. Y. Dobin, and D. K. Weller, “Data Storage Device with Bit Patterned Media with Staggered Islands,” 2007, US Patent 20070258161A1.
- [77] A. Fert, P. Grünberg, A. Barthélémy, F. Petroff, and W. Zinn, “Layered magnetic structures: interlayer exchange coupling and giant magnetoresistance,” *Journal of Magnetism and Magnetic Materials*, vol. 140, pp. 1–8, 1995.
- [78] B. Livshitz, A. Inomata, H. N. Bertram, and V. Lomakin, “Analysis of recording in bit patterned media with parameter distributions,” *Journal of Applied Physics*, vol. 105, no. 7, p. 07C111, Apr. 2009.
- [79] M. Mallary and M. Benakli, “Perpendicular magnetic recording write head design,” *International Journal of Product Development*, vol. 5, no. 3/4, p. 226, 2008.
- [80] T. Okada, I. Nunokawa, M. Mochizuki, M. Hatatani, H. Kimura, K. Etoh, M. Fuyama, and K. Nakamoto, “Newly developed wraparound-shielded head for perpendicular recording,” *IEEE Transactions on Magnetics*, vol. 41, no. 10, pp. 2899–2901, Oct. 2005.
- [81] M. L. Plumer, J. van Ek, and D. Weller, Eds., *The Physics of Ultra-High-Density Magnetic Recording*. Springer Berlin Heidelberg, 2001.
- [82] J. Davis and J. Wilde, “Flying magneto-optical head with a steerable mirror,” May 2 2000, US Patent 6,058,094.
- [83] T. R. Albrecht, O. Hellwing, R. Ruiz, M. E. Schabes, B. D. Terris, and X. Z. Wu, “Bit-patterned magnetic recording: Nanoscale magnetic islands for data storage,” in *Nanoscale Magnetic Materials and Applications*. Springer US, 2009, pp. 237–274.
- [84] E. Grimson, J. Guttag, and A. Bell, “Introduction to Computational Thinking and Data Science,” Jun. 2018, (Accessed 09/21/2018).
- [85] D. Jones, M. Schonlau, and W. Welch, “Efficient global optimization of expensive black-box functions,” *Journal of Global optimization*, vol. 13, no. 4, pp. 455–492, 1998.
- [86] D. Huang, T. T. Allen, W. I. Notz, and N. Zeng, “Global Optimization of Stochastic Black-Box Systems via Sequential Kriging Meta-Models,” *Journal of Global Optimization*, vol. 34, no. 3, pp. 441–466, Mar. 2006.
- [87] J. S. Park, “Optimal Latin-hypercube designs for computer experiments,” *Journal of Statistical Planning and Inference*, vol. 39, no. 1, pp. 95–111, 1994.
- [88] G. Damblin, M. Couplet, and B. Iooss, “Numerical studies of space-filling designs: Optimization of Latin Hypercube Samples and subprojection properties,” *Journal of Simulation*, vol. 7, no. 4, pp. 276–289, Jul. 2013.

- [89] J. L. Loeppky, J. Sacks, and W. J. Welch, “Choosing the sample size of a computer experiment: A practical guide,” *Technometrics*, vol. 51, no. 4, pp. 366–376, 2009.
- [90] A. Marrel, “Mise en oeuvre et utilisation du métamodèle processus gaussien pour l’analyse de sensibilité de modèles numériques: application à un code de transport hydrogéologique,” Ph.D. thesis, Toulouse, INSA, 2008.
- [91] B. M. Adams, M. S. Ebeida, M. S. Eldred, J. D. Jakeman, L. P. Swiler, J. A. Stephens, D. M. Vigil, T. M. Wildey, W. J. Bohnhoff, K. R. Dalbey, J. P. Eddy, K. T. Hu, L. E. Bauman, and P. D. Hough, “Dakota, A Multilevel Parallel Object-Oriented Framework for Design Optimization, Parameter Estimation, Uncertainty Quantification, and Sensitivity Analysis: Version 6.2 User’s Manual,” *Sandia Technical Report SAND2014-4633*, Jul. 2014.
- [92] “Heeds | red cedar technology,” [http://www.redcedartech.com/products/heeds\\_mdo](http://www.redcedartech.com/products/heeds_mdo), (Accessed on 05/18/2017).
- [93] J. C. Slater, “Energy-Band Theory of Magnetism,” *Journal of Applied Physics*, vol. 39, no. 2, pp. 761–767, 1968.
- [94] E. Bauer, C. Eisenmenger-Sittner, and J. Fidler, *Materialwissenschaften. Unveröffentlichtes Skriptum, Institut für Festkörperphysik, Technische Universität Wien*, 2013.
- [95] R. Birss and P. Wallis, “A new torque meter or torque magnetometer,” *Journal of Scientific Instruments*, vol. 40, no. 12, p. 551, 1963.
- [96] A. Aharoni, *Introduction to the Theory of Ferromagnetism*. Clarendon Press, 2000, vol. 109.
- [97] W. Scholz, “Scalable parallel micromagnetic solvers for magnetic nanostructures,” Ph.D. thesis, Vienna University of Technology, 2003.
- [98] D. Fredkin and T. Köhler, “Hybrid method for computing demagnetizing fields,” *IEEE Transactions on Magnetics*, vol. 26, no. 2, pp. 415–417, Mar. 1990.
- [99] P. Asselin and A. Thiele, “On the field Lagrangians in micromagnetics,” *IEEE transactions on magnetics*, vol. 22, no. 6, pp. 1876–1880, 1986.
- [100] W. F. Brown, *Micromagnetics*. interscience publishers, 1963, no. 18.
- [101] T. L. Gilbert, “A lagrangian formulation of the gyromagnetic equation of the magnetization field,” *Phys. Rev.*, vol. 100, p. 1243, 1955.
- [102] T. Gilbert, “Classics in Magnetism A Phenomenological Theory of Damping in Ferromagnetic Materials,” *IEEE Transactions on Magnetics*, vol. 40, no. 6, pp. 3443–3449, Nov. 2004.

- [103] P. Wohllhüter, “Landau-Lifshitz- und Landau-Lifshitz-Gilbert-Gleichung mit Langevin-Dynamik sowie Spin Transfer Torque,” Jul. 2010, Talk, University of Konstanz.
- [104] C. Schieback, “Computersimulationen zur Struktur und Dynamik von Domänenwänden,” Ph.D. thesis, University of Konstanz, 2010.
- [105] W. Brown, “Thermal fluctuation of fine ferromagnetic particles,” *IEEE Transactions on Magnetics*, vol. 15, no. 5, pp. 1196–1208, 1979.
- [106] G. Henkelman, B. P. Uberuaga, and H. Jónsson, “A climbing image nudged elastic band method for finding saddle points and minimum energy paths,” *The Journal of Chemical Physics*, vol. 113, no. 22, pp. 9901–9904, Dec. 2000.
- [107] R. Dittrich, T. Schrefl, D. Suess, W. Scholz, H. Forster, and J. Fidler, “A path method for finding energy barriers and minimum energy paths in complex micro-magnetic systems,” *Journal of Magnetism and Magnetic Materials*, vol. 250, pp. 12–19, Sep. 2002.
- [108] W. E. Ren, and E. Vanden-Eijnden, “String method for the study of rare events,” *Phys. Rev. B*, vol. 66, p. 052301, Aug. 2002.
- [109] —, “Simplified and improved string method for computing the minimum energy paths in barrier-crossing events,” *Journal of Chemical Physics*, vol. 126, p. 164103, May 2007.
- [110] A. Samanta and E. Weinan, “Optimization-based string method for finding minimum energy path,” *Communications in Computational Physics*, vol. 14, no. 2, pp. 265–275, 2013.
- [111] E. Paz, F. Garcia-Sanchez, and O. Chubykalo-Fesenko, “Numerical evaluation of energy barriers in nano-sized magnetic elements with Lagrange multiplier technique,” *Physica B: Condensed Matter*, vol. 403, no. 2, pp. 330–333, 2008.
- [112] “SALOME the open source integration platform for numerical simulation,” <https://www.salome-platform.org>, (Accessed on 02/07/2016).
- [113] “NETGEN automatic mesh generator,” <https://sourceforge.net/projects/netgen-mesher/>, (Accessed on 02/07/2016).
- [114] W. Scholz and S. Batra, “Effect of write current waveform on magnetization and head-field dynamics of perpendicular recording heads,” *IEEE transactions on magnetics*, vol. 42, no. 10, pp. 2264–2266, 2006.
- [115] T. Schrefl, M. E. Schabes, D. Suess, O. Ertl, M. Kirschner, F. Dorfbauer, G. Hrkac, and J. Fidler, “Partitioning of the Perpendicular Write Field Into Head and SUL Contributions,” *IEEE Transactions on Magnetics*, vol. 41, no. 10, pp. 3064–3066, 2005.

- [116] J. Ahrens, B. Geveci, C. Law, C. Hansen, and C. Johnson, *ParaView: An End-User Tool for Large-Data Visualization*. Citeseer, 2005.
- [117] M. Mallary, A. Torabi, and M. Benakli, “One terabit per square inch perpendicular recording conceptual design,” *IEEE Transactions on Magnetics*, vol. 38, no. 4 I, pp. 1719–1724, Jul. 2002.
- [118] I. Tudosa, C. Stamm, A. Kashuba, F. King, H. Siegmann, J. Stöhr, G. Ju, B. Lu, and D. Weller, “The ultimate speed of magnetic switching in granular recording media,” *Nature*, vol. 428, no. 6985, pp. 831–833, 2004.
- [119] R. Victora, “Predicted time dependence of the switching field for magnetic materials,” *Physical review letters*, vol. 63, no. 4, p. 457, 1989.
- [120] H. J. Richter, N. Supper, B. Wilson, and B. D. Terris, “Magnetic Recording Near the Grain Size Limit,” *IEEE Transactions on Magnetics*, vol. 48, no. 11, pp. 3887–3890, Nov. 2012.
- [121] “SHERPA - An Efficient and Robust Optimization / Search Algorithm.” [Online]. Available: [www.redcedartech.com/pdfs/SHERPA.pdf](http://www.redcedartech.com/pdfs/SHERPA.pdf)
- [122] W. Xia, T. Yamada, H. Aoi, H. Muraoka, and Y. Nakamura, “Reduction of track width in perpendicular magnetic recording,” *Journal of Magnetism and Magnetic Materials*, vol. 287, pp. 77–82, Feb. 2005.
- [123] H. A. Shute, J. J. Miles, D. T. Wilton, and D. J. Mapps, “Optimization of heads for perpendicular recording,” *IEEE Transactions on Magnetics*, vol. 38, no. 5 I, pp. 2207–2209, Sep. 2002.
- [124] Y. Dong, Y. Wang, and R. H. Victora, “Micromagnetic specifications for recording self-assembled bit-patterned media,” *Journal of Applied Physics*, vol. 111, no. 7, p. 07B904, 2012.
- [125] J. Kalezhi, B. D. Belle, and J. J. Miles, “Dependence of write-window on write error rates in bit patterned media,” *IEEE Transactions on Magnetics*, vol. 46, no. 10, pp. 3752–3759, Oct. 2010.
- [126] M. E. Schabes, “Micromagnetic simulations for terabit/in<sup>2</sup> head/media systems,” *Journal of Magnetism and Magnetic Materials*, vol. 320, no. 22, pp. 2880 – 2884, 2008.
- [127] J. Dean, M. A. Bashir, A. Goncharov, G. Hrkac, S. Bance, T. Schrefl, A. Cazacu, M. Gubbins, R. W. Lamberton, and D. Suess, “Thermally induced adjacent track erasure in exchange spring media,” *Applied Physics Letters*, vol. 92, no. 14, p. 142505, 2008.

- [128] Y. Kanai, S. J. Greaves, K. Yamakawa, H. Aoi, H. Muraoka, and Y. Nakamura, “A single-pole-type head design for 400 Gb/in<sup>2</sup> recording,” *IEEE Transactions on Magnetism*, vol. 41, no. 2, pp. 687–695, Feb. 2005.
- [129] H. Fukuda and Y. Nakatani, “Recording Density Limitation Explored by Head/Media Co-Optimization Using Genetic Algorithm and GPU-Accelerated LLG,” *IEEE Transactions on Magnetism*, vol. 48, no. 11, pp. 3895–3898, Nov. 2012.
- [130] X. G. Li, Z. J. Liu, A. G. Kang, and X. Y. Xie, “Writing Field Analysis for Shingled Bit-Patterned Magnetic Recording,” *Journal of Nanomaterials*, vol. 2017, pp. 1–9, 2017.
- [131] Y. Dong and R. H. Victora, “Micromagnetic Specification for Bit Patterned Recording at 4 Tbit/in<sup>2</sup>,” *IEEE Transactions on Magnetism*, vol. 47, no. 10, pp. 2652–2655, Oct. 2011.
- [132] A. Y. Dobin and H. J. Richter, “Domain wall assisted magnetic recording (invited),” *Journal of Applied Physics*, vol. 101, no. 9, p. 09K108, May 2007.
- [133] X. Shen and R. H. Victora, “Write head design for exchange coupled composite media,” *IEEE transactions on magnetism*, vol. 43, no. 6, pp. 2172–2174, 2007.
- [134] —, “Effect of pole tip geometry on remnant field,” *Journal of Applied Physics*, vol. 103, no. 7, p. 07F542, 2008.
- [135] H. Muraoka and S. J. Greaves, “Statistical Modeling of Write Error Rates in Bit Patterned Media for 10 Tb / in 2 Recording,” *IEEE Transactions on Magnetism*, vol. 47, no. 1, pp. 26–34, 2011.
- [136] K. Y. Guslienko, O. Chubykalo-Fesenko, O. Mryasov, R. Chantrell, and D. Weller, “Magnetization reversal via perpendicular exchange spring in FePt / FeRh bilayer films,” *Physical Review B*, vol. 70, no. 10, p. 104405, Sep. 2004.
- [137] D. Suess, T. Schrefl, S. Fähler, M. Kirschner, G. Hrkac, F. Dorfbauer, and J. Fidler, “Exchange spring media for perpendicular recording,” *Applied Physics Letters*, vol. 87, no. 1, p. 012504, Jul. 2005.
- [138] L. Baas, A. Prohl, and M. Slodička, “Numerical scheme for augmented Landau-Lifshitz equation in heat assisted recording,” *Journal of Computational and Applied Mathematics*, vol. 236, no. 18, pp. 4775–4787, 2012.
- [139] D. Arjmand, M. Poluektov, and G. Kreiss, “Atomistic-continuum multiscale modelling of magnetisation dynamics at non-zero temperature,” *Advances in Computational Mathematics*, no. 4, pp. 1119–1151, Dec. 2018.
- [140] K. F. Young and D. J. Seagle, “System and method for minimizing thermal pole tip protrusion,” Apr. 25 2006, US Patent 7,035,046.

- [141] K. S. Stoev, S. Song, and T. Pan, “Magnetic recording head with resistive heating element located near the write coil,” Jun. 1 2010, US Patent 7,729,087.
- [142] S. Basu, M. Gubbins, M. A. Bashir, and P. Gangmei, “Data writer with flux density insert,” 2015, US Patent 9196267B2.
- [143] M. Benakli and S. Batra, “Magnetic recording head with notched shield,” Oct. 16 2012, US Patent 8,289,647.
- [144] V. Melicher, I. Cimrak, and R. Van Keer, “Level set method for optimal shape design of MRAM core. Micromagnetic approach,” *Physica B: Condensed Matter*, vol. 403, no. 2-3, pp. 308–311, 2008.
- [145] S. Park, J. Yoo, and J. S. Choi, “Optimal Shape Design of the Perpendicular Magnetic Recording Head,” *IEEE Transactions on Magnetics*, vol. 45, no. 5, pp. 2272–2275, May 2009.
- [146] A. Kovacs, J. Fischbacher, M. Gusenbauer, H. Oezelt, H. C. Herper, O. Y. Vekilova, P. Nieves, S. Arapan, and T. Schrefl, “Computational design of rare-earth reduced permanent magnets,” *Engineering*, vol. 6, no. 2, pp. 148–153, 2020.